This thesis is approved by:

Professor Greg Nellis 

Professor Mark Anderson 

HIGH-TEMPERATURE THERMAL PROPERTIES OF PARTICLES FOR CONCENTRATED SOLAR POWER AND THERMAL ENERGY STORAGE SYSTEMS

by

Jeff Maskalunas

A thesis submitted in partial fulfillment of

the requirements for the degree of

Master of Science

(Mechanical Engineering)

at the

UNIVERSITY OF WISCONSIN-MADISON

2020

Dedication

To begin, I started this intensive project not really knowing much about research (let alone particle flow) and was only armed with a chip on my shoulder to grind. Through the struggle, I have grown quite a bit over the past two and a half years, and there were a lot of people involved in this project that helped me along the way. First and foremost, thank you to Professor Greg Nellis and Professor Mark Anderson for procuring the funds for this project, providing advice, and nudging me in the right direction. I truly appreciate you sticking with me when I was stumbling through difficulties and slow progress in the beginning of my research. Thank you to my undergraduate research assistants Max Henry, Alastair "AL" Luna, and Brady Reichardt; THL Senior Lab Technician Paul Brooks; THL Instrument Maker Seth Jones; Jay, Jeff, and Mike from the TEAM Lab at UW-Madison; Thomas Harrington and Tyler from PSL; and the other students in the SEL/THL who provided hands on help with my experiments. Thank you to Professor Mike Wagner at UW-Madison, Megan Kirschmeier at Brayton Energy, Professor Greg Mehos, Evan Johnson at METU, Dustin Witkowski at UW-Madison, Professor Sanford Klein, and a handful of others at NREL and Brayton Energy who gave advice and critiqued my work. A special shout out to the Hodags, the men's ultimate team at UW-Madison, which I spent my last year of eligibility on the team captaining during my first year of research – Hodag Love. Lastly, thank you to the family and friends, especially Holly, who cared for me and checked in on my mental and emotional health along the way. It means more to me than I show.

Acknowledgements

This work was funded by the Department of Energy's Office of Energy Efficiency and Renewable Energy under award DE-EE0008368 through a subcontract from Brayton Energy.

This research was partially supported by the University of Wisconsin-Madison College of Engineering Shared Research Facilities and the NSF through the Materials Science Research Center (DMR-1720415) using instrumentation provided at the UW-Madison Materials Science Center

Non-Technical Project Description

Concentrated Solar Power (CSP) is a technology that uses heat from the sun to produce electricity. A CSP facility does this first by redirecting the sun's rays with mirrors towards a single point called a receiver. A traditional receiver has a black surface and gets very hot as a result – higher than temperatures that would melt aluminum. Simultaneously, a liquified, molten salt is pumped through piping in contact with the hot receiver to pass heat to the molten salt. The heated molten salt then flows towards either a power cycle or a storage vessel. The power cycle uses the heat from the molten salt to drive a turbine which produces usable electricity. The storage vessel has high-temperature insulation which helps the molten salt retain most of its heat for a period of time, usually less than 24 hours, until the hot molten salt is required for the power cycle to produce electricity; the temperature decrease of the molten salts in these storage vessels due to heat loss is fairly negligible. The benefit of having this storage vessel is that these CSP facilities can continue to operate whether or not the sun is out. If the sun is out, there is enough molten salt heated by the receiver to use some salt to create electricity via the power cycle and store the rest of the hot molten salt in the storage vessel. When the sun is not out, the receiver is not getting heated, so the hot molten salt in the storage vessel can be used to provide heat to the power cycle. This ability to store thermal energy makes CSP technology with Thermal Energy Storage (TES) particularly appealing because the facilities can operate 24/7. Current research is attempting to decrease the cost and increase the amount of energy produced by these CSP facilities which could become a more viable way to produce sustainable energy with virtually zero carbon emissions to combat climate change.

One of the ways to increase the electricity production of CSP facilities is to increase

the temperature of the receiver and the molten salt. This can be done by using more mirrors to reflect the sun's rays or by focusing the mirrors on a smaller point, both of which can and have been done to produce higher temperatures. The issue lies in the molten salt itself; if the molten salt gets too hot, it suddenly becomes very corrosive to the traditional grade metal used for the receiver, pipes, and storage vessel that contain the molten salt. One way to combat this issue is to use a higher performance metal, but this can result in a significantly higher costs to build the CSP facility. Another way to achieve higher temperatures is to use sand particles of controlled sizes (as discussed in this work). Sand particles are non-corrosive and stay solid at much higher temperatures than the molten salt which would allow these CSP facilities to operate at higher temperatures. The issue is that there is no intuitive way to transport the solid particles - for molten salt, a specialized pump forces the liquid salt to move through piping.

Gravity aides in the transport of the particles, and these types of CSP facilities contain what is known as a "falling particle receiver." This concept concentrates the sun's rays on a continuous falling flow of particles to directly heat those particles (rather than the black-surface receiver used for molten salts). The heated particles may then either be used to transfer heat to a power cycle to create electricity or stored in an insulated storage tank to allow for continuous facility operation day and night – much like the process for molten salts. After the particles reach ground level, they are moved to the top of the CSP facility with either mechanical bucket elevators or pressurized air pushing the particles upward through vertical piping.

The knowledge gap that this work seeks to address is to determine how effectively the heat is transferred from the particles to the power cycle. For this concept, the hot particles would fall vertically (driven solely by gravity) through thin channels with a restriction at the

bottom. This restriction limits the number of particles exiting the channels with physical blockages and causes the particles to become packed tightly together as they flow downward. A fluid (called a heat transfer fluid) is flown over the exterior of these channels to absorb the heat from the hot particles through the channels and then uses that heat to drive a turbine to produce electricity. To clarify, the particles and heat transfer fluid are both in contact with the channels but not each other; the channels provide a barrier between the heat transfer fluid and particles – this is the heat exchanger. There is not much documented research on how well a packed bed, particle flow transfers heat to these channels in the heat exchanger. This work seeks to quantify the properties associated with the heat transfer of the high-temperature packed bed, particle flow to a specific channel design for a particle-based CSP facility. The results of this work will hopefully aide in future design of the channels/heat exchanger or particle selection for a particle-based CSP facility (as part of the Gen3 CSP project headed by the United States Department of Energy) to produce more and lower cost energy than has been done by a molten salt CSP facility. Various other countries are involved in a collaborative effort for particle-based CSP outside of the Gen3 CSP project. The ultimate goal is to reduce emissions by implementing renewable power generating facilities, such as CSP, across the world.

Abstract

High-temperature bulk thermal conductivity and heat capacitance were determined for six pure Silica particles and two Alumino-Silicate particles of various size distributions in a 75-800 micron range. The bulk thermal conductivities for the Silica sands are in the range of 0.33-0.64 $\frac{W}{m-K}$ over 220-815°C (which is in good agreement with other experimentation performed for the same Silica sands) and for the Alumino-Silicate sands are in the range of 0.27-0.45 $\frac{W}{m-K}$ over 235-670°C; the bulk thermal conductivity of all the particles increases non-linearly with temperature. As average particle size of the distribution decreases, the bulk thermal conductivity decreases. The specific heat capacitance for the particles is deemed to be the same as the bulk material, regardless of size distribution, and can be estimated using standardized values for the specific heat capacitance of the bulk material. The specific heat capacitance of the particles increases non-linearly with temperature, but there is a noted phase change in the crystalline structure of Quartz at 573°C which causes a step decrease in specific heat capacitance for the Silica and Alumino-Silicate sands. Next, heat transfer coefficients were determined for a packed-bed, particle flow of a specific size distribution of Silica sand in the range of 100-600 microns through a high aspect ratio, rectangular channel with a 3 mm gap. The heat transfer coefficients for this configuration are in the range of 200-400 $\frac{W}{m^2-K}$ over 10-190°C which are in good agreement with other literature; the heat transfer coefficient increased with temperature. The experimentally determined Nusselt number showed good correlation with the theoretically determined Nusselt number of 6 for this configuration.

Contents

Introduction

Concentrated Solar Power (CSP) is a form of renewable energy that relies on capturing and storing thermal radiation from the sun for use. Traditionally, the thermal energy from CSP has been used for power cycles to produce electricity or to aide in thermochemical industrial processes such as chemical production and water desalination [1]. The general facility setup for CSP includes an array of mirrors that reflect the sun's light towards a receiver as seen in Figure 1. The receiver captures the radiative heat and transfers it to a thermal storage medium which is usually a molten salt mixture [2]. The heated molten salt can be stored in insulated tanks which can retain a large fraction of its energy overnight, allowing CSP storage facilities to continuously run for 24 hours at a fraction of the cost compared to photovoltaic solar cells using battery storage [3]. When the thermal energy is required for processing, the thermal storage medium may be passed through a heat exchanger in order to transfer energy to a working fluid in a power plant or process.

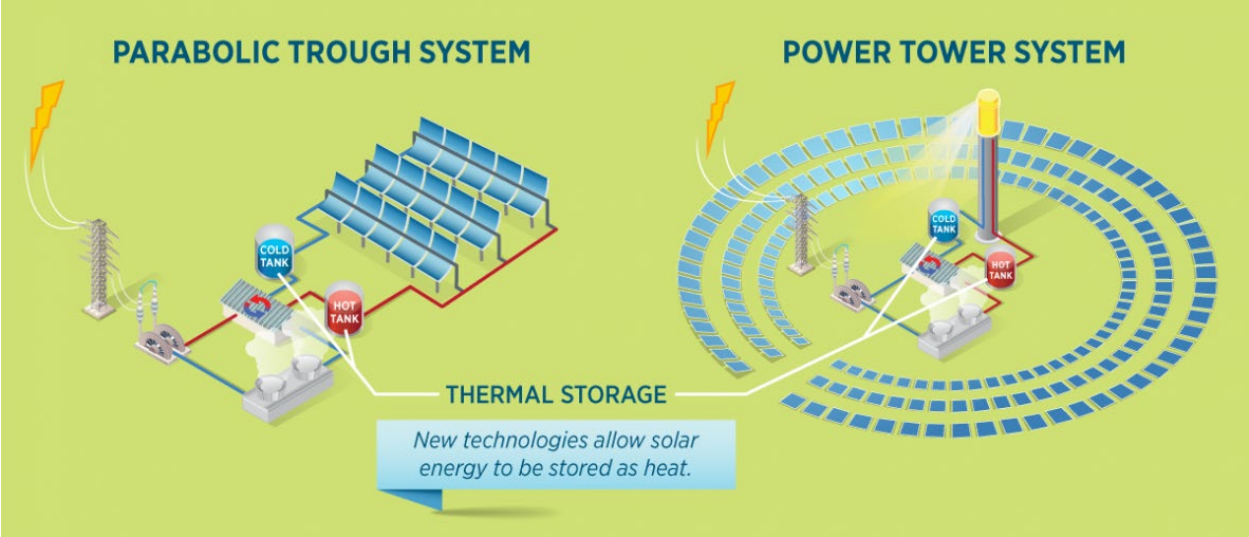

Figure 1 - Graphic depiction of the two main types of Concentrated Solar Power (CSP) facilities. This work is concerned with the power tower system [4]. One interesting application of the parabolic trough system is by a startup in Spain called Solatom; they build modular concentrators that fit in shipping containers and are used to create steam for thermal processes for individual customers and facilities [5].

CSP facilities are generally setup on hundreds of acres of flat land and in dry climates with high amounts of direct normal irradiation (e.g. exposure to the sun) such as in Spain or the southwest United States as shown in Figure 2 [6]. This technology was first implemented on a large scale in the 1980s following the build of the first parabolic trough plants called Solar Electric Generating Systems (SEGS) [6]. After 2005, new headway was made by the US and Spain in building commercial CSP sites as an alternative way to produce energy and reduce greenhouse gas emissions due to growing concerns regarding climate change [6]. Since then, CSP facilities are becoming more popular around the world as noted by the recent rises in facility creation and energy production as seen in Figure 3. CSP is still in its beginnings of lowering capital and production costs due to the 15-year hiatus of research and provides great promise as a dispatchable (i.e., low start-up and shutdown times) energy source with high-efficiency and low-cost, thermal storage capabilities [6]. Photovoltaics (PV) being less costly than CSP as a non-dispatchable energy source has encouraged research into dispatchability

and storage for CSP [6]. Progression into newer developments of hybrid PV and CSP with storage may offer a cost-effective and sustainable way to harness solar energy with 24/7 operation too [3].

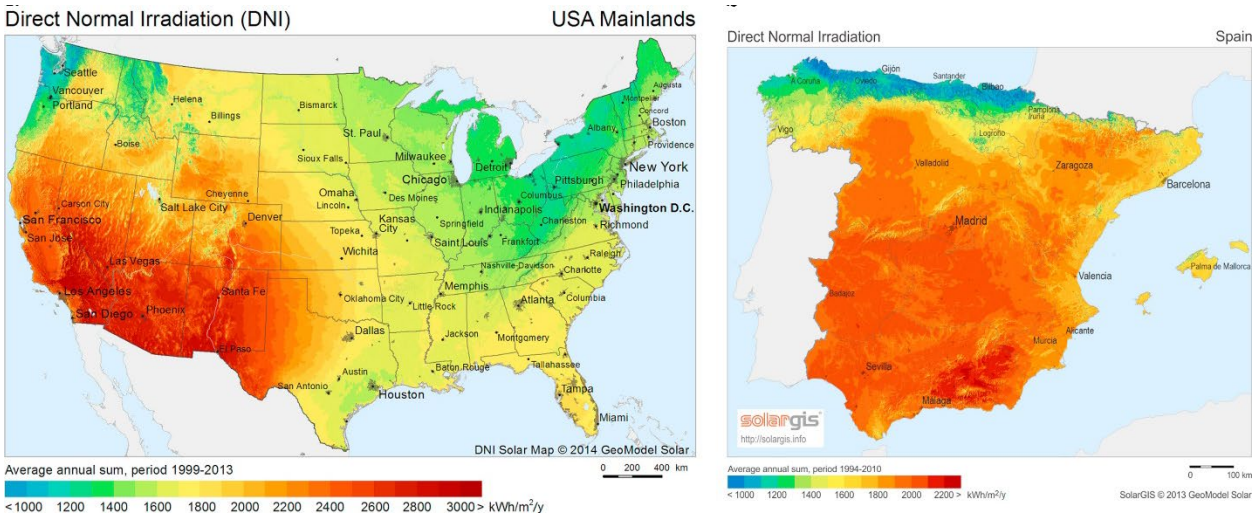

Figure 2 - Direct Normal Irradiation maps for the United States and Spain [7]

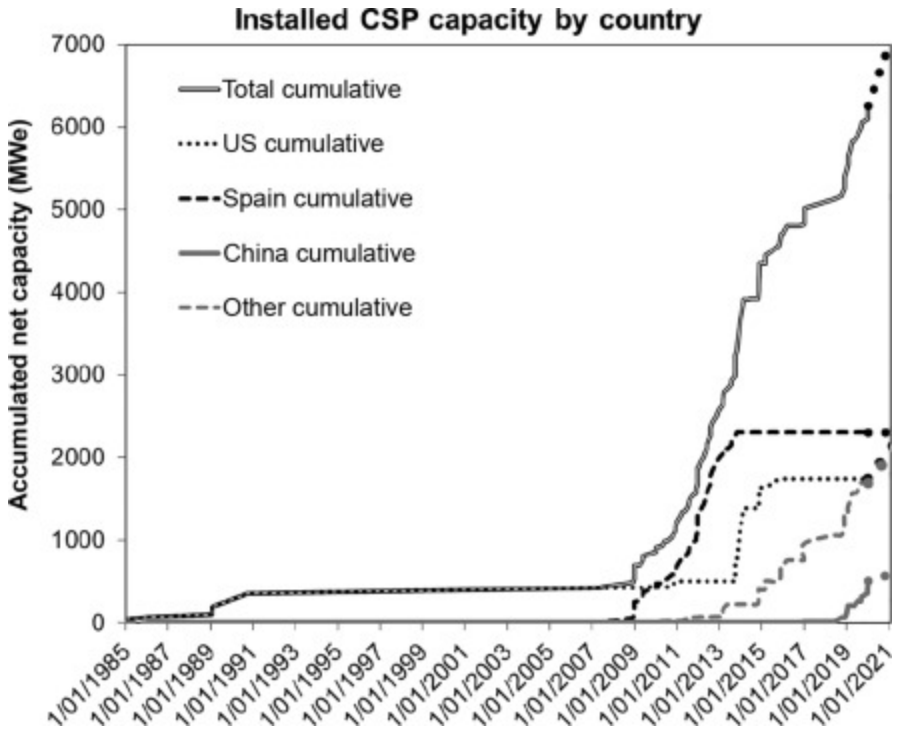

Figure 3 - Global CSP energy production since 1985 [6]

Solar One, implemented in the Mojave Desert by the United States Department of Energy (US DOE) in 1984 as an experimental facility, was the catalyst of the CSP movement [6]. Solar One used 1,818 heliostats with 39 m^2 of reflective surface each that pointed towards a single focal point to power a steam turbine cycle. This focal point was a 13.7 x 7 m receiver that absorbed a maximum of 45 MW_t in radiation and exchanged the heat from the radiation to the working fluid, steam or oil [6]. Solar One produced 10 MW_e (on scale for a hypothetical 10 MW_e facility) and also had the capability to thermally store energy in a rock, sand, and oil thermocline tank which could power the turbine to produce 7 MW_e for 4 hours alone [6].

Solar Two, completed in 1995 as an extension of Solar One by the US DOE and seen in Figure 4, added 105, 95 m^2 heliostats to the Solar One facility to produce 10 MW_e (the same amount as Solar One) and used molten salt, a mixture of 60% $NaNO_3$ and 40% KNO_3 dubbed

"solar salt," as the receiver heat transfer fluid and thermal storage medium [6]. This salt mixture was chosen as a result of its reasonable cost, nontoxicity, and good heat transfer properties [6]. Storing the heated molten salt above its freezing temperature in tanks allowed for the facility to continue to produce 10 MW_e [6]. Solar Two was decommissioned in 1999 before commercial operation due to costs associated with steam generator failure, blockages in the salt riser, and warpage developing in the receiver [6].

Figure 4 - Overhead of the Solar Two facility in the Mojave Desert [8]

Torresol Energy built the commercial Gemasolar, seen in Figure 5, which uses concepts from Solar One and Solar Two to create a 24/7 operational CSP facility using molten nitrate salt storage tanks [6]. Commissioned in 2011 in Seville, Spain, Solar Tres contains 2,650, 15 m^2 heliostats [6]. The 19.9 MW facility can produce 15 hours of electricity without sunlight

and was able to achieve continuous operation for multiple days on regular occasions which highlights feasible baseload usage for CSP via thermal storage [6].

Figure 5 - Gemasolar CSP facility located in Seville, Spain [9]

Although CSP has come a long way, there are still difficulties that are being addressed for these facilities. For one, the capital cost in building a CSP facility can require quite a bit of initial funding [6]. CSP needs to become cost-competitive with other forms of energy production to be viable; the SunShot Initiative by the US Department of Energy met the goal of reducing baseload energy rates to 6 ¢ per kW-hr by 2020 and now has the objective to further reduce to 3 ¢ per kW-hr by 2030 [10]. The facilities also require hundreds of acres and need to be located in areas with high direct normal irradiation [6]. Some additional operational issues include but are not limited to:

- Keeping the heliostats clean of dust for the most reflective surface as well as cooling can require water and cleaning agents which can be difficult to source in desert areas [7]
- Preventing freezing of solar salt and managing corrosivity of the salt used for the thermal storage medium [6]

The purpose of this project is to explore alternative pathways to address the issues in the final bullet point.

While the solar salt that has been used in CSP plants previously is fairly cheap at 50 ₡ per kilogram, it has an upper operating limit of approximately 565°C at which point the salt becomes too corrosive to operate within 316 and 304 Stainless Steel facilities [11] [12]. Increasing the temperature of the thermal storage medium provides the benefit of a resulting hotter working fluid when the heat is passed to the power cycle which can lead to greater energy yield. To increase the upper temperature limit of CSP facilities, one alternative pathway that is being explored by this project is the use of solid particles, specifically various sized Silica and Alumino-Silicate sands, as a thermal storage medium in place of solar salt.

These particles are thermally stable past 900°C but have a volumetric heat capacity lower than solar salts [12] [13]. One of the biggest issues with particles is circulation: although particles can be gravitationally driven downward, there is no intuitive, inexpensive way to recirculate the particles to the top of a facility without significant heat loss [14]. Novel concepts include using bucket lifters or fluidizing and driving the particles vertically with a pressurized gas flow as seen in Figure 7. Along with this, the thermophysical properties of these particles and their flow behavior are not well-documented at high temperatures.

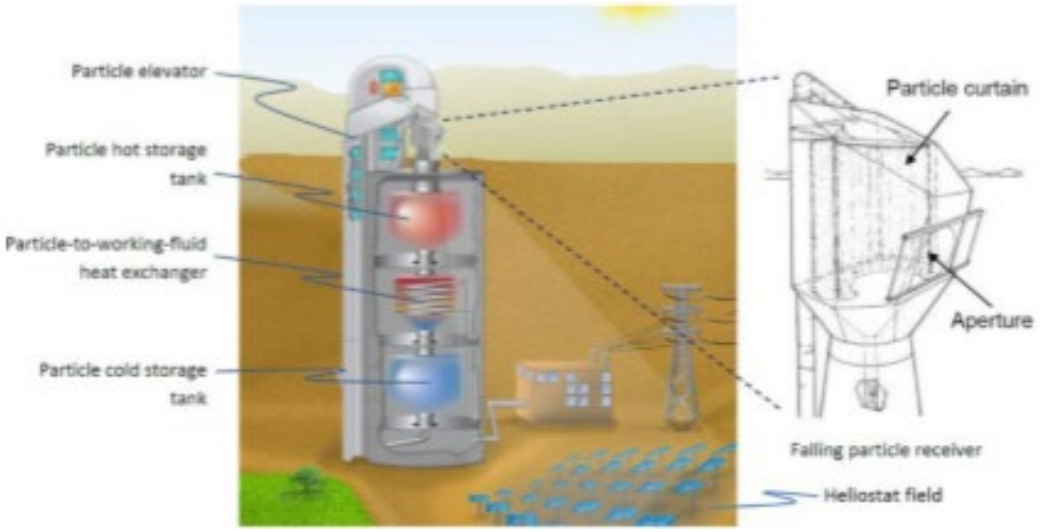

Figure 6 - Particle bucket elevator for transporting particles in a CSP system [15]

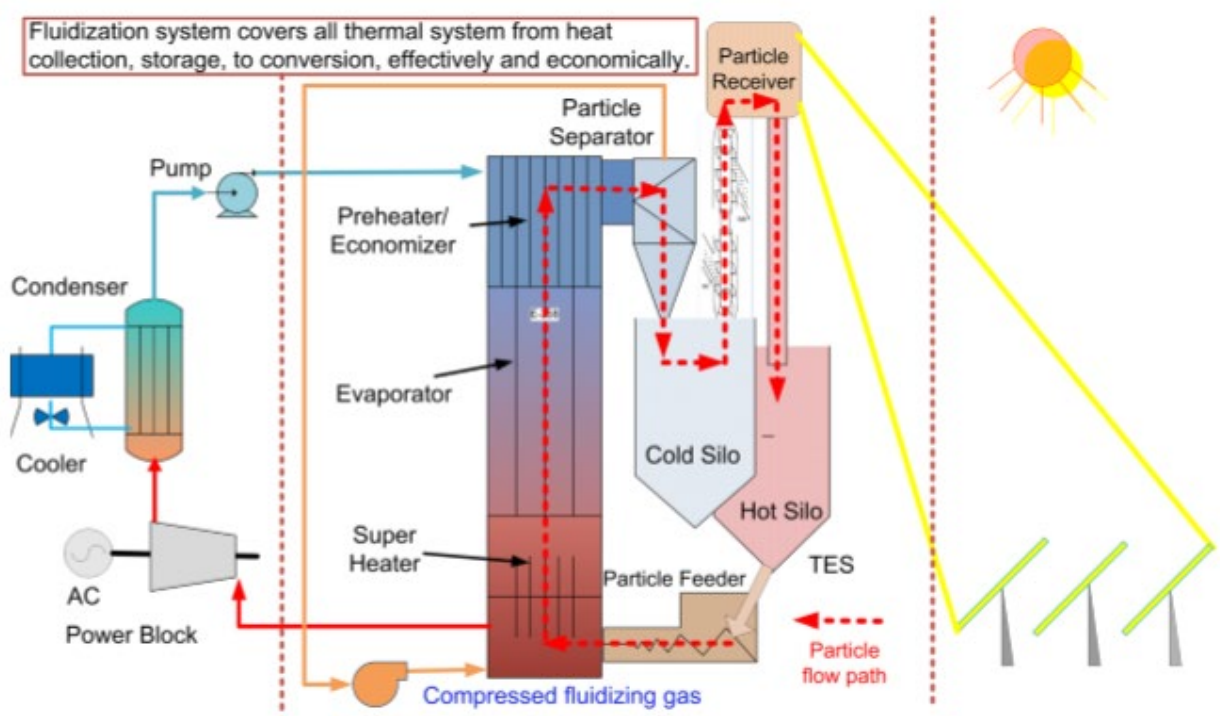

Figure 7 - Fluidized bed recirculation of particles in a CSP system [2]

The purpose of this project is to determine the static thermophysical properties, such as conductivity, interface resistance, and heat capacitance, of these particles in question between

and below 520°C-800°C as well as the behavior (i.e., the heat transfer coefficient) associated with a flowing, packed-bed of heated particles. As discussed later, the interface resistance of the particles was unable to be determined. Similar work has been done with alumino-silicate and zirconia-silica particles in [16] and bauxite particles in [17] and [18] that produced heat transfer coefficients in line with this work.

Static Testing Rig Design for Conductivity and Heat Capacitance

The first experimental facility built is a static setup, meaning non-moving particles, to determine conductivity and heat capacitance. The basic premise of the static facility is to apply a heat flux on one end of the particles to induce a temperature gradient with respect to position at steady state conditions to determine thermal conductivity, summed up by a simplification of Fourier's law of conduction:

$$\dot{Q} = -k\, A_c \frac{dT}{dx} \qquad (1)$$

where $\dot{Q}$ is the heat input, k is the thermal conductivity, A_c is the cross-section, and $\frac{dT}{dx}$ is the temperature gradient. Equation (1) assumes that the material is isotropic and has a uniform heat flux applied that travels only in one direction through a cross-section. In terms of heat capacitance, the transient data from the experimental facility can be used via application of the following simplified equation for lumped capacitance:

$$\dot{Q} = c_p\, \rho\, V \frac{dT}{dt} \qquad (2)$$

The assumptions made with Equation (2) are that the heat capacitance (c_p), density (ρ), and volume (V) of the material are independent of time and temperature and that there are no temperature gradients with respect to position within the material. $\frac{dT}{dt}$ represents the derivative of temperature with respect to time. The complication of building such a facility is that a directional temperature gradient is required to satisfy Equation (1) and determine conductivity, yet there cannot be any directional temperature gradients to satisfy Equation (2) and determine heat capacitance.

A double-sided, guarded hot plate (GHP) as described in ASTM C177-19 [19] is the basis for the design of the static test facility (see Figure 8). GHPs are a standardized way to determine thermal conductivity using the positional temperature gradient at steady state. The GHP in ASTM C177 uses a hot plate to apply heat to the specimen and cold surface assemblies to ensure a uniform temperature across the cross-section of the "cold" side of the specimen. Heater guards, insulation, and shroud ensure unidirectional heat flow across the specimen. The insulation and shrouding offer thermal resistance to ensure heat only flows along the intended direction. The heater guards require a feedback loop to determine how much heat must be produced by the guards to approach a net zero heat loss out the sides of the specimen. The controlled environmental chamber ensures a constant pressure of a certain fluid to encompass the specimen.

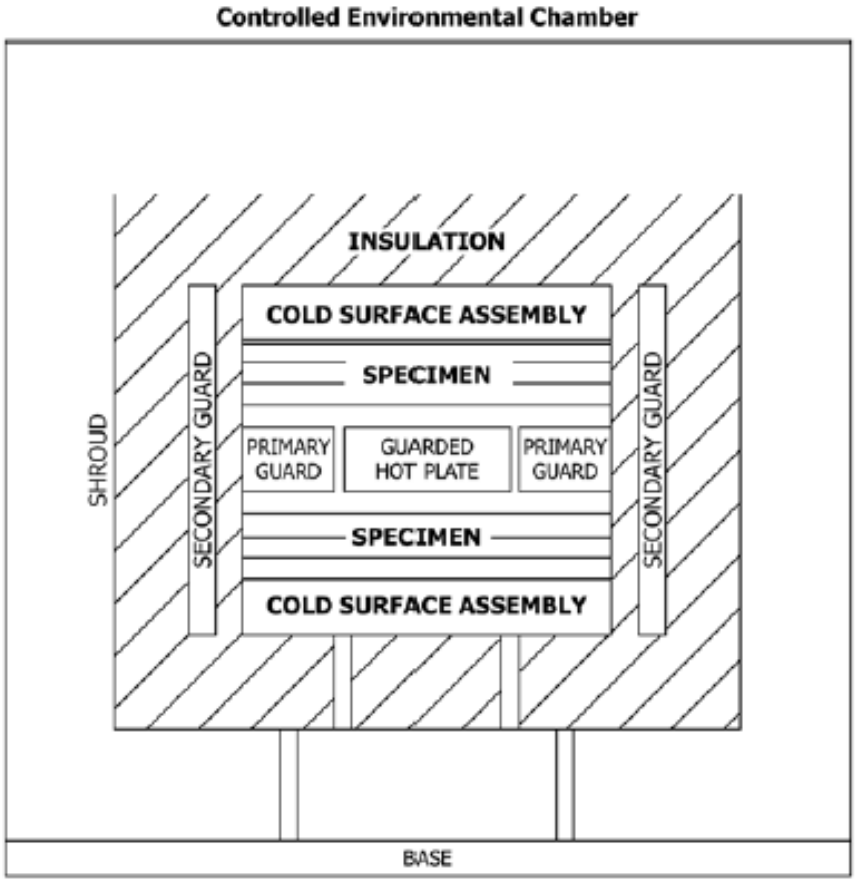

Figure 8 - Cross-sectional depiction of the double-sided, guarded hot plate apparatus as described by ASTM C177. Picture taken from ASTM C177.

There is also a one-sided GHP design described by ASTM C177, but it is difficult to either add a guard plate on the backside of the specimen with feedback to ensure heat flow only through the specimen or account for the heat loss through the backside of the heater plate through the insulation. Using symmetry, this GHP is double-sided in that the specimen is placed on both sides of the heater to ensure there is equal and opposite heat flow from the hot plate.

A radial GHP design, like that in [16], deviates from the ASTM C177 [19] and was also considered because the radial design has the inherent symmetry of the double-sided GHP.

The radial design was abandoned because of the complexity to put either the hot plate or cold surface assembly on the exterior of the radial design and ensure uniform heat flow. Thus, the double-sided GHP is the base design selected.

There are a couple design deviations from the ASTM C177 [19] standard. For one, high temperature, high performance insulation is used in placed of the heater guards. If the heat loss is determined to be too large after running experiments, heater guards would be installed. The controlled environment chamber is also unnecessary because the particles are intended to operate in an open environment in the actual CSP application. Also, the base and shroud seem to be unnecessary additives to the experimental rig. Without heater guards, the static test rig is dubbed an Insulated Hot Plate (IHP) rig.

Experimentally, ASTM C177 [19] advises that a constant heat flux is applied to the specimen until steady state is reached. At this point, thermal conductivity of the specimen can be found by using spaced temperature readouts placed inside the specimen such as shown in Figure 9.

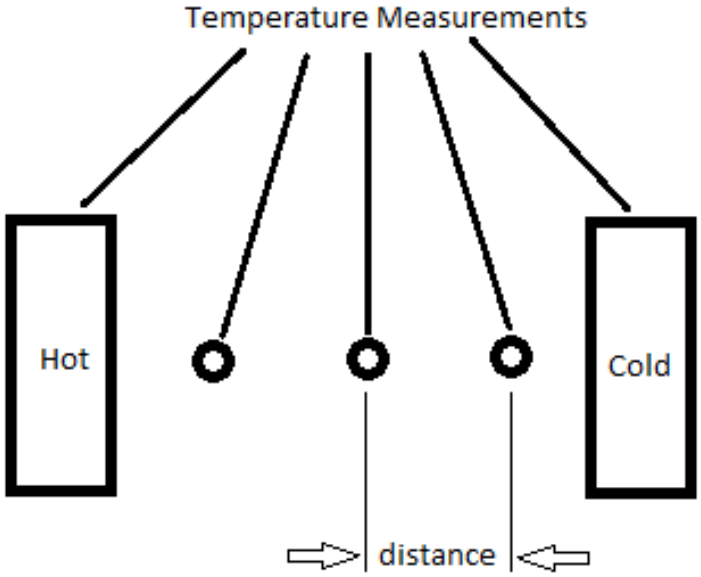

Figure 9 - Drawing that describes how temperature measurements are taken within the GHP

With knowledge of the heat input, cross-sectional area of the specimen, the temperatures at the probes, and the distance between the temperature probes, conductivity becomes the only unknown from Equation (1), approximating the temperature gradient with the probes' temperatures and distances from each other. For example, given two thermocouple (TC) temperature probes, TC_1 and TC_2, and their relative locations, x_1 and x_2, the term for the positional temperature gradient can be approximated as:

$$\frac{dT}{dx} \approx \frac{TC_1 - TC_2}{x_1 - x_2} = \frac{\Delta T}{\Delta x} \qquad (3)$$

It should be noted from Equation (3) that a larger temperature difference (ΔT) and a larger positional difference (Δx) results in a smaller uncertainty value for the overall approximated positional temperature gradient. To achieve a larger temperature difference (ΔT) and smaller uncertainty, the cross-sectional area in the direction of the heat flux (A_c) of the specimen must

be smaller, the heat input ($\dot{Q}$) must be higher, and/or the specimen must have a lower thermal conductivity (k). To achieve a larger positional difference (Δx) and smaller uncertainty, the temperature probes must be spaced further apart.

Decreasing the cross-sectional area or lengthening the distance between probes (and thus overall length of the GHP) both result in increasing the thermal resistance in the intended direction of heat flow as shown in Equation (4). Using similar assumptions to Equation (1), the thermal resistance due to conduction along the intended direction of heat flow can be described as:

$$R_{cond,x} = \frac{\Delta x}{k\, A_c} \qquad (4)$$

The thermal resistance due to conduction perpendicular to the intended direction of heat flow can be approximated as:

$$R_{cond,\perp} = \frac{\sqrt{A_c}/2}{k\, \Delta x\, \sqrt{A_c}} = \frac{1}{2\, k\, \Delta x} \qquad (5)$$

Equation (5) assumes that there are two thermal resistances in parallel originating from the centerline of the intended direction of heat flow and extending towards the sides. Taking the ratio of the resistance due to conduction in the intended direction to that in the perpendicular direction:

$$\frac{R_{cond,x}}{R_{cond,\perp}} = \frac{2\, \Delta x^2}{A_c} \qquad (6)$$

In an ideal scenario, the ratio of resistances described by Equation (6) would be low such that there is less thermal resistance along the intended direction of heat flow compared to the

resistance perpendicular to the intended direction of heat flow. To achieve this, Δx must be small, and A_c must be large. Yet, to achieve a lower uncertainty for the positional temperature gradient described by Equation (3), Δx must be large, and A_c must be small.

While a lower conductivity and greater heat input would result in a lesser uncertainty, a non-uniform heat flux applied to the specimen can result in temperature gradients across the cross-section of the specimen for an IHP design without heater guards (e.g., vertically and in the plane of the page in Figure 9). For example, if the heater has a greater heat flux at the centerline than the edges of the cross-section, then a lower conductivity or larger heat input would result in larger temperature gradients from the centerline to the edge of the specimen. To limit this scenario, high-performance, high-temperature insulation providing significant thermal resistance needs to be used to surround the specimen, and special care has to be taken to ensure the heat flux applied by the heater and the temperature of the cold surface assemblies are nearly uniform across the cross-section.

Interface resistance between the particles and the wall ($R_c^{"}$) could be calculated using the following:

$$\dot{Q} = \frac{TC_{close} - TC_{wall}}{R_{cond,x} + {R_c^{"}}/{A_c}} \qquad (7)$$

where $R_{cond,x}$ can be found using Equation (4) such that Δx is the distance between the closest thermocouple to the wall in the sand and the wall, TC_{close} is the temperature closest to the wall in the sand, and TC_{wall} is the temperature of the wall. Based upon initial estimates, the interface resistance is estimated to have an absolute uncertainty of at least 50% using Equation (7). As

mentioned later, temperature measurements of the wall were unable to be taken in the static rig, so the interface resistance could not be determined.

The static rig has a 10.2 cm specimen gap for the particles on each side of the heater with a 30.5 cm by 30.5 cm cross-section. A square cross-section is preferred over rectangular in terms of symmetry, and having existing 15.25 cm by 30.5 cm Aluminum water channels to use for the cold surface assembly was the design rationale for implementing a 30.5 cm by 30.5 cm cross section. A value of 10.2 cm for the specimen gap gave a value of 0.22 for Equation (6) which seems reasonably low and, along with insulation, ensures that there would not be significant parasitic heat loss. This gap size of 10.2 cm also allows for a number of temperature measurements to be taken along the sand gap extrapolate a temperature gradient such as in Equation (3). The static rig size is fairly compact and requires about 19 L of specimen to test, enough to account for any variety in the particles being tested but not so much that the amount of sand would be expensive to acquire or too difficult to handle. Figure 10 and Figure 11 show the finalized design and build of the static rig:

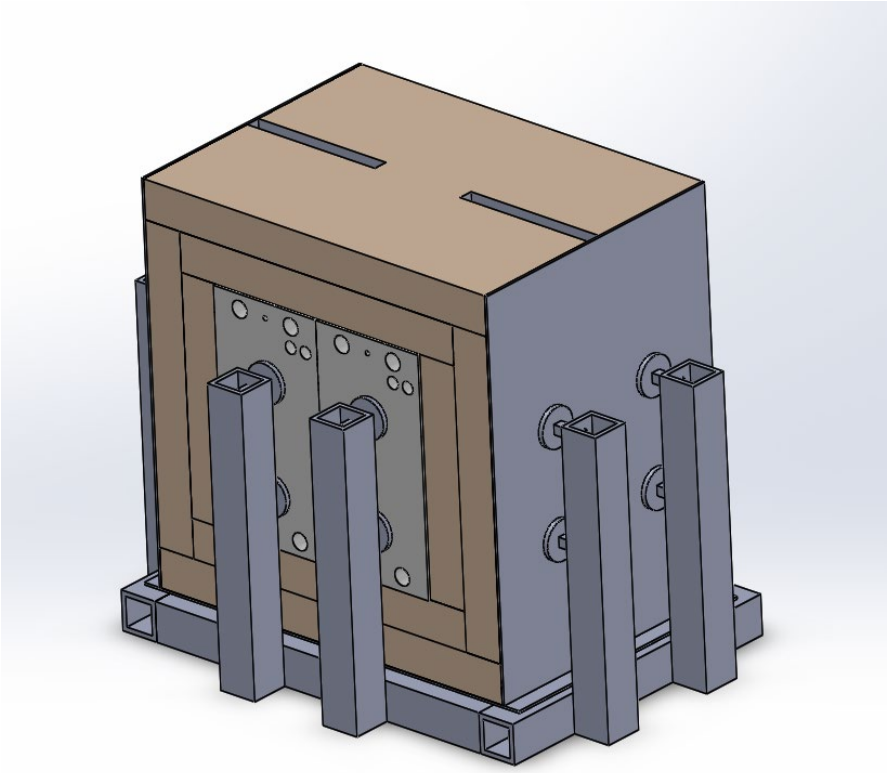

Figure 10 - Isometric of the CAD Static Sand Rig. The Static Sand Rig sits within an exterior square tube housing that supports the rig

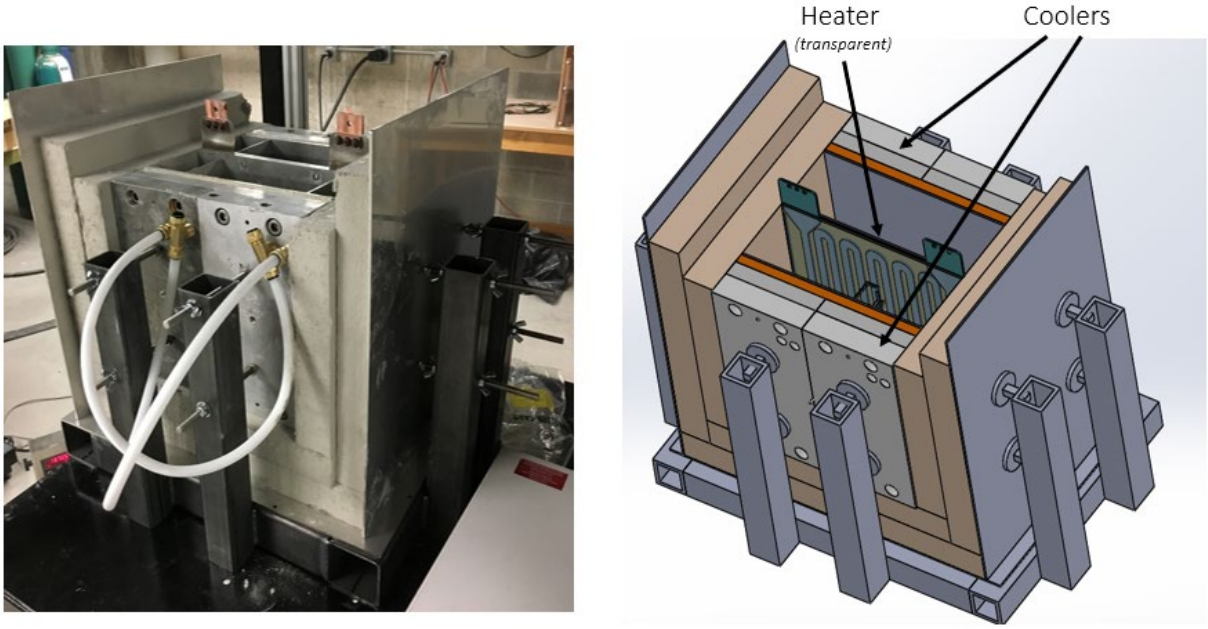

Figure 11 - Isometric of the Static Sand Rig with an open top. Sand would be filled on both sides of the heater plate.

There are 12 thermocouples spaced evenly apart at 8.8 mm increments with 2.54 mm of space between the edge thermocouples and the hot and cold walls. These thermocouples are supported and located by thermocouple rakes – very thin, long tabs extending from either the hot or cold plates with holes sized to fit the thermocouple probe. Two rakes are attached to each plate at a 90° angle so that the thermocouple probes can be fed through both rakes and held in place:

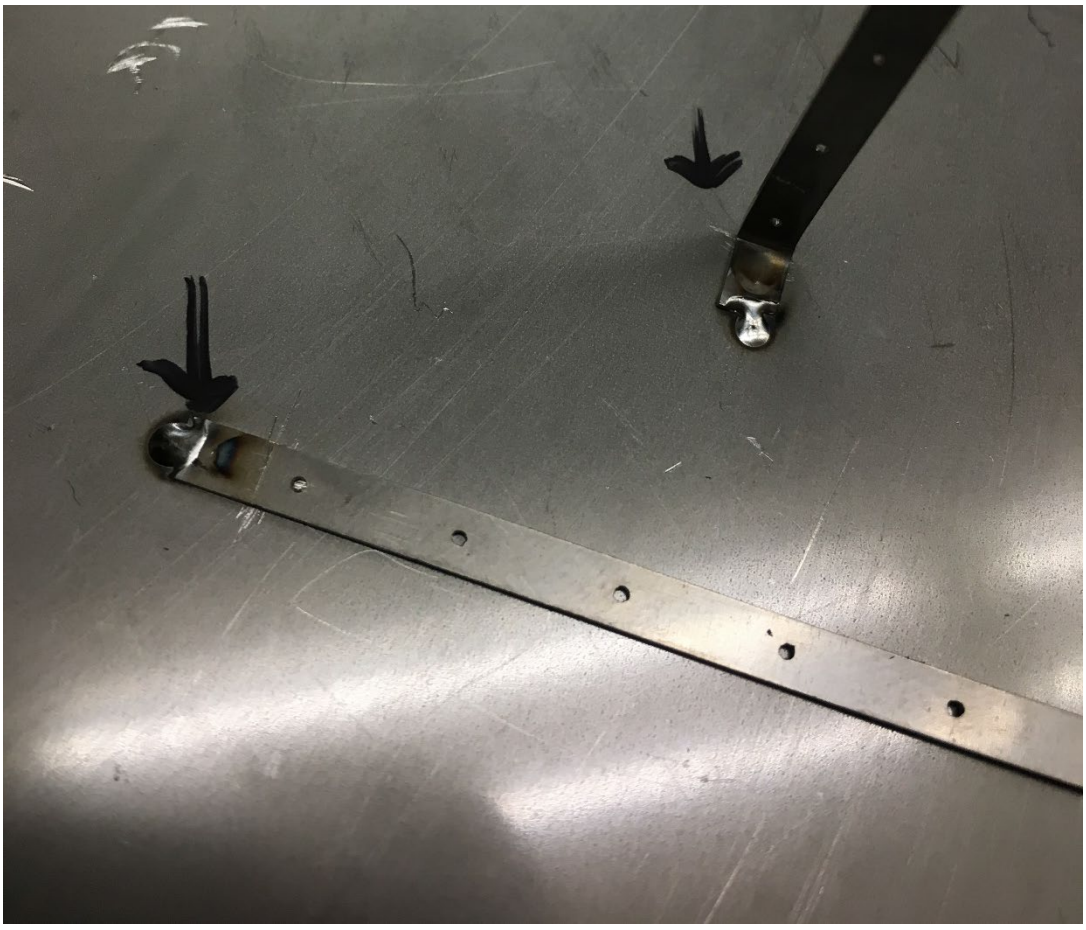

Figure 12 – Two thermocouple rakes welded to one of the plates. The bottom rake has yet to be bent.

Fiber optic temperature sensors housed in 316 Stainless Steel, 0.8 mm OD capillary tubing in conjunction with a Luna ODISI-B system are also used to verify temperature measurements.

The heat is supplied by a 0.5 mm thick, Inconel serpentine heater via ohmic heating; the serpentine heater resistance is approximately 0.5 Ω. The cold surface assemblies consist of water coolers to keep the plates at 20°C. Three sheets of 5 mm thick, Aspen Aerogel's Pyrogel XTF insulation is included between the sand gap and the cold surface assembly to offer thermal resistance and raise the temperature of the sand gap. The Pyrogel sheets are compressed to 14 mm of thickness via bolts through the cold plate into the water coolers.

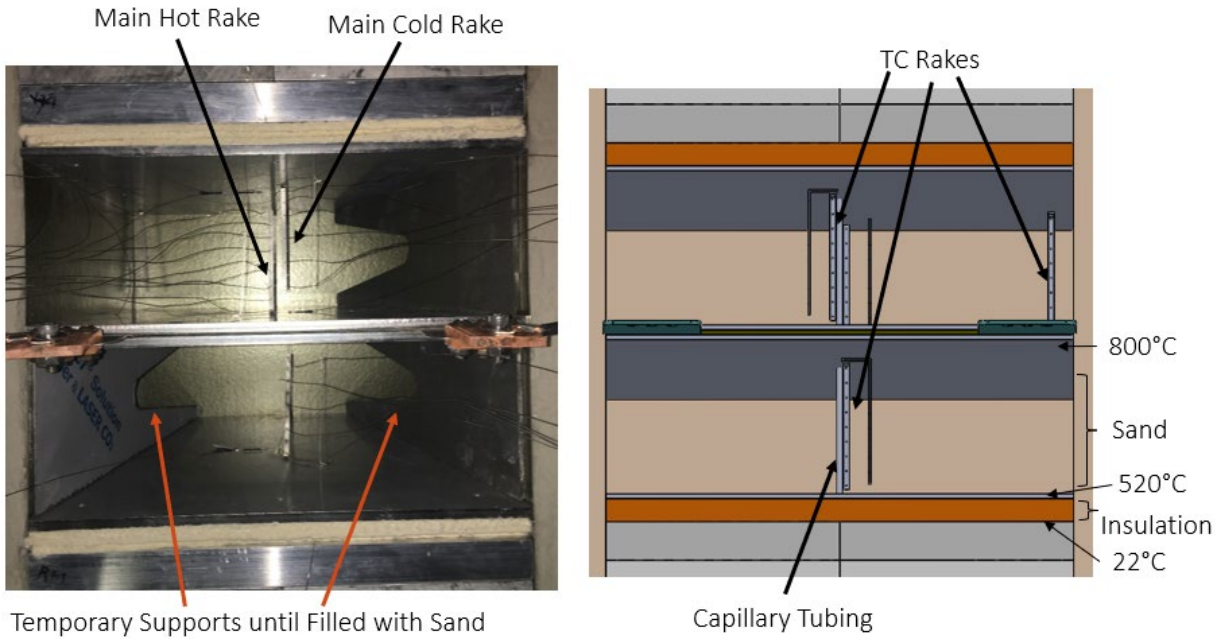

Figure 13 - Outlay of the interior of the static sand rig with labeling showing expected temperatures. These temperatures are symmetrical on the other side of the heater too.

The entire test section is surrounded by staggered 5.1 cm thick Promat Microtherm Promalight 1000x PE board, such that there are no wide-open gaps in the Microtherm insulation assembly, to create a total 10.2 cm thick insulating surrounding. There are no physical connections across the sand gap or the Microtherm insulation because those physical connections could act as thermal bridges. All of the components are held in place by their own

weight as well as light compression provided by the exterior, square tube support structure as seen in Figure 14.

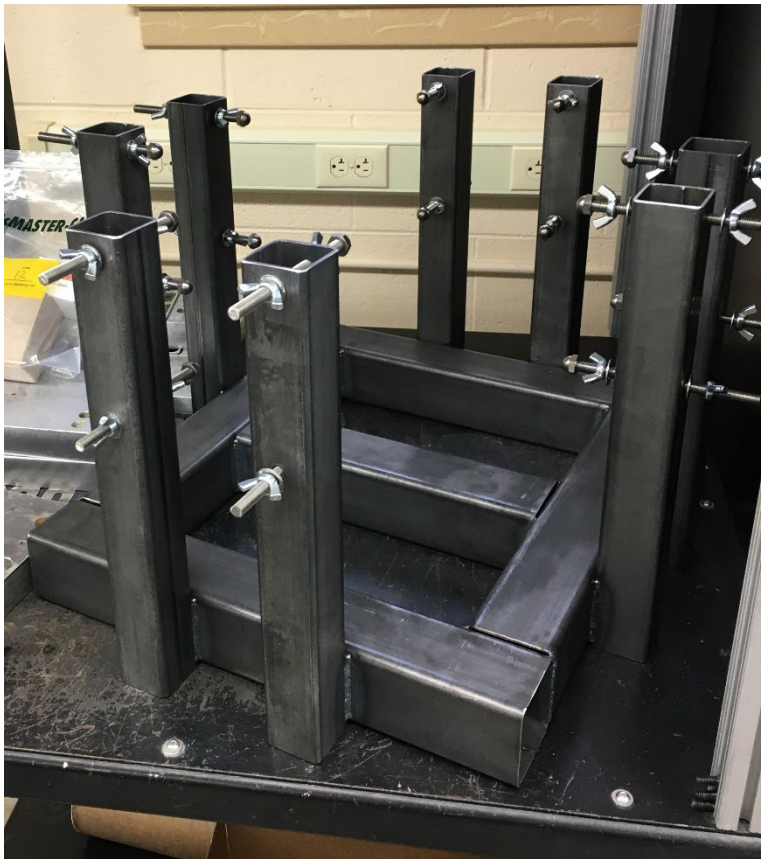

Figure 14 - Square tube support structure used to house the Static Sand Rig

For the hot plate assembly, the Inconel 600 serpentine heater is bolted between two 6.4 mm thick, 30.5 cm by 30.5 cm Inconel 600 Plates. A Xantrex XDC 40-150 DC power supply wired to the serpentine heater via copper leads is used as a constant current source with varying voltage to provide ohmic heating. The serpentine heater leads have to be extended 5.1 cm outside the insulation to ensure that conduction down the leads did not result in the melting of the wire's insulation connected to the leads. 0.5 mm thick Phlogopite Mica sheets are placed between the serpentine heater and the Inconel plates to provide electrical insulation as well act

as a thermal spreader; Mica's conductivity along the plane of the sheet is 10x greater than the conductivity into the plane of the sheet. The Inconel plate also acts as a thermal spreader because its thermal resistance along its cross-section is comparable to the thermal resistance into the sand. To verify that the temperature of the plate would be fairly uniform, a 2D FEHT model uses adiabatic symmetry to isolate a single portion of the serpentine heater's contact with the plate and gap. The maximum temperature difference along the cross-section of the hot plate in contact with the sand (i.e., rightmost edge of the hot plate in Figure 15) is less than 0.25°C which is insignificant. This model did not include the mica sheets, so the temperature across the cross-section of the hot plate in the experiment should be nearly uniform with the addition of the mica.

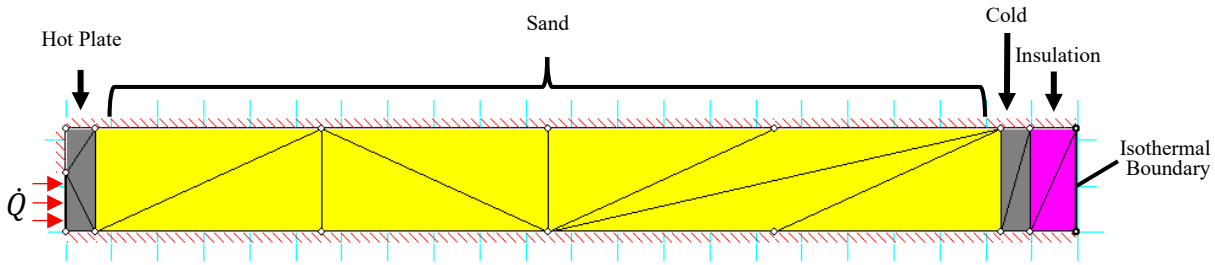

Figure 15 - Minimally meshed version of the 2D FEHT model used to determine if there were significant temperature gradients along the cross-section of the heater. Heat flux is only applied to half of the left side of the model. Dashes indicate lines of adiabatic symmetry.

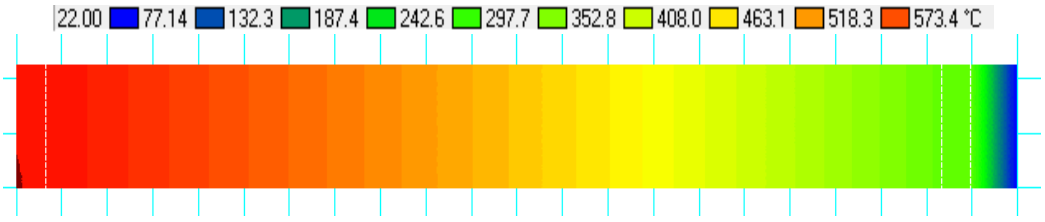

Figure 16 - Temperature profile of the 2D FEHT model from Figure 15. This model has a much finer mesh.

For both of the cold surface, water cooler assemblies, two 15.25 cm by 30.5 cm 6061

Aluminum water channels are bolted to a flat, 30.5 cm by 30.5 cm 6061 Aluminum plate. Rubber O-rings are used to seal the channels against the plate. The two water channels within a single assembly are plumbed in parallel while the two assemblies are plumbed in series to an FTS RS33AL11 temperature-controlled, recirculating cooler with a 60/40 mixture of propylene glycol and water as the refrigerant. The cooler has an internal centrifugal pump rated for 2 gpm at 4 psi and can remove heat at 1050 W at 20°C. Estimates of the pressure drop through all the piping is very minimal (less than 0.1 psi) and can be handled by the recirculating cooler's pump. An energy balance shows that even at max heater power, there will be less than a 1°C temperature rise in the water when it exits the water channels. The water cooler assembly has a total of 3.8 cm thick of Aluminum which ensures an isothermal cross-section at the cold end.

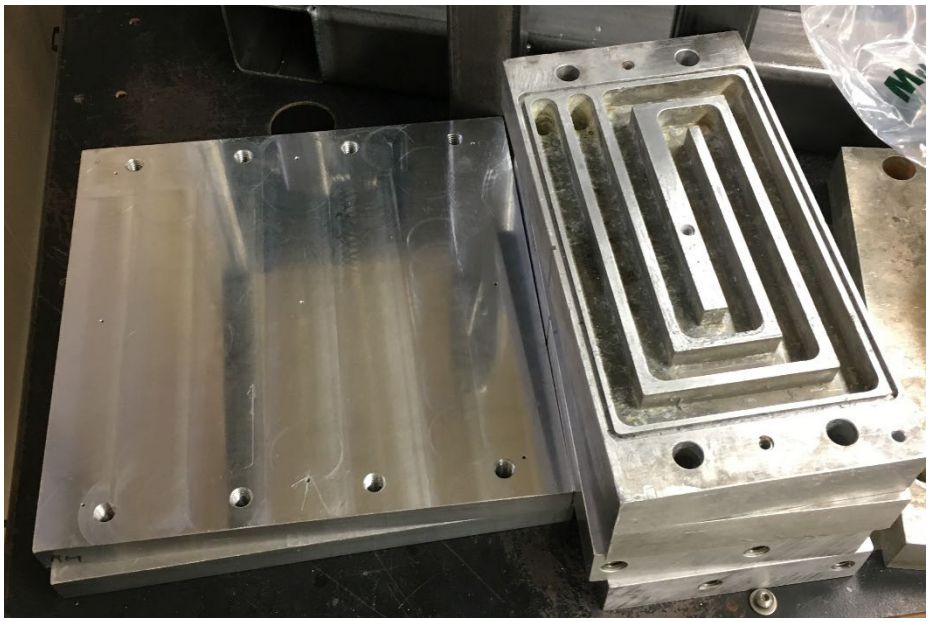

Figure 17 - Aluminum plates (left) and water channels (right) used to for the water cooler, cold surface assembly

Though the square tubing support structure limits the amount of thermal bridging by

removing the necessity of internal supports, there still is thermal bridging due to the 304 Stainless Steel thermocouple rakes and 316 Stainless Steel, capillary tubing for the fiber optic temperature measurements. The issue with this thermal bridging is approximated to be fairly insignificant with regards to affecting the temperature profile of the sand, but care had to be taken to ensure the thermal bridging across the thermocouple rakes is not significantly affecting the actual temperature measurements taken by the thermocouples. The Omega, type-K thermocouple probes themselves are as small as possible (0.5 mm in diameter) in order to limit conduction along the probes. To ensure the thermocouple junction did not experience any of the thermal bridging from the rake, the end of the probe needs to be at least 2.5 mm away from the rake. This distance is determined by treating the thermocouple probe as an extended surface in the sand and requiring that the resistance of conduction along the probe to be approximately two orders of magnitude greater than the resistance associated with conduction into the sand. Similarly, the resistance of conduction along the thermocouple rake and the capillary tube before the first temperature measurements are about two orders of magnitude greater than the resistance of conduction into the sand.

Another consideration with thermal bridging arose from the fact that there are eight, 316 Stainless Steel #2-56 bolts used to hold the cold plate to the water cooler assemblies that pass through the Pyrogel insulation. The bolts are intended to be as small and sparsely used as possible to limit this effect. This can cause localized cold spots to occur at the head of the bolts in contact with the sand. The effective thermal resistance of the Pyrogel with the eight bolts is approximately 20% less than the resistance of the Pyrogel insulation alone. This raises some concerns about these bolts that are considered in experimental analysis and will be discussed

in the next section.

Temperature measurements are primarily taken with 32 total Omega thermocouples with Inconel sheath 0.5 mm in diameter. These thermocouples are hooked up to two NI-9213, 16 channel thermocouple cards on a cDAQ chassis that is operated and records measurements via LabVIEW. The thermocouples are placed primarily along the centerline of the main gap, TC2-TC16, (North in Figure 18) and secondary gap, TC21-TC25. Note that these gaps are nominally identical and so the assignment of one to be the main gap and the other the secondary gap is arbitrary. Thermocouples were potted to the hot and cold plates (TC1, TC20, and TC26) with Aremco Cermabond 571 thermal epoxy, but the epoxy did not stick during experimentation, making these wall temperatures unreliable. Thus, the interface resistance could not be extracted. There are also thermocouples placed along the lower West corner of the main gap (TC17-19), within the Microtherm blocks and Pyrogel insulation (TC27-30), and in the outlet plumbing of the cooling assemblies (TC31 and TC32). Aside from TC29 and TC30 which are in between the Microtherm blocks on the center East side, all thermocouple locations are shown in Figure 18.

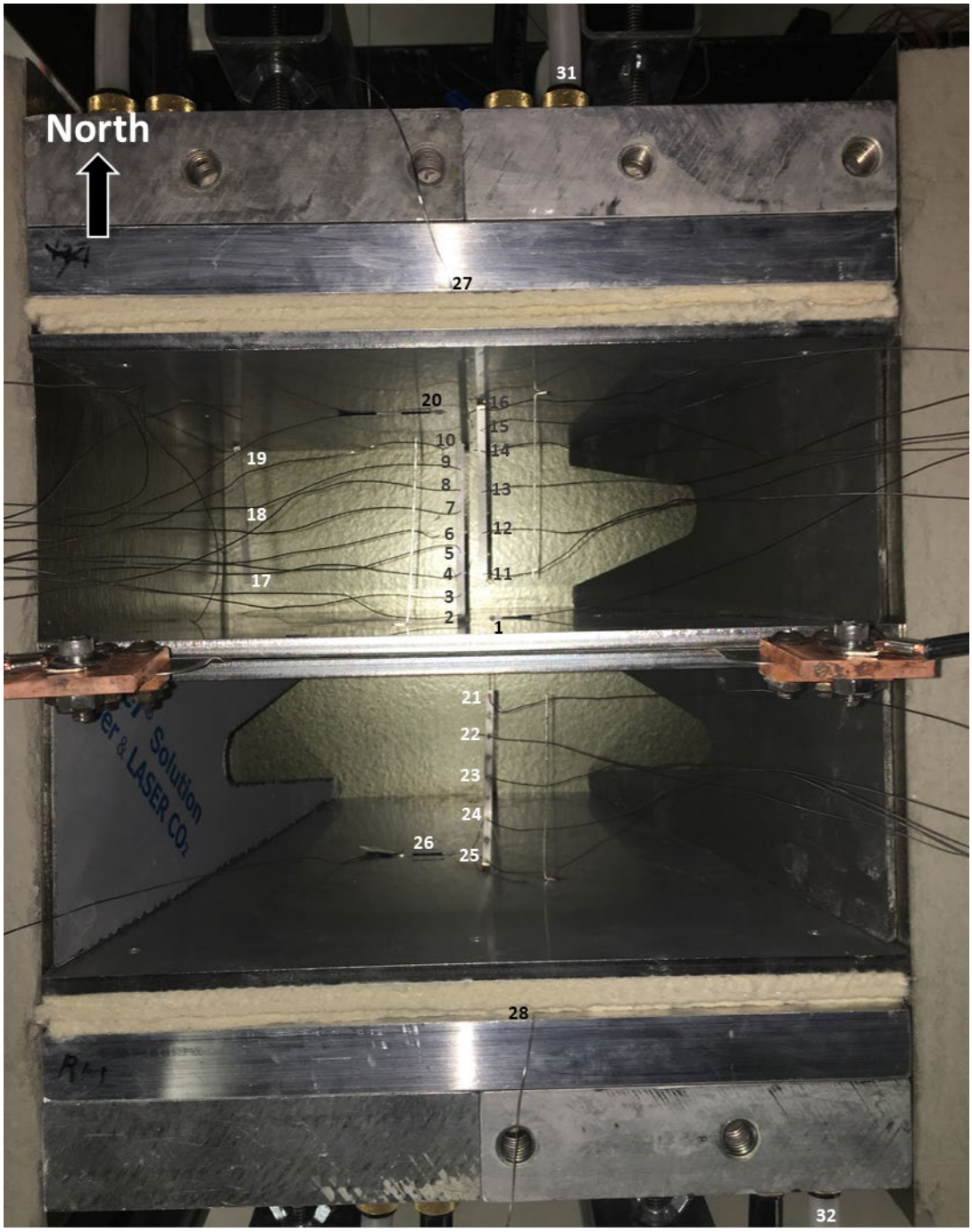

Figure 18 - Overhead of where the thermocouples presided within the static sand rig. The North gap is the main gap. Black and white numbers are solely for contrast of the text on the background. TC31 and TC32 measured the outlet temperature of the refrigerant for the cooling plates. Not pictured: TC29, in between two sheets of Microtherm on the East center, and TC30, on the outside wall of the Microtherm on the East center

As a secondary measurement, a fiber optic temperature sensor with a loop termination

feeds through 0.8 mm OD x 0.5 mm ID 316 Stainless Steel capillary and measures the temperature along the entire centerline of the rig. A Luna Innovations ODiSi-B system [20] collects data from the fiber at a spatial resolution of 0.65 mm between each temperature measurement. The basic principle of the temperature sensing fiber is that it uses Rayleigh backscattering to detect changes in crystalline structure of the silica fiber due to thermal strain; this strain can be correlated to temperature. Ultimately, a baseline strain for the fiber needs to be read at a known temperature (generally ambient), and any deviation of strain and thus frequency shift in the signal at certain points in the fiber directly correlate to a change in temperature. An in-house correlation [21] is used to correlate frequency shift to temperature:

$$T = (-8.18 * 10^{-5}) * S^2 - 0.667 * S + 26.17 \quad (8)$$

where T is temperature in °C and S is frequency shift in GHz.

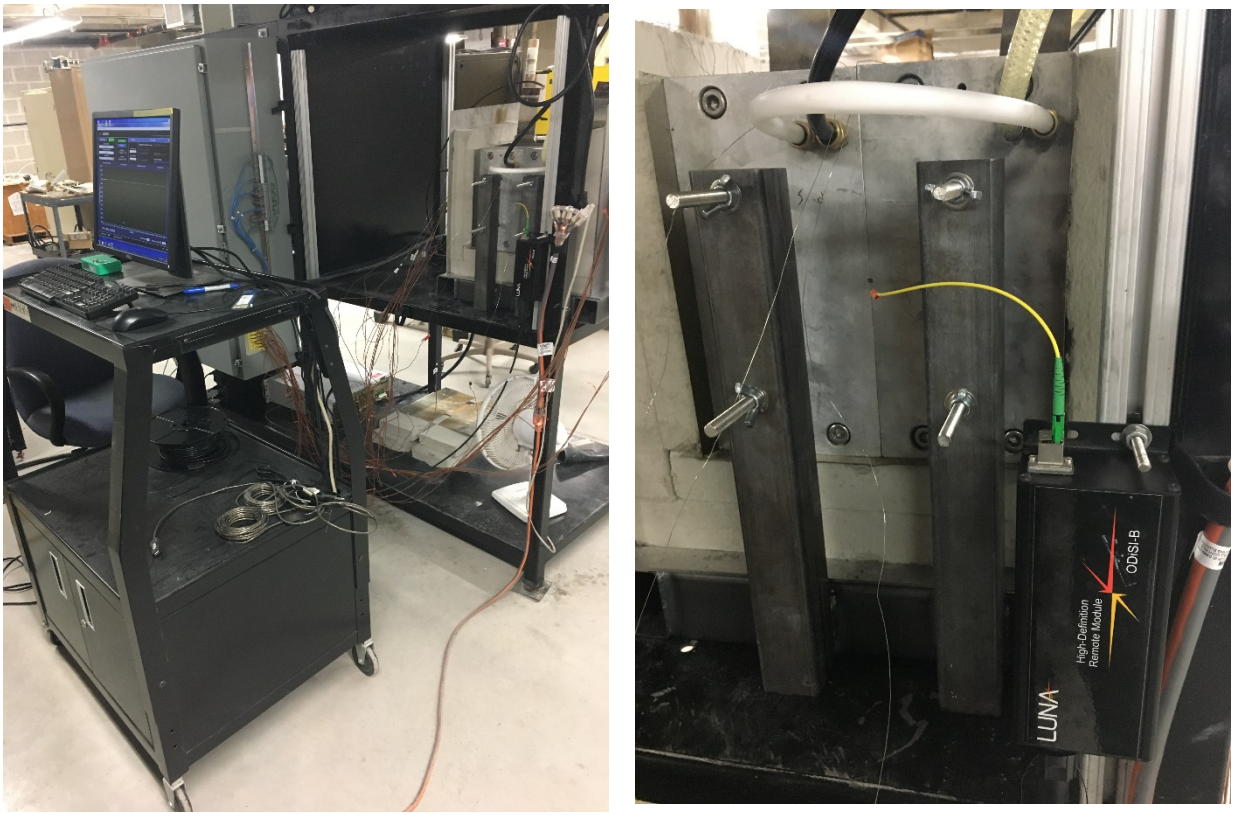

Figure 19 - Luna ODISi-B system in conjunction with the static sand rig

As a verification of temperatures within the rig, the temperature sensing optical fiber is compared to the rake of thermocouples. The fibers show good agreement with the rakes as shown in Figure 20 and Figure 21. The fiber malfunctions above temperatures of 650°C which compromised fibers at higher temperature runs [21]. Because fibers had to be rebuilt entirely after each high temperature test, not all sands have fiber data.

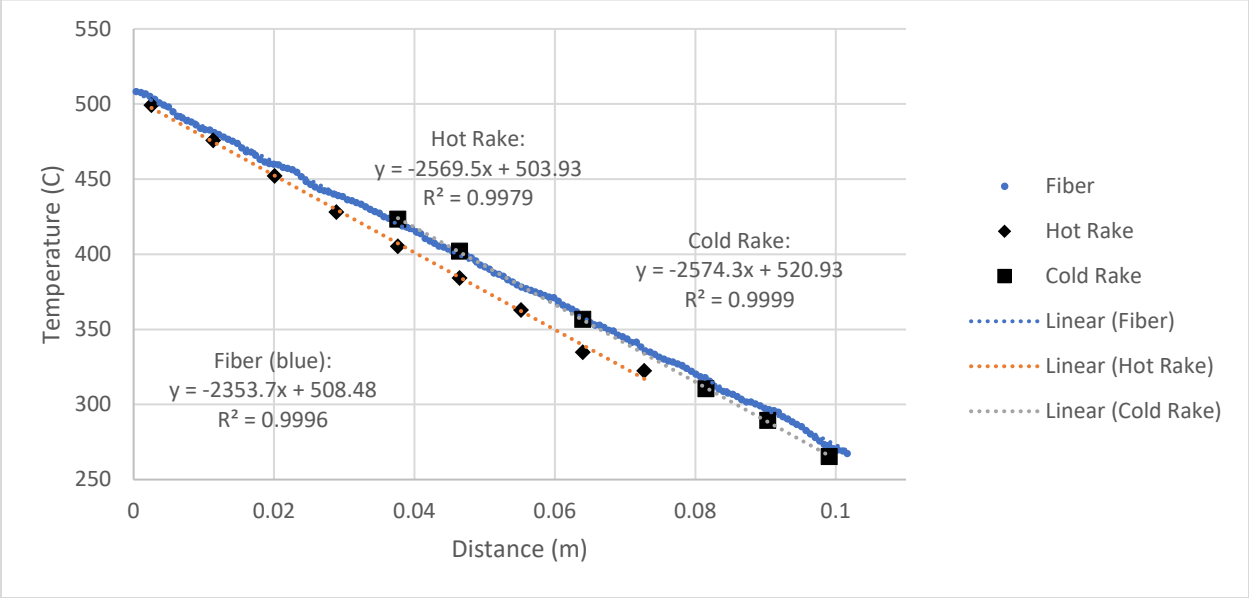

Figure 20 - Primary side comparison of fiber measurements to thermocouple rakes for Silica #530 at 200 [W]. Linear fit to each dataset also shown.

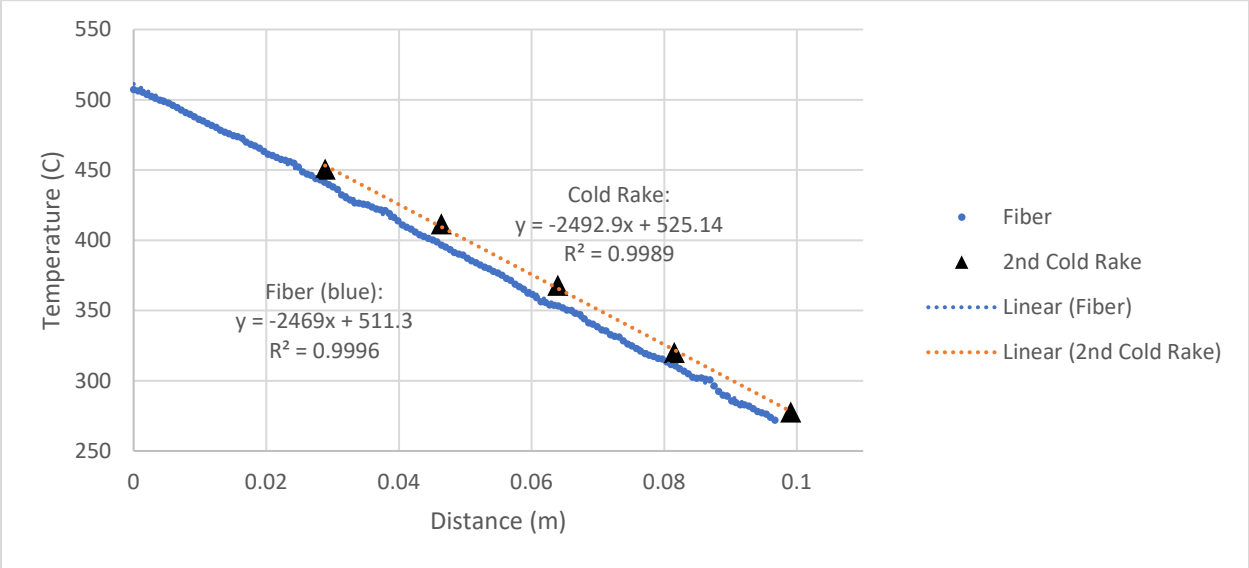

Figure 21 - Secondary side comparison of fiber measurements to thermocouple rake for Silica #530 at 200 [W]. Linear fit to each dataset also shown.

Figure 21 shows the entire static testing facility (while in operation) from three different views:

Figure 22 - Static testing facility from the front (top), side (bottom-left), and back (bottom-right)

The finalized methodology for running and recording data for the static testing proceeds as follows. Personal Protection Equipment (PPE) required for filling include long sleeved clothing, nitrile gloves, a disposable respirator mask, and safety glasses. PPE required for emptying include those items required for filling as well as welding gloves and a face shield. Possible hazards to be aware of include inhalation of particulate dust associated with Silicosis, skin irritation from the insulation and particles, electrical shock from the current source, and high temperature.

1. Put on nitrile gloves, disposable respirator mask, and safety glasses. Make sure to wear long sleeves, pants, and closed toed shoes.
2. Ensure that temperature sensors, current source, recirculating chiller, and other equipment are functioning properly. Check for any other obvious issues with the rig. Unplug both the chiller and the current source from the wall before continuing
3. Disconnect the heater wires from the current source and remove the top two pieces of Microtherm and mica sheet from the rig if they have not been already.
4. Place the 10.2 cm internal supports inside the specimen gaps and adjust the heater and coolers to ensure that both specimen gaps are approximately 10.2 cm. Tighten the threaded wingnuts on the support structure.
5. Position the thermocouple leads in their approximate location (i.e., 1.3 cm below the rake). Record a fiber tare at this point if using.
6. Fill both gaps with particle specimen until the particle level is just below the thermocouples. Remove the 10.2 cm internal supports.

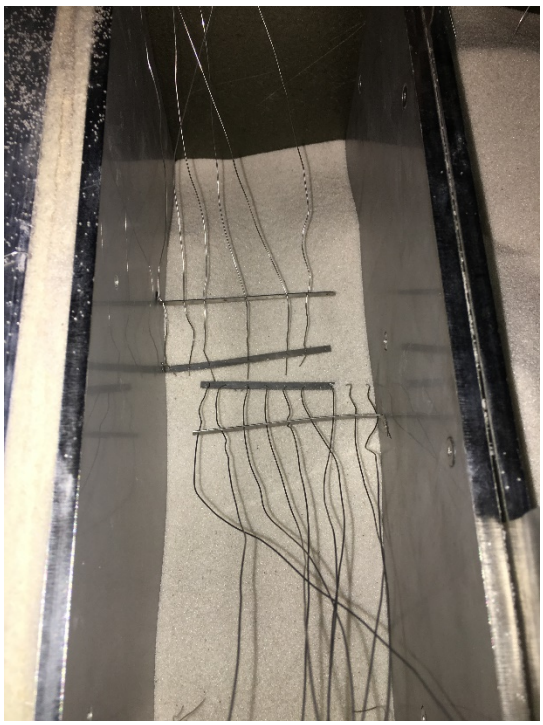

Figure 23 - Partial fill of one gap of the static sand rig.

7. Make a final check that the thermocouples are in the correct position. Fill slowly and evenly past the thermocouples.
8. Continue to fill the specimen gaps until the particle level reaches the top of the cooling assemblies and heater. Smooth the top layer of particles so that it is flat.

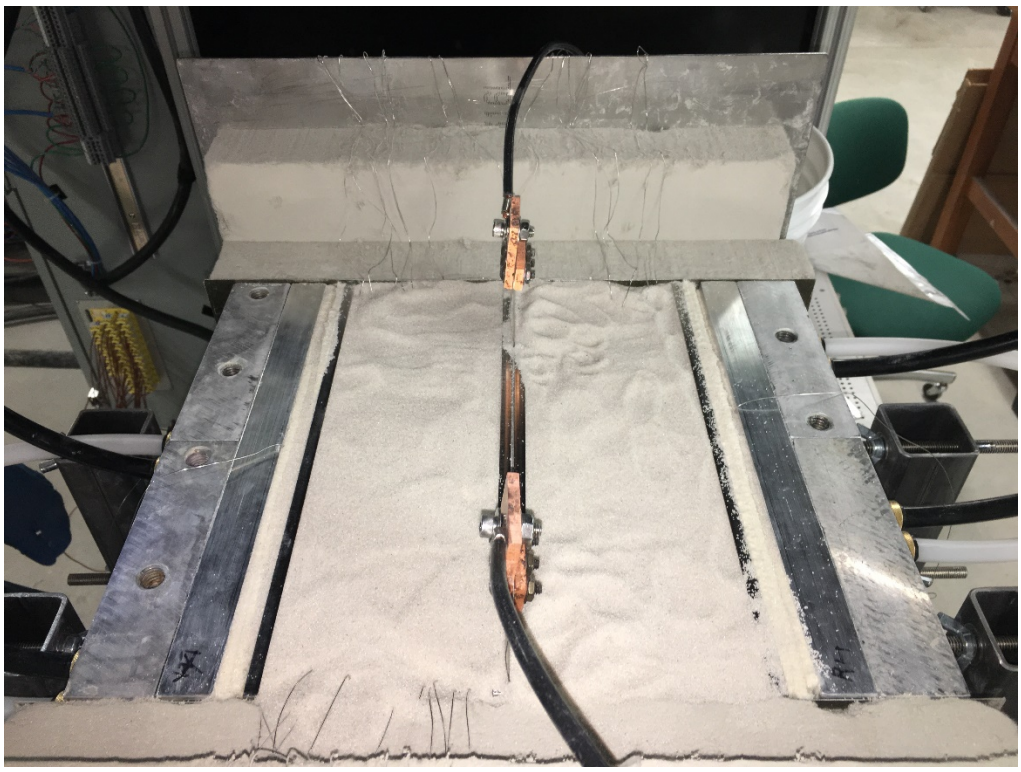

Figure 24 - Fully filled static sand rig.

9. Place the Mica top sheet followed by the first top layer of Microtherm being very careful not to damage the fragile Microtherm. Stuff white Kaowool insulation between the gaps of the Microtherm and serpentine heater.
10. Place the second layer of Microtherm on top of the first, again being careful of the fragile Microtherm. Stuff the gaps between the Microtherm and serpentine heater with the two small Microtherm blocks as well as the Kaowool insulation.

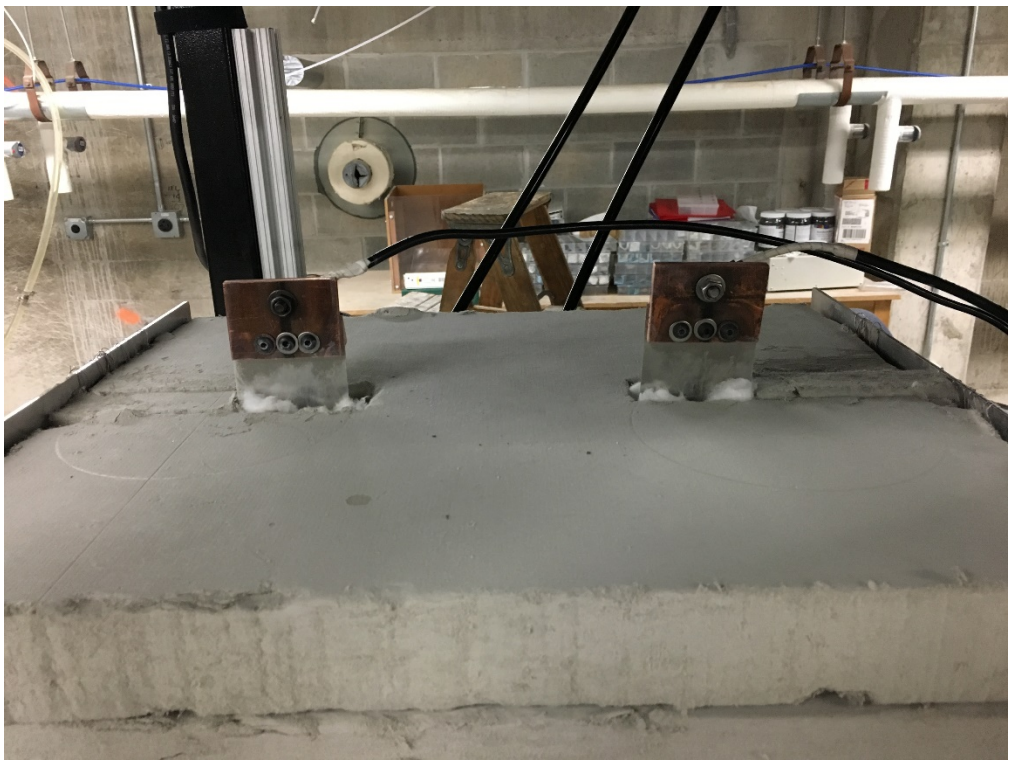

Figure 25 - Static sand rig with the top pieces of Microtherm in place as well as Kaowool and excess Microtherm stuffed in the gaps near the leads.

11. Reconnect the heater wires to the current source.
12. Begin the LabVIEW program to collect baseline data. A rate of 15 seconds per temperature recording is suggested. Make sure that data is recording properly and that the temperature readings are reasonable.
13. Plug in and turn on the recirculating chiller. Make sure refrigerant is pumping properly and that the chiller approaches the set temperature, generally 20°C.
14. Plug in and turn on the current source to the appropriate setpoint. A constant current is suggested. For reference, the serpentine heater is approximately 0.5 Ω in order to figure out the intended heat input.

a. With the current setup, it is suggested that the heater input does not surpass 500 W or 31.03 amps for materials of similar conductivity to these sands due to issues with the recirculating chiller removing heat.
b. If the power required is greater than the suggestion above, make special care to monitor the temperatures of the chillers as they will not be able to sustain 20°C.

15. Each heater input will require at least 40 hours to approach near steady state but more time may be necessary. During this time, monitor and record the voltage changes as displayed on the current source as well as using a voltmeter to read voltages on the serpentine heater just under the leads. Check the rig and temperatures at regular intervals for errors. Some errors include but are not limited to:
    a. Particles leaking from the rig
    b. Malfunction of the recirculating chiller
    c. Shorting of the serpentine heater (indicated by a significant and immediate decrease in voltage)
16. Steady state of the static rig is indicated by comparing the temperatures at TC2 and TC16 to an exponentially decaying fit for a temperature versus time plot of TC2 and TC16 for a later portion of the data

$$T = a0 - a1\ exp\left(\frac{-Time}{a2}\right) \quad (9)$$

where $a0$, $a1$, and $a2$ are constants

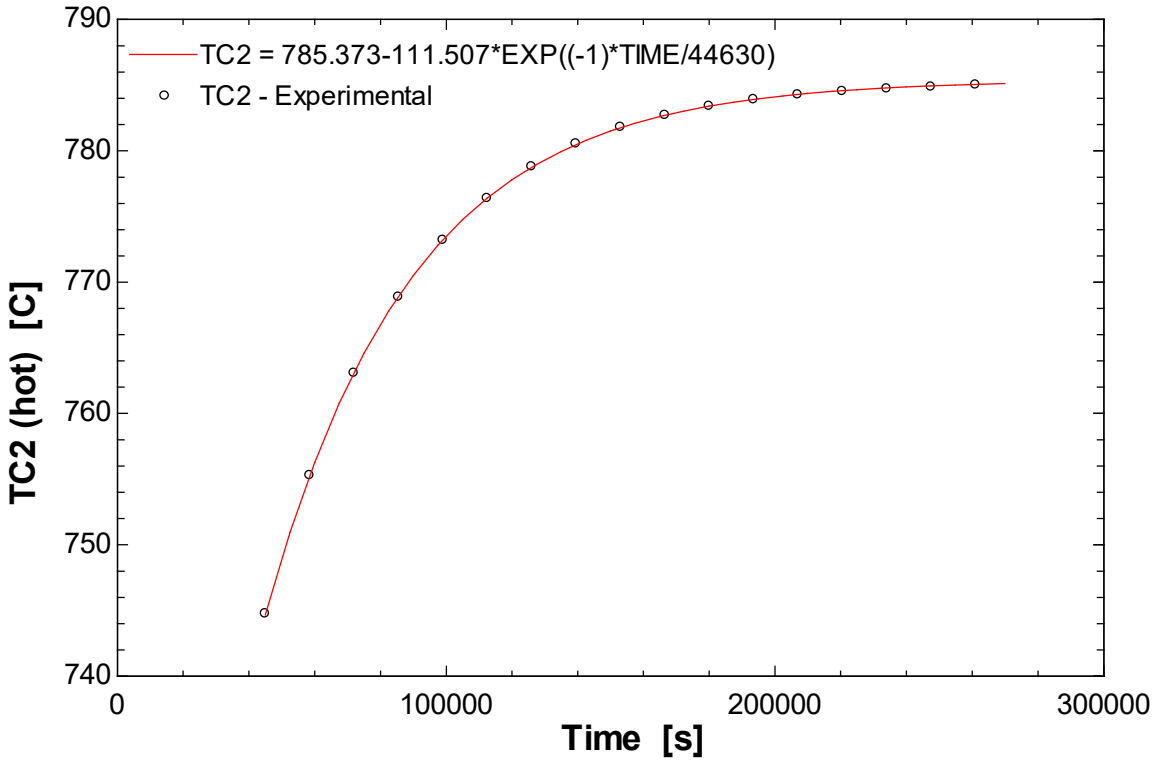

Figure 26 – Example of an overlay of exponentially decaying fit on top of experimental data. Only 1 in 900 points are shown for the experimental plot.

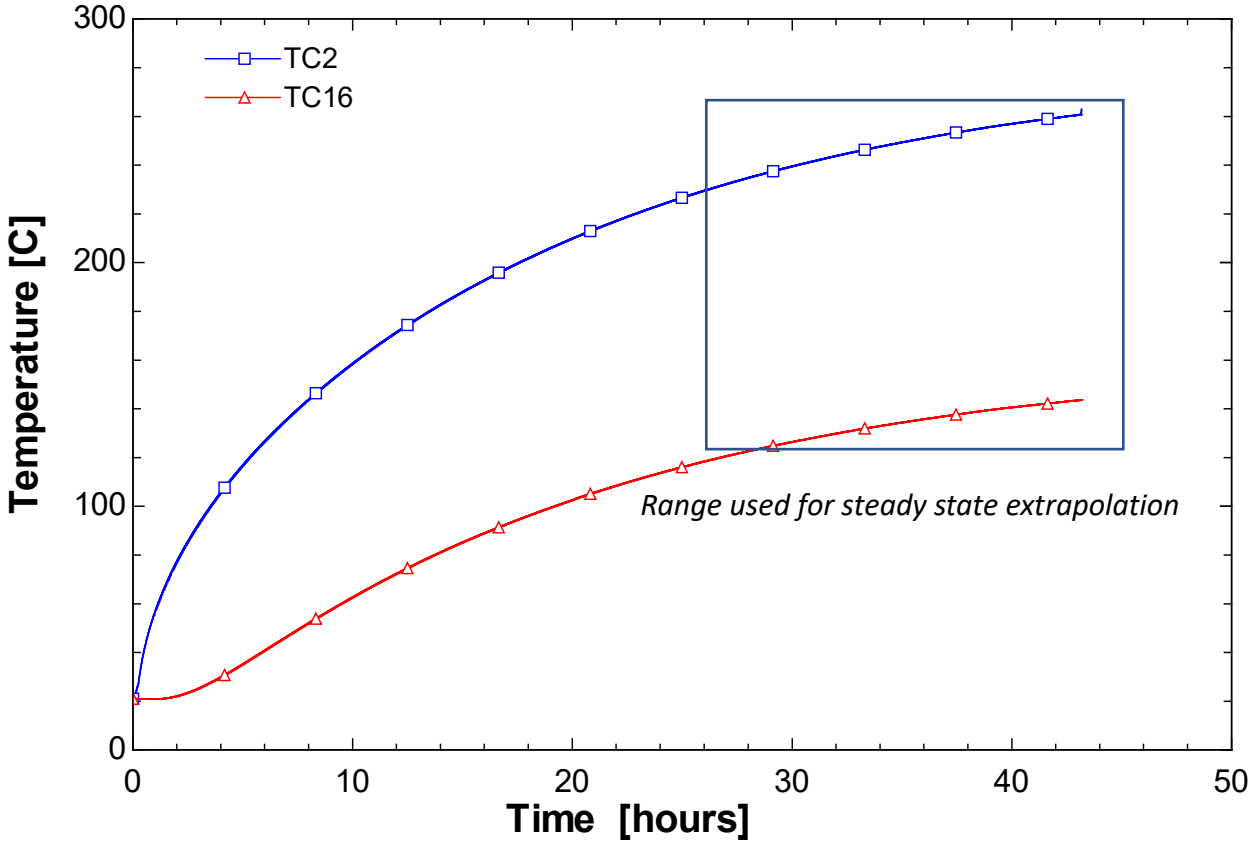

Figure 27 - Box indicates the portion of the data used for the exponentially decaying fit to estimate steady state temperatures at TC2 and TC16 in step 16. This data is from the heat up of Silica #460 at a heater input of 100 W.

17. Once steady state has been reached, stop data recording for that trial and repeat steps 12-16 for a new trial with an increased current input and a new file name for data collection in LabVIEW. Ensure the experimentally data is stored in a safe file location.
18. After the final current input trial has reached steady state, stop the LabVIEW program and move the experimental data to a safe file location.
19. Unplug and turn off the heater but continue to let the chillers run to cool the rig. Disconnect the heater wire from the current source.
20. Once the internal temperatures of the rig are cool enough, carefully remove the top two

pieces of Microtherm and mica sheet from the rig using welding gloves, a face shield, and all other PPE described in step 1. Continue to let the chiller run.

21. After the internal temperatures of the rig are near ambient, turn off and unplug the chiller.
22. Using the PPE described in step 1 along with an empty and clean shop vacuum, vacuum the particles from the inside of the rig. Insert the 10.2 cm internal supports once the particle level is low enough in the gap. Be careful not to bend significantly or break the thermocouple rakes, thermocouples, or capillary tubing.
23. Transfer the particles from the shop vacuum to another storage vessel.
24. Check the rig for damage, clean up, and remove all PPE.

Static Testing Analysis for Conductivity and Heat Capacitance

In order to estimate the thermal conductivity, a 1D analysis is carried out that utilizes Fourier's equation (Equation (1)) assuming a constant conductivity and temperature gradient related to the difference between TC2 and TC16. Locations of these thermocouples can be found in Figure 18. This estimate ignores edge effects and assumes completely 1-D heat transfer in the gap. The edge effects were later determined to be significant, and a higher-dimension model is required.

To account for edge effects, a 3-D FEA model was developed. SolidWorks was used to create the CAD model, and ANSYS was used to solve the steady state thermal models. The model is a half-rig, quarter-symmetry adiabatic model in that only one quarter of one side of the heater is modeled. Assumptions for the ANSYS models include:

- The heat input is uniformly bidirectional from the heater plate assembly (i.e., a 100 W heat input results in 50 W going into the main sand gap and 50 W going into the secondary sand gap).
- The heat flux input is uniform along the entire cross-section of the heater plate.
- The entire outer cross-section of the cold plate assembly is isothermal at 20°C.
- There is a small amount of free convection (estimated to be 10 $\frac{\mathrm{W}}{\mathrm{m^2-K}}$) to ambient (20°C) at the external portions of the rig [22].
- The particles, Microtherm insulation, and steel parts are isotropic in regard to thermal properties; the mica sheet is the only anisotropic material because of its variation in thermal conductivity. All temperature-dependent thermophysical properties are

implemented for known materials (i.e., everything except the particles and Pyrogel).

- There is no thermal expansion (i.e., the geometry is constant).

The #2-56 screws going through the Pyrogel are included along with the capillary housing the fiber extending across the entire rig in order to understand the impact of these penetrations. The thermocouple rakes and thermocouple sheaths are not included in the ANSYS model.

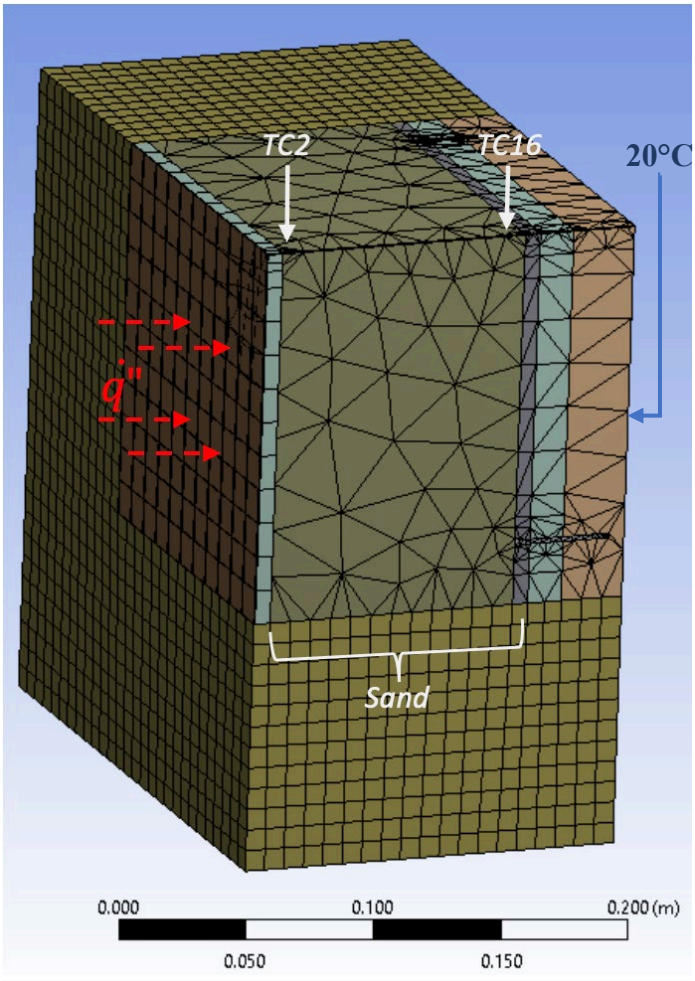

Figure 28 - 3D ANSYS quarter-symmetry model of one gap used for steady state and transient analysis

The basic premise of the 3D steady state analysis is that conductivity of the particles and Pyrogel are altered until the predicted temperatures at the locations of TC2 and TC16

matches the experimental results. The Pyrogel is not considered to have a known conductivity because there are three 5.1 cm sheets of Pyrogel compressed to create the Pyrogel gap. Not much was known about how compression of the Pyrogel and interfacing of the Pyrogel sheets affects the overall conductivity of the Pyrogel gap. The procedure for the steady state analysis of the thermal conductivity of the particles goes as follows:

1. For boundary conditions, determine and input:
    a. The appropriate input heat flux taken (from the input current and voltage taken with a multimeter across the leads)
    b. The cold face isothermal temperature which is usually given by TC28
2. Use the steady state, exponentially decaying projections as described by Equation (9) to determine the measured steady state temperatures for TC2 and TC16 with the curve fitting function in EES
3. Adjust the thermal conductivities of the sand and Pyrogel and run the steady state simulation until the temperatures match at TC2 and TC16 within 0.5°C of those determined in step 2
    a. The Pyrogel's conductivity should first be adjusted first to nearly match TC16, and the sand's conductivity should be adjusted next to match TC2 – this may have shifted the temperature at TC16
    b. If both temperatures do not match within tolerance after the previous step, continue to iteratively fine-tune the sand's and Pyrogel's conductivities
4. Record the conductivities of the Pyrogel and sand. The temperature associated with that conductivity is the average temperature across the gap

a. The temperature associated with the sand's conductivity for that trial would be the average temperature of TC2 and TC16
b. The temperature associated with the Pyrogel's conductivity for that trial would be the average temperature of TC16 and the isothermal cold plate

Initial comparisons of the 3D ANSYS model for determining conductivity compared to the 1D method using Fourier's Law show that there is an approximately 20% difference in conductivity between the two methods:

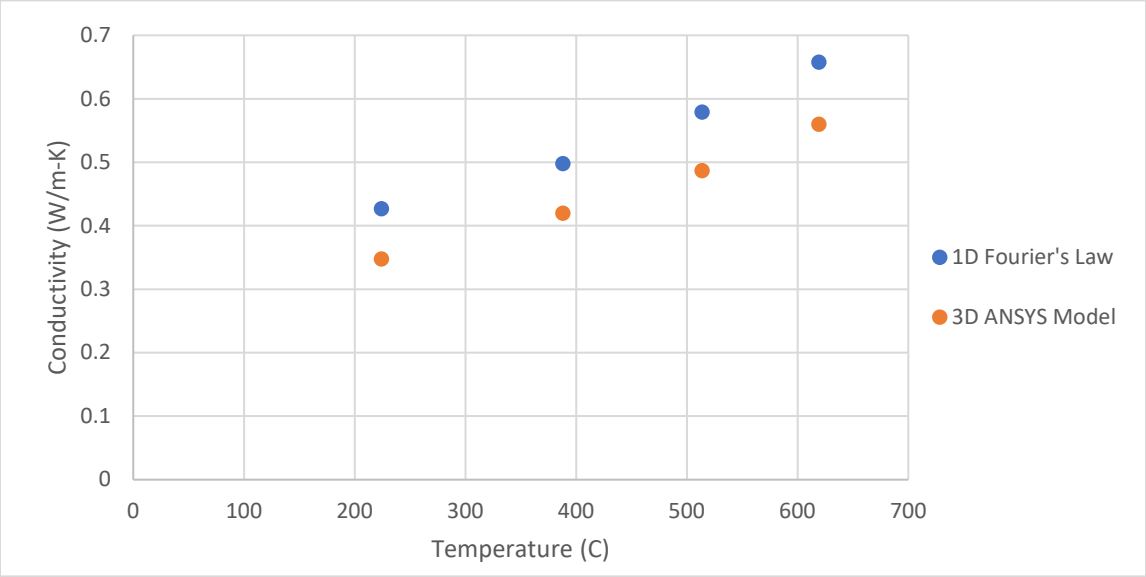

Figure 29 - Comparison of conductivities calculated using Equation (1) and the 3D ANSYS model for Silica #430. Temperatures used are the average temperature of the sand gap.

The conductivity calculated using the 3D model is less than the conductivity obtained by assuming 1D conduction because the heat loss causes less heat to flow through the centerline of the gap. As seen in Equation (1), the conductivity, k, will decrease if the heat input, $\dot{Q}$, decreases. More simply put, this heat loss can be characterized by:

$$\dot{Q}_{1D} = \dot{Q}_{3D} + \dot{Q}_{loss} \quad (10)$$

Ideally, a useful comparison to validate the model is to check the Pyrogel's thermal conductivities estimated by the 3D ANSYS model with the manufacturer's specs:

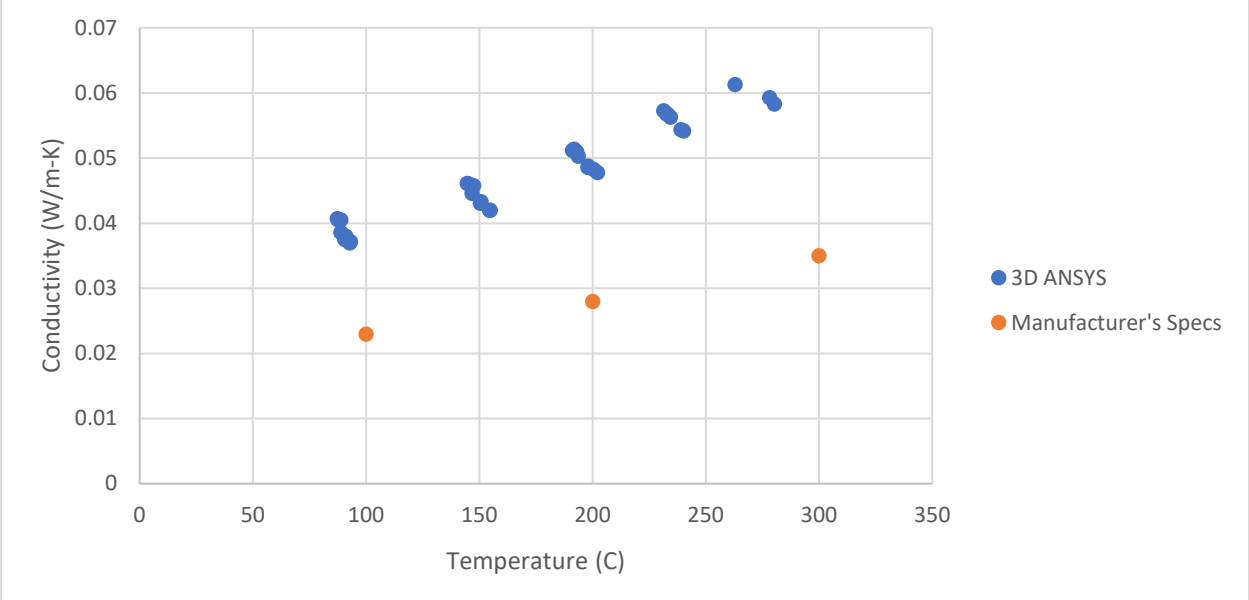

Figure 30 - Pyrogel conductivity comparison between those determined by the 3D model and those provided by Aspen Aerogel for Pyrogel XTF [23]

The effective conductivity of the Pyrogel estimated by the 3D ANSYS model is nearly double that provided by Aspen Aerogels [23]. This is likely related to the Pyrogel being compressed in the actual rig; the Pyrogel sheets are nominally 5.1 mm, and three of these 5.1 mm sheets are compressed to fit into a nominally 14 mm thick gap.

The bulk conductivities of the Silica sands are greater than that of the Alumino-Silicates, as shown:

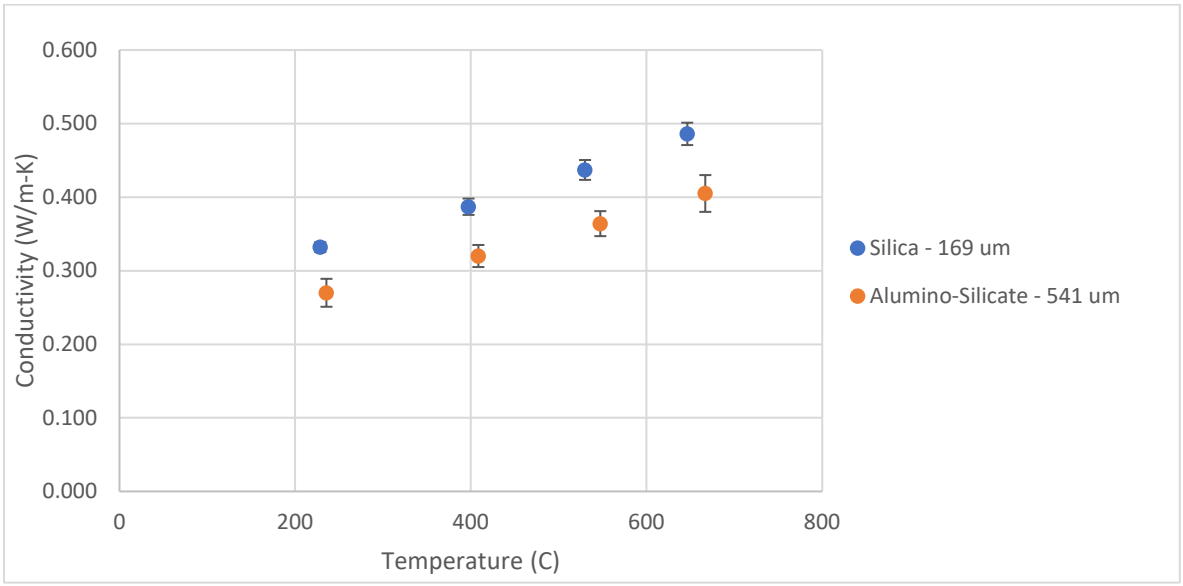

Figure 31 - Comparison of bulk thermal conductivities of Wedron Silica #510 (the smallest size distribution of the Silicas) to Christy Minerals STKO MCFC 60S Alumino-Silicate (the largest size distribution of the Alumino-Silicates)

The thermal conductivity for pure Quartz is an order of magnitude greater than the particles [24], and the thermal conductivity of Aluminum Oxide is approximately two orders of magnitude greater than the particles [25]. The Wedron Silica sands are composed of nearly entirely pure SiO_2 particles while the Christy Minerals STKO Alumino-Silicate sands are composed of a combination of mainly SiO_2 and Al_2O_3 sands. The data sheets for the Silica and Alumino-Silicate sands as well as the experimentally determined values for bulk conductivity for all of the sands can be found in the appendix. This methodology produces similar results for thermal conductivity for Silica sands #410, #430, and #480 compared to a recent project using a hot wire method by Chen et al at UC-San Diego [26].

The uncertainty for the conductivity measurements is determined by comparison of the temperature gradients along the thermocouple rakes and, if available, the fiber. For each

datapoint, the absolute uncertainty for conductivity (u_k) is determined based upon the standard deviation ($\sigma_{dT/dx}$) and average ($\frac{\overline{dT}}{dx}$)of the temperature gradients:

$$u_k = \frac{\sigma_{dT/dx}}{\frac{\overline{dT}}{dx}} \quad (11)$$

The uncertainty in conductivity averages to 4% and maximums and minimums at 2% and 8% respectively. There is no noticeable trend in the conductivity uncertainty in relation to heater input or type of sand used.

One interesting result from testing the different sized particles is that as the average particle size decreases, the bulk conductivity of the particles also decreases as seen in Figure 32. This occurs for both the Silica and Alumino-Silicate sands. One possible reason is because as the particle size decreases, there are more points of contact between the particles in a given volume of bulk medium. These points of contact add more interface resistance between the particles within the bulk medium resulting in an ultimately lower bulk thermal conductivity. Another possible explanation is that radiation cannot travel as far in the smaller gaps associated with the smaller particles, meaning particles are only seeing similar temperature particles nearby. It is not within the scope of this work to differentiate between these two effects. As a note, the packing fraction stayed relatively similar across all particle specimens tested.

$$\varphi = \frac{V_{particle}}{V_{bulk}} = \frac{\rho_{bulk}}{\rho_{particle}} \quad (12)$$

where φ is the packing fraction of the bulk medium; $V_{particle}$ is the volume that all of the particles take up; V_{bulk} is the volume that the bulk media takes up (e.g. particles and voids);

ρ_{bulk} is the density of the bulk media (e.g. particles and voids); and $\rho_{particle}$ is the density of the particle material.

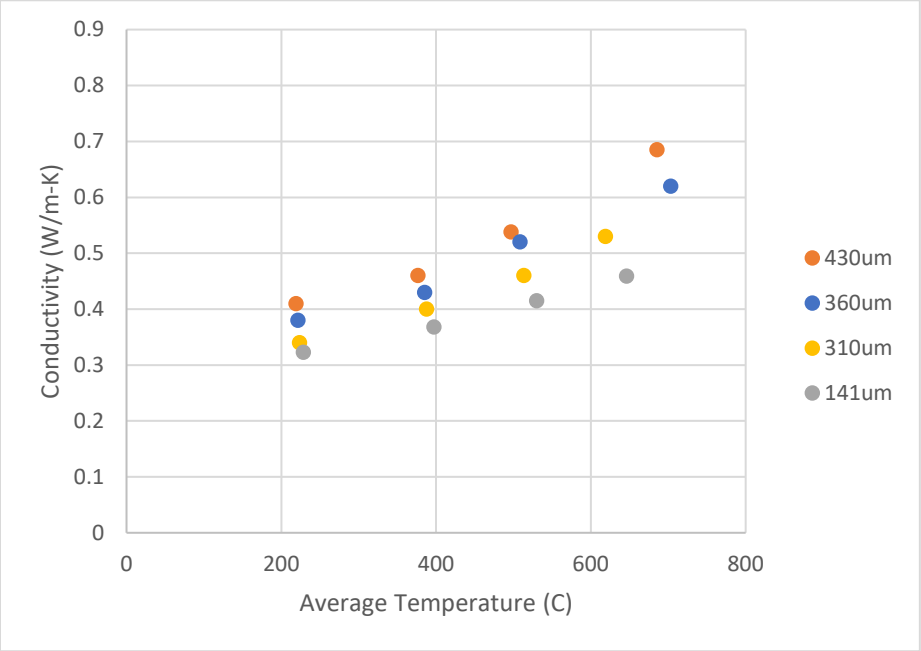

Figure 32 - Thermal conductivity of various particle sizes of the Silica sands. Note that as the average particle size decreases, the bulk thermal conductivity also decreases. Silica sizes 430um, 360um, 310um, and 170um are associated with Wedron Silica #480, #460, #430, and #510 respectively.

The effective thermal conductivities for bulk Silica sand of a particular particle size are calculated using the Zehner, Bauer, and Schlünder [27], [28] or van Antwerpen [29] models. Both slightly underestimate the results of the ANSYS method for Silica #410 as seen in Figure 33 and Figure 34. The two models consider various physical and thermal properties of the particles and interstitial gas (i.e., air) as well as radiation. The thermal conductivities of the base particle material (i.e., Quartz Silica) and interstitial gas are functions of temperature. Pure Silica sands can only be analyzed by the models because the Alumnio-Silicates are composed of multiple compounds.

Particle Properties	
Youngs Modulus	7.48E+10 Pa
Poisson Ratio	0.19
Molar Mass	60.08 g/mol
Emissivity	0.8
Interstitial Gas	air
Interstitial Gas Pressure	0.101325 MPa
Gas Molar Mass	28.96
Bulk Void Fraction	0.37
Particle Diameter	300 µm
Force between Particles	0.000116 N
Contact Area Fraction	0.01

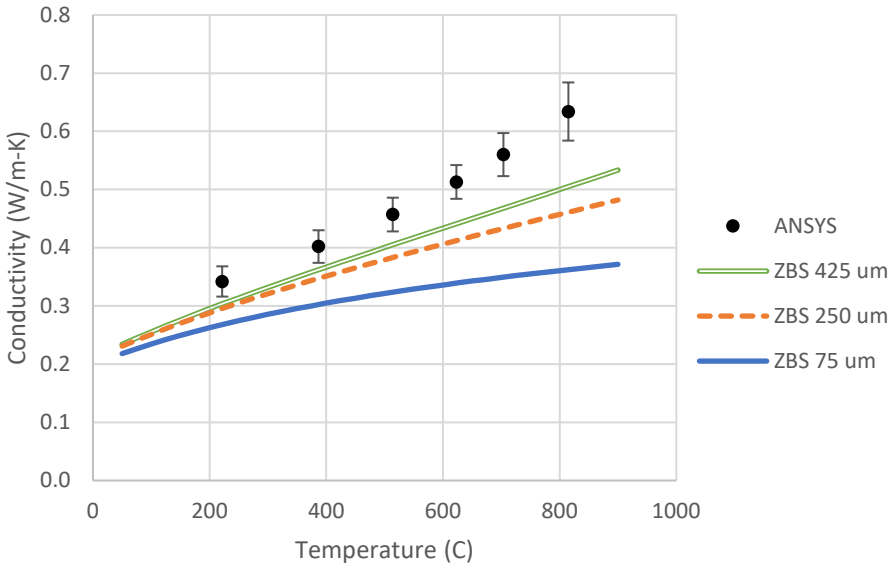

Figure 33 - Comparison of Silica 410 results from the ANSYS methodology with the Zehner, Bauer, and Schlünder [27], [28] model for various particle sizes encompassing the range of Silica 410. The input data for the model is shown on the left where the only parameter varied is the particle diameter

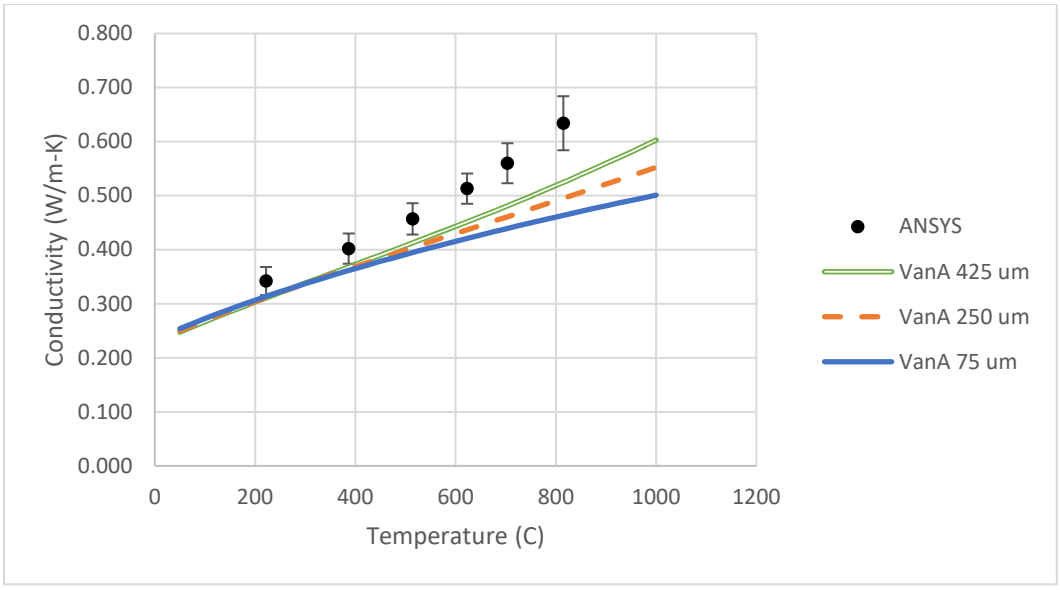

Figure 34 – van Antwerpen [29]model comparison with Silica #410. Same parameters are used as in Figure 33

In order to estimate the heat capacity of the particles, the temperature at either TC2 or TC16 of the experimental results at different times (usually 10, 20, and 40 hours) is matched

with the transient model ran for the same simulation time by adjusting the heat capacity in the model. The bulk density of the sand needs to be inputted into the model too which is approximately 1625 $\frac{\text{kg}}{\text{m}^3}$ for the Silica sands shown; measurements for the bulk density were taken at room temperature by simply dividing the mass of the sand by the volume. This process results in six total heat capacity values determined for a given sand for a given heat input: three heat capacitances at 10, 20, and 40 hours for either TC2 or TC16 as seen in Figure 35.

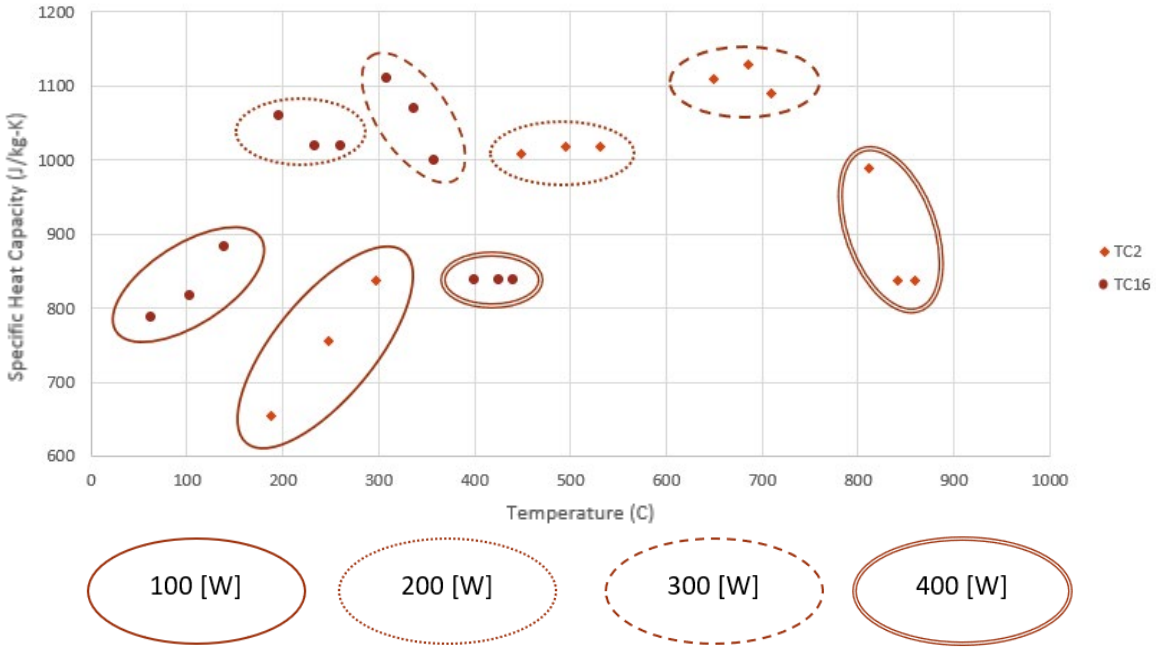

Figure 35 - Example of unaveraged specific heat capacitances determined by adjusting the specific heat capacitance of the sand to match either TC2 or TC16 of the 3D ANSYS model to the experimental at 10, 20, and 40 hours for various heater inputs. Within a given oval, the leftmost datapoint (i.e., the coldest) corresponds with 10 hours, and the rightmost datapoint (i.e., the hottest) corresponds with 40 hours.

Increasing or decreasing the heat capacitance of the Pyrogel by an order of magnitude has minimal effect on the temperatures of the transient simulation, as shown in Figure 36. The temperature dependent conductivities for the sand and Pyrogel found from the steady state 3D ANSYS analysis are used in the model.

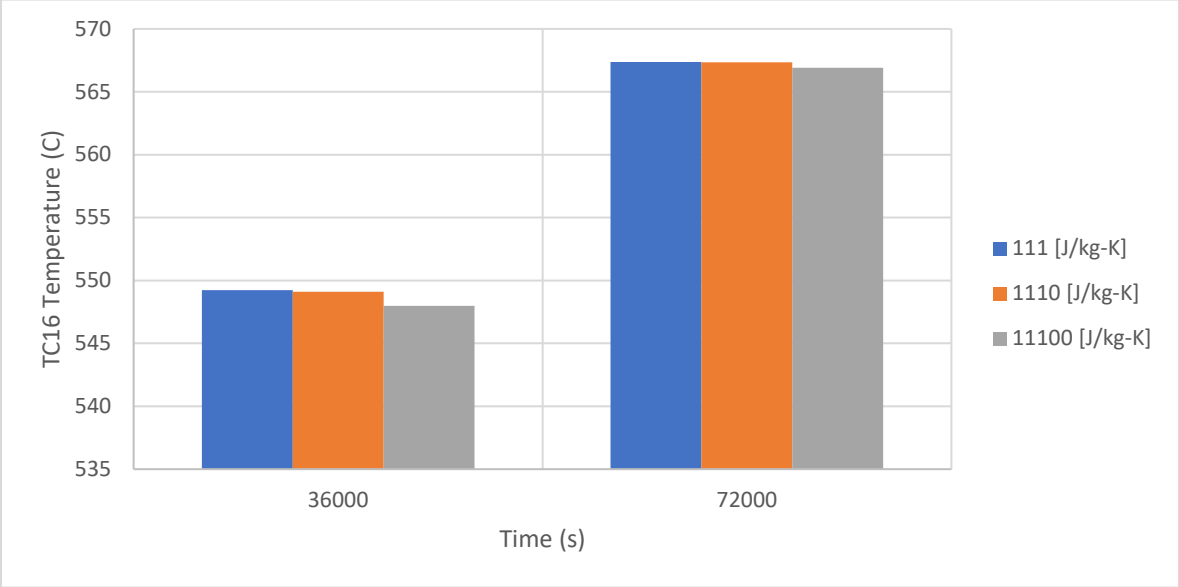

Figure 36 - Varying Pyrogel's heat capacitance in the 3D ANSYS model using the transient 600 [W] Silica #410 conditions at either 10 or 20 hours; the temperatures shown are from TC16. Note that temperatures change minimally despite the specific heat capacitance of the Pyrogel changing by an order of magnitude in each direction.

The methodology for the transient ANSYS analysis proceeded as follows:

1. Input the temperature dependent conductivity for the particles
    a. The Pyrogel's temperature dependent conductivity is determined from the steady state analysis, and the temperature dependent specific heat capacitances is provided by Aspen Aerogel [23]
    b. All of the other materials in the ANSYS model should have temperature dependent properties
2. Input the conditions from the previous trial into the steady state thermal analysis and run the steady state analysis; the final temperature distribution from the previous steady state trial will be used as initial conditions for this transient trial

   a. For example, if a 300 W heater input trial is being analyzed, the initial conditions will be the steady state temperature distribution from the previous 200 W heater input
   b. If the trial in question is the first trial, the initial temperature distribution for the rig should be uniformly ambient at 22°C
3. Choose a simulation time (i.e., 10, 20, or 40 hours) and thermocouple (i.e., TC2 or TC16) to match temperatures with the experimental. Run the transient analysis, adjusting the specific heat capacitance of the particles between each run, until the model temperature at that thermocouple matches the experimental within 0.5°C
4. Repeat step 3 for all simulation times and thermocouples. If three simulation times and both TC2 and TC16 are used for a given heater input transient trial (as shown in Figure 35), there should be six total specific heat capacitances determined for that trial
5. To determine a single-value specific heat capacitance for a given trial, the following averaging method should be used:
   a. For each thermocouple, average the specific heat capacitances of the sand ($c_{p,t,TC}$) for all the times (i.e., N = 3 for 10, 20, and 40 hours) to get an average specific heat capacitance for a thermocouple ($c_{p,avg,TC}$)

$$c_{p,avg,TC} = \frac{1}{N}\sum_{t=1}^{N} c_{p,t,TC} \qquad (13)$$

   b. Average all of the specific heat capacitances between thermocouples ($c_{p,avg,TC}$) determined in step 5a to get a final average specific heat capacitance ($c_{p,avg,final}$)

$$c_{p,avg,final} = \frac{c_{p,avg,TC2} + c_{p,avg,TC16}}{2} \quad (14)$$

6. To determine a single-value temperature for a given trial's averaged heat capacitance as determined in step 5, the following averaging method should be used for temperature:
    a. For each simulation time and thermocouple (i.e., one of the six datapoints from the trial), average the final temperature ($T_{t,TC}$) with the initial temperature ($T_{o,TC}$) to get an average temperature over a simulation time for a thermocouple ($T_{avg,t,TC}$):

$$T_{avg,t,TC} = \frac{T_{t,TC} + T_{o,TC}}{2} \quad (15)$$

    b. For each thermocouple, average the temperature determined in step 6a ($T_{avg,t,TC}$) for all the times (i.e., N = 3 for 10, 20, and 40 hours) to get an average temperature for a thermocouple ($T_{avg,TC}$):

$$T_{avg,TC} = \frac{1}{N} * \sum_{t=1}^{N} T_{avg,t,TC} \quad (16)$$

    c. Average all of the temperatures between thermocouples determined in step 6b ($T_{avg,TC}$) to get a final average temperature ($T_{avg,final}$)

$$T_{avg,final} = \frac{T_{avg,TC2} + T_{avg,TC16}}{2} \quad (17)$$

7. Repeat steps 2-6 for all heat input trials. There should be single-value specific heat capacitances associated with single temperatures as shown in Figure 37

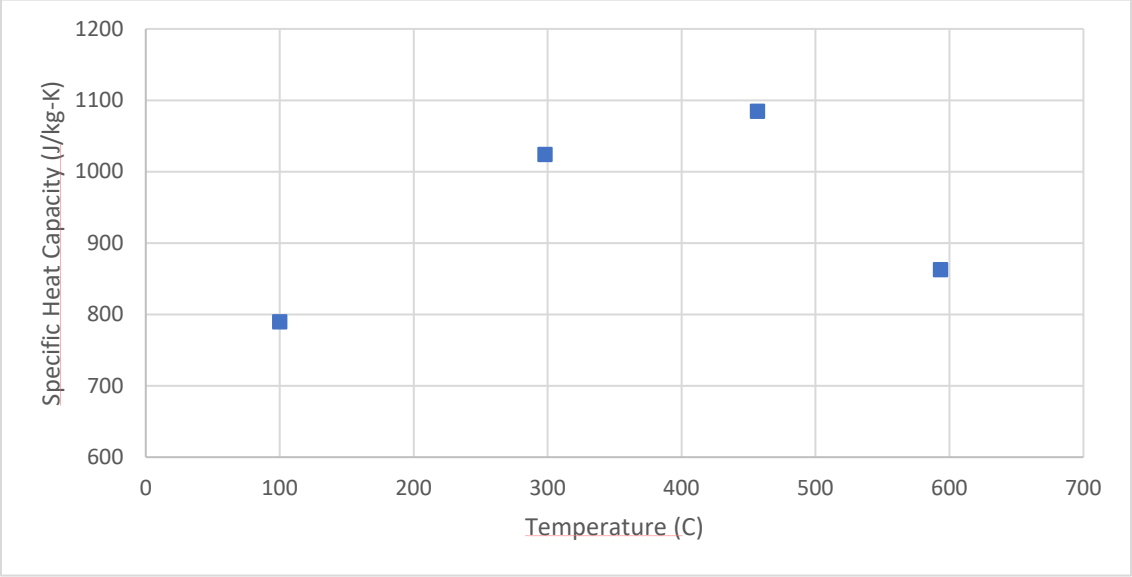

Figure 37 - Final averaged specific heat capacitance versus averaged temperature for Silica #410. The initial plot of specific heat capacitances as a function of temperature, simulation time, and thermocouple location before averaging can be seen in Figure 35

One notable trend that was apparent for most all of the sands is the reduction in specific heat capacitance just before 600°C. Upon further investigation into the bulk material of the particles, Quartz silica, using the NIST-JANAF tables [30], there is a phase change in crystalline structure of Quartz at 573°C. During a slow, reversible phase change such as occurred in the experiment, α-Quartz transitions to β-Quartz as shown in Figure 38 which results in a decrease in density and specific heat capacitance of the material [31]. The specific heat capacitances do not seem to be a function of particle size, as is with conductivity, which seems reasonable because the specific heat should only depend on the bulk material [32].

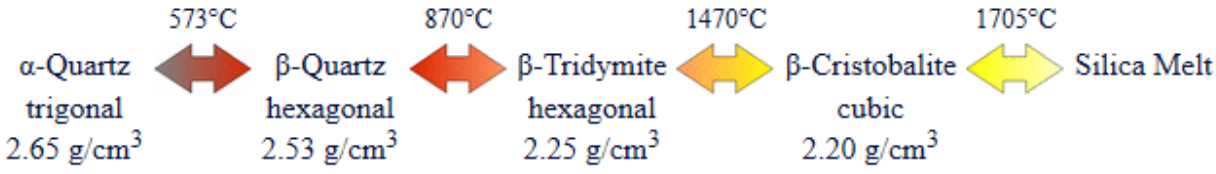

Figure 38 -- Reversible phase transitions for Silica Polymorphs. Image taken from [31]

To verify this phase transition, a PerkinElmer 8000 DSC (Differential Scanning Calorimeter) provided by the Soft Materials Characterization Lab at the University of Wisconsin-Madison was used.

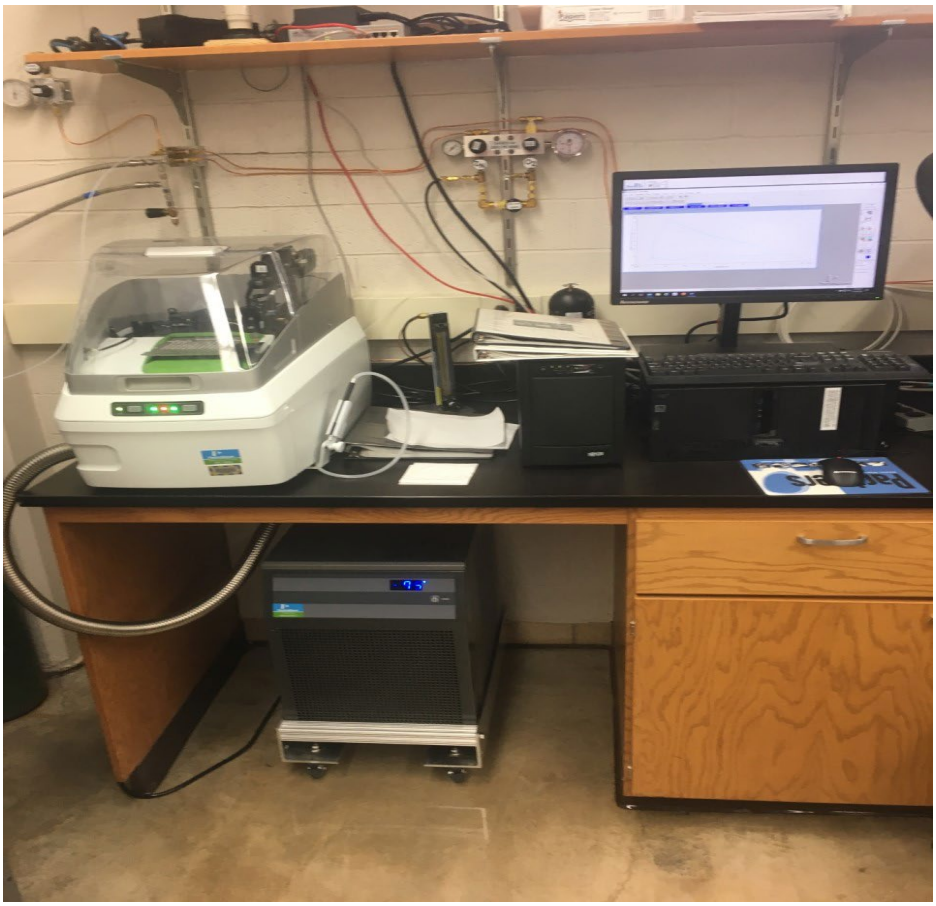

Figure 39 -- PerkinElmer 8000 DSC (top left), cooler (bottom left), and software display (top right) used.

The device uses a double furnace to compare heating a small cell loaded with a specimen to an empty cell. The specimen's weight is usually around 25-40 mg. Non-hermetic gold pans are required to be used as the loading cells in this case to allow the device to measure specific heat capacitance up to 700°C, the upper temperature limit of the DSC.

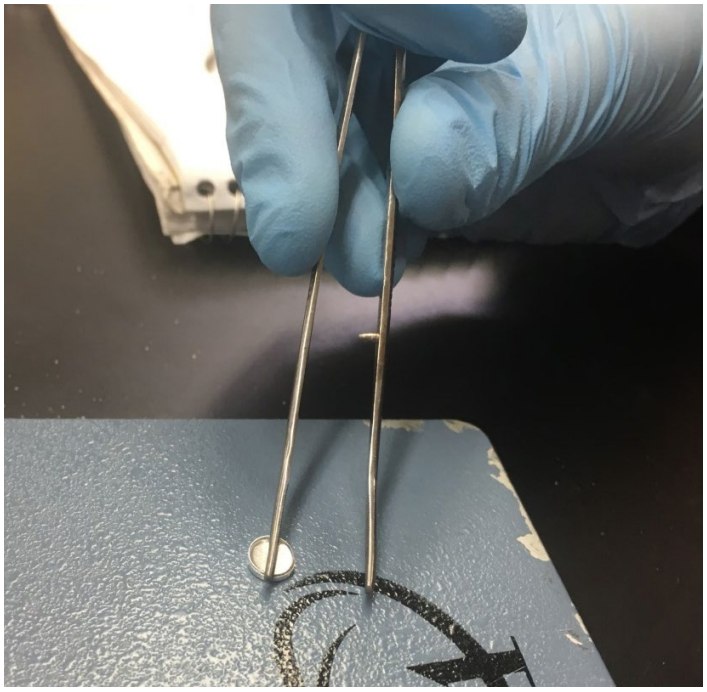

Figure 40 -- Tweezer placing top of pan on a loading cell to be used for the DSC. A crimper was used to actually seal the cell.

The testing method for the DSC involved two cycles of heating and cooling at a rate of 20°C/min between 20°C and 700°C and also holding at either 20°C or 700°C for three minutes when those temperatures were reached. Heat flow data for heating and cooling is collected from the second cycle as the second cycle is considered more reliable; this raw data for Silica #510 is shown in Figure 41.

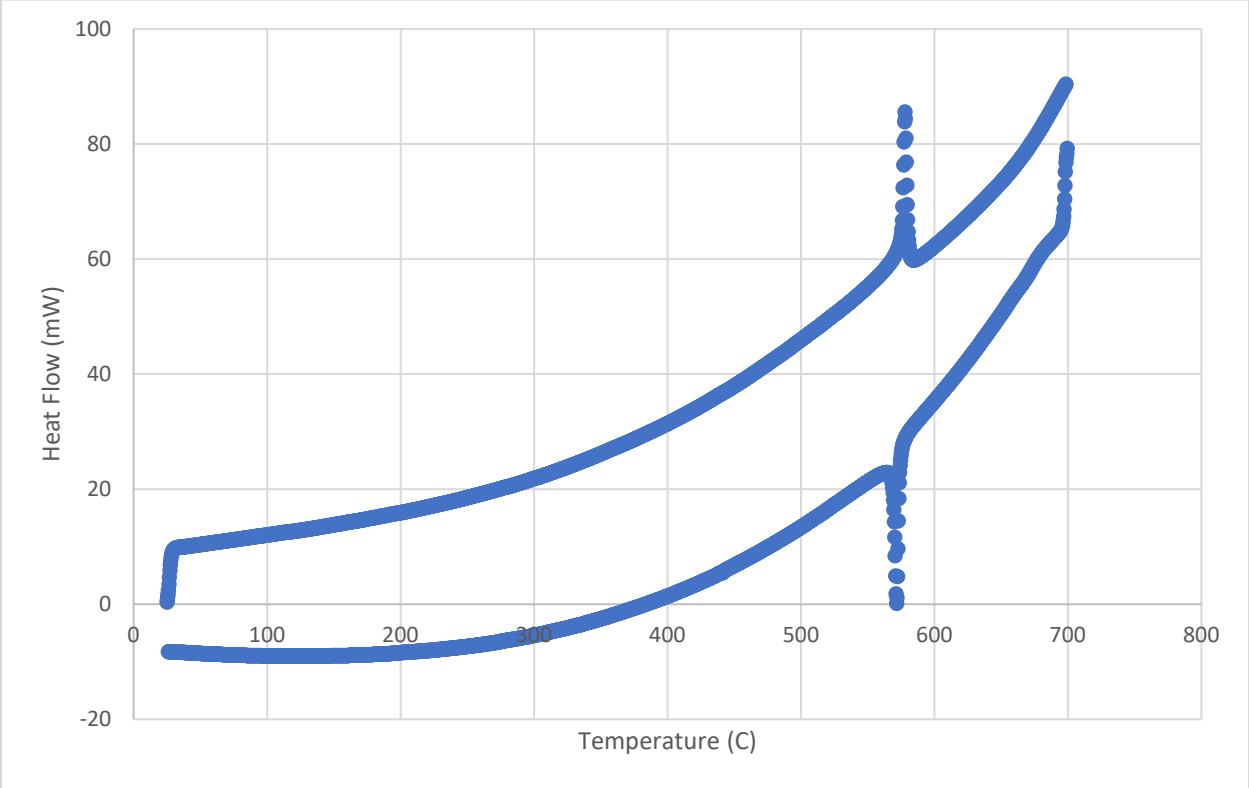

Figure 41 -- Raw DSC heat flow data from the heat up and cool down of the second cycle. The top curve is heating up the specimen while the bottom curve is cooling down the specimen.

The analysis method to determine specific heat capacitance from the DSC data was developed by Dustin Witkowski a postdoctoral research associate at the University of Wisconsin-Madison Engine Research Center [33]. Normally, two empty cells are placed in the DSC to determine a baseline for heat flow into the cell. This baseline heat flow is subtracted from the heat flow with the specimen included to determine the net heat flow solely into the specimen; the subtraction removes the heat flow into the gold pan itself. Dustin's method relies on the symmetry ($\dot{Q}_{b,symm}$) of the heating curve ($\dot{Q}_{s,heat}$) and cooling curve ($\dot{Q}_{s,cool}$) to determine a baseline as seen in Figure 41.

$$\dot{Q}_{b,symm} = \frac{\left(\dot{Q}_{s,heat} + \dot{Q}_{s,cool}\right)}{2} \quad (18)$$

The symmetry curve was then used to calculate the heat capacitance $c_{p,symm}$ based upon modification of Equation (2).

$$c_{p,symm} = \frac{\left(\dot{Q}_{s,heat} - \dot{Q}_{b,symm}\right)}{m_{sample}\left|\frac{dT}{dt}\right|} \quad (19)$$

where m_{sample} is the mass of the sample (between 25-40 mg as stated before) and $\frac{dT}{dt}$ is the rate of temperature change with respect to time (20°C/min). Dustin's method seems to be a suitable replacement for the normal methodology of two tests which would have required another set of expensive, gold loading cell pans. DSC tests at lower temperatures for the sands using aluminum loading cell pans with both methods gave similar results. Figure 42 shows an overlay of the DSC, 3D ANSYS transient model, and NIST-JANAF specific heat capacitances for a Silica sand, all of which are within 15% of each other.

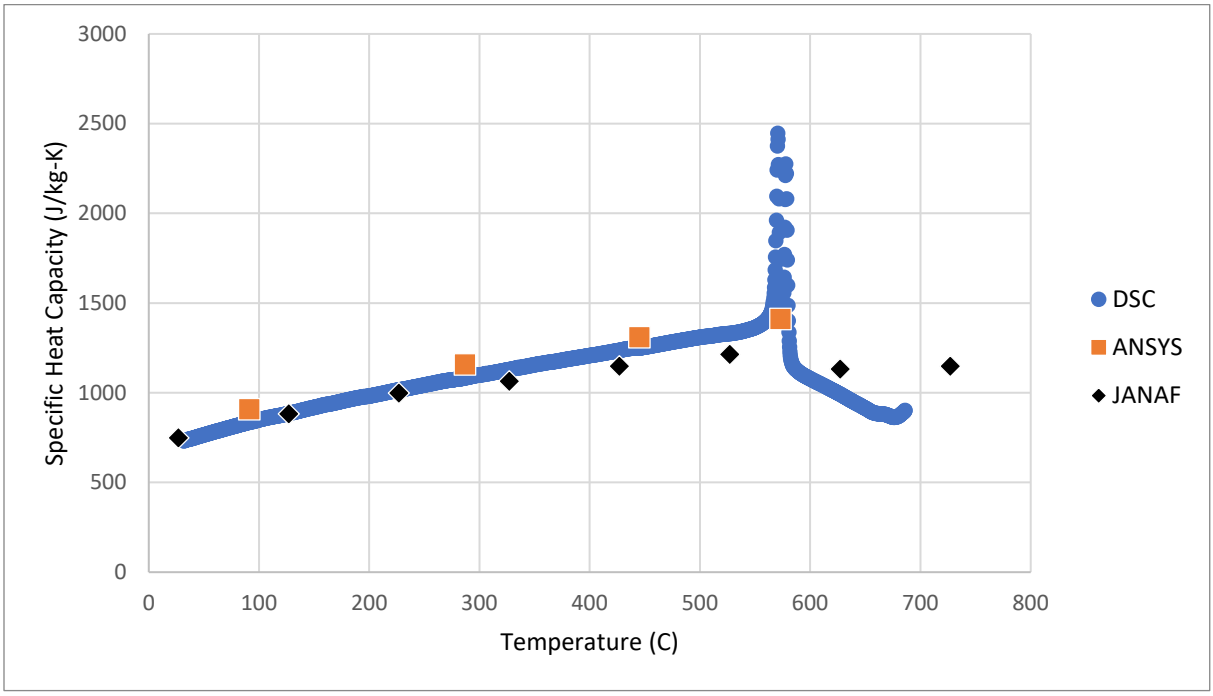

Figure 42 -- Specific heat capacity of Silica #510 from the DSC, the transient analysis of the static sand rig via ANSYS, and the NIST JANAF tables [30]. The spike in the DSC plot indicates where the change in crystalline structure of the Silica is occurring. A peak or dip in specific heat capacity for some of the sands which indicates the phase change can be seen in Figure 38

The specific heat capacity of the Alumino-Silicate sands could be estimated using the NIST-JANAF tables as:

$$c_p = \sum_{i=1}^{N_m} \frac{c_{p,i}\,\emptyset_i}{N_m} \qquad (20)$$

where N_m is the number of components in the sand; $c_{p,i}$ is the specific heat capacitance of a given component; and $\emptyset_i$ is the relative ratio of that component in the sand described by the mineralogy. Figure 42 shows an overlay of the DSC, 3D ANSYS transient model, and NIST-JANAF specific heat capacitances using (20) for an Alumino-Silicate sand, all of which are within 15% of each other. The DSC was not able to obtain as high of temperature compared to Figure 42 due to the lack of gold pans. Regardless, using the NIST-JANAF tables in

conjunction with Equation (20) seems to be a valid way to estimate specific heat capacitance of bulk material. The data sheets for the sands tested can be found in the appendix.

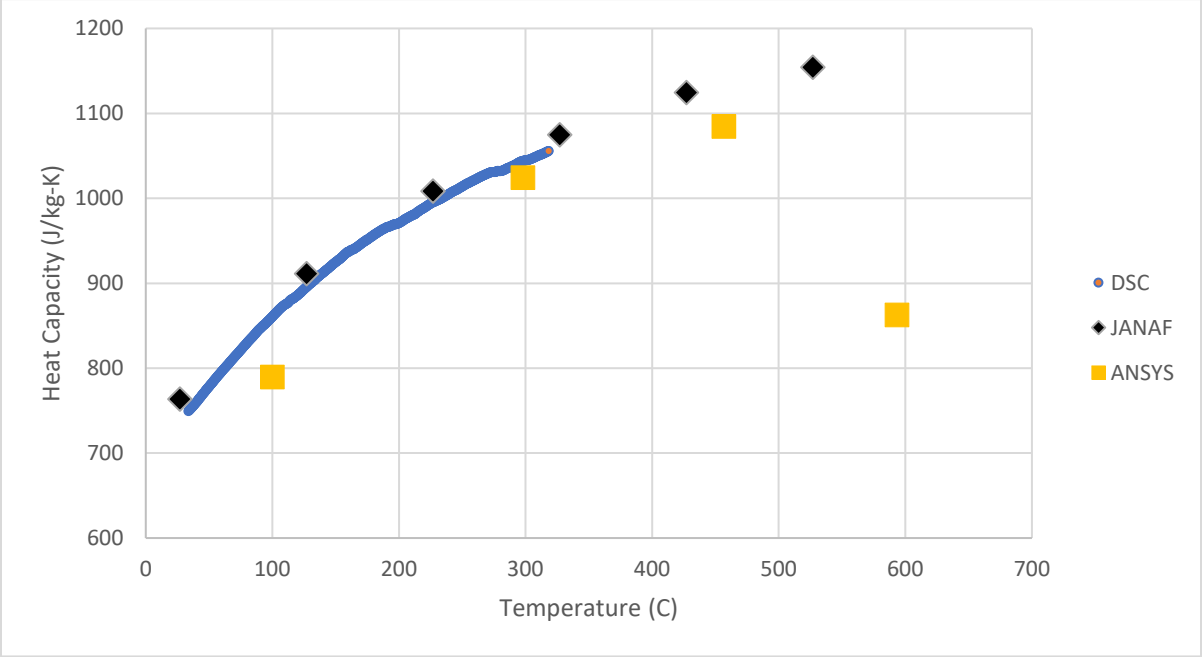

Figure 43 - Specific heat capacity of Alumino-Silicate MCFC 50S from the DSC, the transient analysis of the static sand rig via ANSYS, and the NIST JANAF tables [30] using Equation (20). The spike in the DSC plot indicates where the change in crystalline structure of the Silica is occurring. A peak or dip in specific heat capacity for some of the sands which indicates the phase change can be seen in Figure 38

Dynamic Rig Design for Heat Transfer Coefficients

The second experiment that was built is a dynamic test rig (meaning moving particles) to determine heat transfer coefficients between a packed bed flow of particles and a solid surface. The premise of the dynamic rig is that a heat flux is applied at one surface that is exposed to a moving, packed bed of particles as seen in Figure 44.

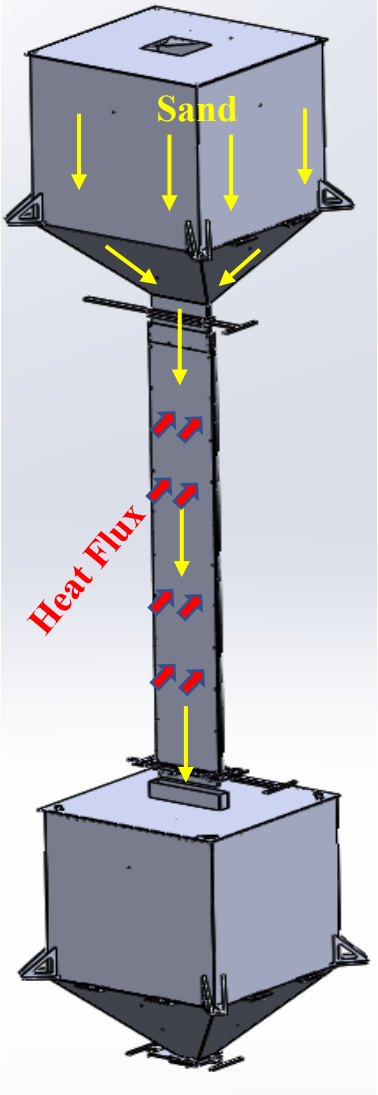

Figure 44 - Schematic of the dynamic test rig. Yellow, thin arrows indicate the direction of sand flow. Red, block arrows indicate the direction of applied heat flux.

The heat transfer coefficient (h) can be deduced using the following equation:

$$\dot{Q}" = h\,\Delta\mathrm{T} \qquad (21)$$

The temperature difference in Equation (21) is defined as:

$$\Delta\mathrm{T} = T_{wall} - T_{fluid} \qquad (22)$$

where T_{wall} is the wall temperature and T_{fluid} is the bulk temperature of the fluid.

Brayton Energy had initially indicated that the particle flow should correspond to a moving packed-bed flow of Wedron Silica #410 (for which the data sheet can be found in the appendix) within a high aspect ratio rectangular channel that had either a 3 mm or 6 mm gap. The flow velocity should be in the 15-20 mm/s range. A "moving packed-bed flow" is defined as closely packed particle flow, much like a laminar, plug flow. The test section was designed to accommodate higher flow rates, and the finalized nominal design parameters are a 3 mm gap with a 35 mm/s flow rate.

Brayton wanted the test section to be able to achieve high temperature flow, and our lab group had decided that 300°C is a reasonable goal due to estimated heat loss and structural safety constraints. The test section needed to be sufficiently tall with a long enough run duration to ensure that both a fully developed flow and thermal steady state are achieved. The dynamic rig was capable of measuring the convection coefficient (h) and the associated Nusselt number (Nu), which is defined as:

$$Nu = \frac{h\,L_{char}}{k} \qquad (23)$$

where L_{char} is the characteristic length, defined as the hydraulic diameter for internal flow,

and k is the thermal conductivity of the flowing media. These results will be used to help design components associated with the particle pathway for the Gen3 CSP project.

Based on the previous work in [16], the test section needs to be at least 1 meter in length to ensure fully developed flow. To double check this proposed length, the time for a thermal wave to diffuse through the sand gap needs to be much shorter than the time required for the sand to pass through the test section at the highest flow rates. The thermal diffusivity (α) of Silica #410 is estimated to be approximately $2\text{x}10^{-7}$ m^2/s using the equation:

$$\alpha = \frac{k}{\rho\, c_p} \tag{24}$$

The time for the thermal wave to diffuse through the sand gap (where *gap* = 3 mm) is found to be approximately 10 seconds:

$$\tau_{diffuse} = \frac{gap^2}{4\,\alpha} \tag{25}$$

The time for the sand flowing at a given velocity (v) to pass through the length of the test section (L) is calculated as:

$$\tau_{vel} = \frac{L}{v} \tag{26}$$

Setting $\tau_{diffuse}$ equal to τ_{vel} for the faster flow velocity of 70 mm/s, the length of the test section only needs to be approximately 0.75 m to achieve fully developed flow. To ensure a reasonable length of fully develop flow as well as to mitigate entrance and exit effects and the associated flow pattern issues that might occur at the inlet and outlet, the test section is made 1.5 m long. The width of the test section is 203 mm (i.e., the flow cross-section is nominally 3 mm x 203 mm) in order to reduce edge effects and attempt to replicate an infinitely wide test

section.

Determining the correct volume of Silica #410 to use is important in order to ensure that the rig is able to achieve thermal steady state for a given test, even those at the faster flow rates. Aside from less sand being easier to handle, minimizing the amount of sand used decreases the amount of heat loss because smaller supporting connections can be used for the supply bin. An estimated flow time of 2 hours, based on [16], seemed more than adequate to ensure that thermal steady state could be achieved. This amount of flow time required about 0.2 m^3 of Silica #410.

The facility housing this experiment is a silo, shown in Figure 45, located on the property of the University of Wisconsin-Madison's Tantalus facility in McFarland, WI. The non-air-conditioned silo contained an existing experiment and three-story structure that was gutted in order to make room for the dynamic rig test. Another important feature of the silo is that it contains a CM Valustar 2-ton, electric chain hoist that is four stories high. The hoist moves along the plane parallel to the ground on rollers on the I-beam support in one direction and via a shaft and manual pull-chain that allows the I-beam to move in the other direction, as seen in Figure 46. This chain hoist can lift and move the basin of particles above the test section.

Figure 45 - CAD model of silo with external structure, and three vertical panoramas of the interior of the silo containing the previous experiment.

Figure 46 - CM Valustar 2-ton chain hoist with rollers to move the hoist along the I-beam support into/out of the plane of the picture and a manually operated chain pull to move the I-beam allowing left/right movement of the hoist relative to the picture

The experiment is housed in the center opening in the support structure in order to limit the amount of square-tube cross-bracing that is needed to be cut and removed. 10.2 cm square tube (with 4.8 mm wall thickness) with 10.4 m length were installed in each of the corners of the center hole to act as stilts for the dynamic rig's support structure, as shown in Figure 47. Guard rails and kick guards were welded to the stilts to prevent falling hazards through the center hole. Because of the support configuration, the supply sand must be lifted from the ground level to above the third story deck with the chain hoist, moved over the center of the support structure, and lowered above the test section. Due to clearance between the hoist clevis and third deck, the container for the supply sand needs to be shorter than 2.1 m.

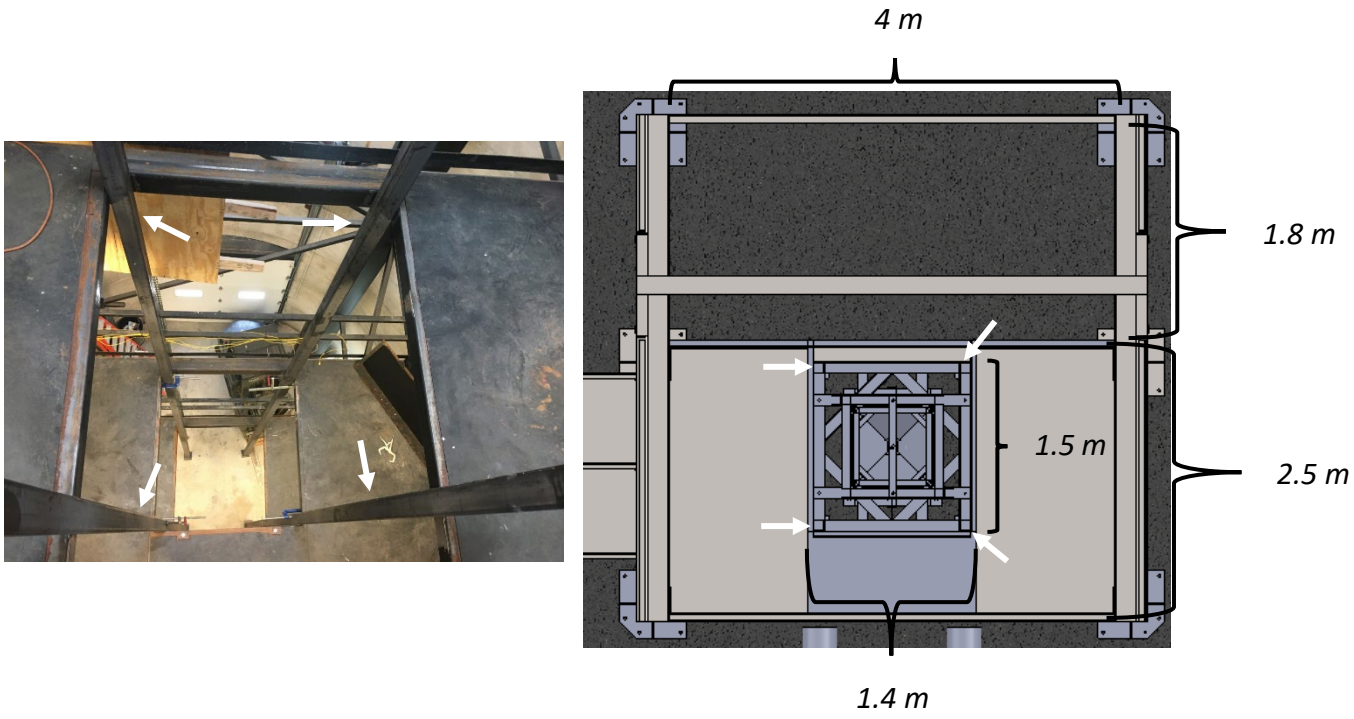

Figure 47 - Overhead view of external support structure (within silo) with dynamic rig in place showing crucial dimensions. Arrows indicate the 10.2 cm square tube stilts

The dynamic test rig was composed of three main components: the hopper, the test section, and the basin as shown in Figure 48. The particles are supplied to the test section by a hopper sitting above it. Within the test section, a heat flux is applied on one wall, and temperature measurements are obtained in order to determine the heat transfer coefficient. The basin catches the particles exiting from the test section and rests on top of a scale in order to measure the mass flow rate of the particle flow. After the hopper and test section have been completely emptied of particles, the basin can be moved out from under the test section and connected to the chain hoist. The basin is lifted above the third deck, lowered on top of the supply hopper, and emptied of the (now warmer) particles into the supply hopper for another run. The basin is then lifted via chain hoist and returned to ground level where it is placed underneath the test section for subsequent testing. One benefit of this testing methodology is that each recirculation and heating of particles will allow for subsequent higher temperature measurements. In practice this approach caused significant uncertainties for inlet temperature measurement due to temperature gradients that were present in the supplied sand as will be discussed in the next chapter.

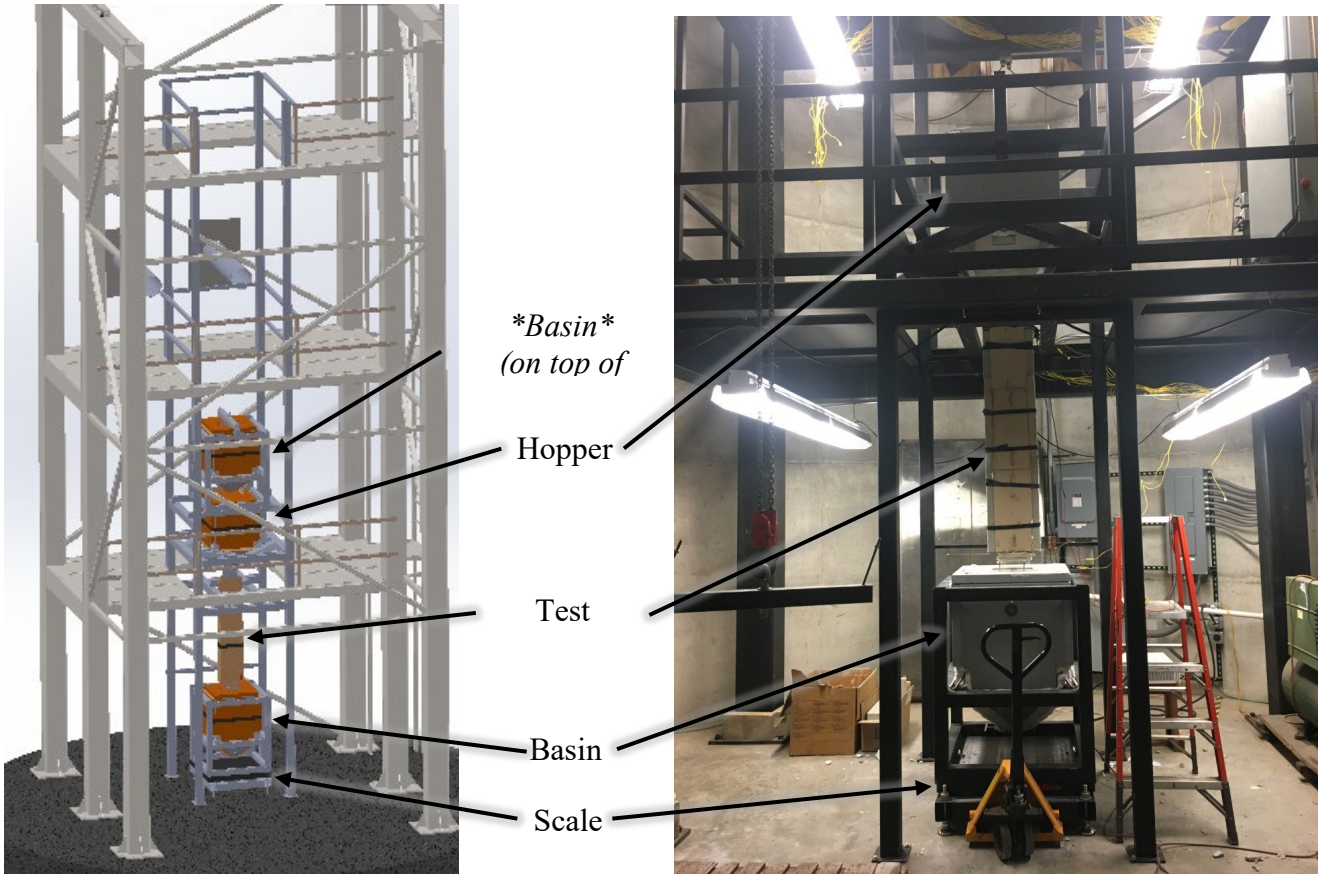

*Figure 48 - Setup of the dynamic rig. Note that only one Basin was built for the rig. *Basin* only indicates the placement of the Basin on top of the Hopper.*

The test section applies a heat flux to one side of the flowing sand using a 316 Stainless Steel, 0.5 mm thick serpentine heater that occupies the length and width of the test section and is shown in Figure 49. The heater is sandwiched between two 0.5 mm Phlogopite Mica sheets and two 6.4 mm thick, 1.55 m by 230 mm 316 stainless steel plates (much like the heater used for the Static test rig) as shown in Figure 50. A Xantrex XDC 40-150 DC power supply is connected to the leads of the approximately 0.5 Ω serpentine heater. The power supply's maximum output is 40 V and 150 Amps. Through holes in the top of these two stainless plates allow for a junction piece to be installed between the test section and hopper. Two Phlogopite Mica plates 3 mm thick and 13 mm wide act as spacers to retain the 203 mm x 3 mm flow area

cross-section, and a 316 stainless steel plate that is 6.4 mm thick, 1.52 m long, and 230 mm wide acts as the backside plate for the flowing sand (i.e., the opposing, non-heated channel wall). 11 small slots along each edge of the test section allowed for #10-24 stainless steel nuts and bolts to evenly compress the three stainless plates, heater, and Mica plates together; the slots are used in place of through holes to accommodate differences in the thermal expansion of the three stainless plates and two Mica spacers which could cause warpage or possible fracturing of the Mica.

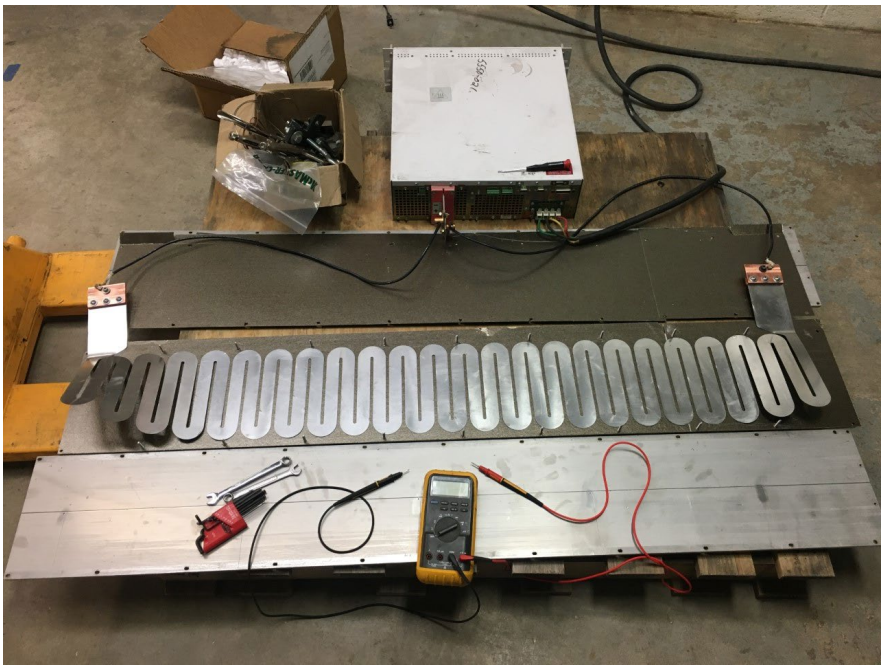

Figure 49 - Open test section with exposed serpentine heater

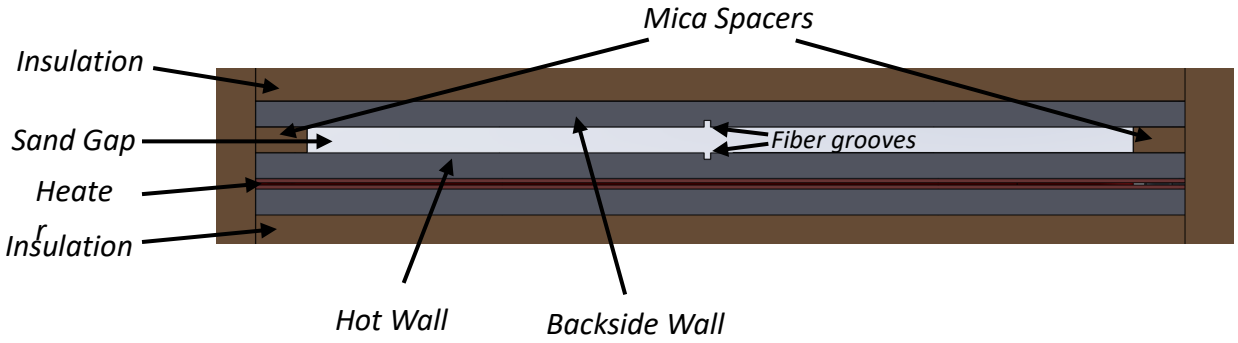

Figure 50 - Cross-section of the test section. The sand gap is 3 mm x 203 mm for reference. Note that the fiber grooves have capillary in place, but fibers were never installed.

Two #10 through holes near the top of the three Stainless plates allow the test section to be suspended solely by two #10-24, 316 stainless steel threaded rods, limiting the contact of the test section with the support structure and therefore decreasing parasitic heat loss. Suspending the test section also limits thermal stress by allowing free expansion of the test section. A tie rod is attached to the restriction valve at the bottom of the test section to prevent swaying, as shown in Figure 51. The test section is surrounded by a layer of high-performance, high-temperature, 5.1 cm thick Promat Microtherm Promalight 1000x PE board.

Figure 51 – Pictured left: top of the uninsulated test section (with hopper and junction in place). Pictured right: bottom of the test section (with basin below).

The restriction valve is mounted to the bottom of the test section via a tab with four #10 holes on the outer plates of the test section. The restriction valve consists of four layers of 6.4 mm thick, 316 stainless steel plates that are sandwiched by #10-24 bolts going through the tabs connected to the test section, as seen in Figure 52. The top layer is a plate that is 5.1 cm wider than the test section on all sides and supports 5.1 cm thick Microtherm insulation installed along the sidewalls of the test section. This plate also attaches to the tie rod to prevent swaying and has cutouts on the extended surfaces to reduce heat transfer by conduction. The second layer contains 26x 5.1 mm holes in line with the flow outlet. The third layer contains sidewalls to allow a restriction valve handle to move with a dead stop portion to halt flow and another portion with the 26x 5.1 mm holes. The flow is modulated by manually operating the valve handle to change the degree of intersection between the 26 holes in the valve handle at the third layer and the 26 holes in the plate on the second layer. The flow rate can be varied between 17.8 g/s or 18.0 mm/s — lower flow rates can cause clogs in some of the 5.1 mm hole intersections — and 80.7 g/s or 81.6 mm/s (i.e., fully open) for Silica #410. Between the second and third layer are 0.5 mm thick Stainless shims that sit above the sidewalls in order to allow clearance for the valve handle to move. The valve handle is thick enough to be hit with a rubber mallet without bending which is necessary as the valve can become sticky due to particles lodging in the crevices during actuation. The fourth and final layer is an outlet piece that is inserted into the basin when the basin is lifted by a pallet jack; this restricts ambient air from flowing up into the test section and also reduces the possibility of exiting particles being lost. Particles flow uniformly at the outlet into the basin which also reduces the possibility of exit

particles “missing” the basin opening. The restriction valve is roughly insulated using Pyrogel XTF.

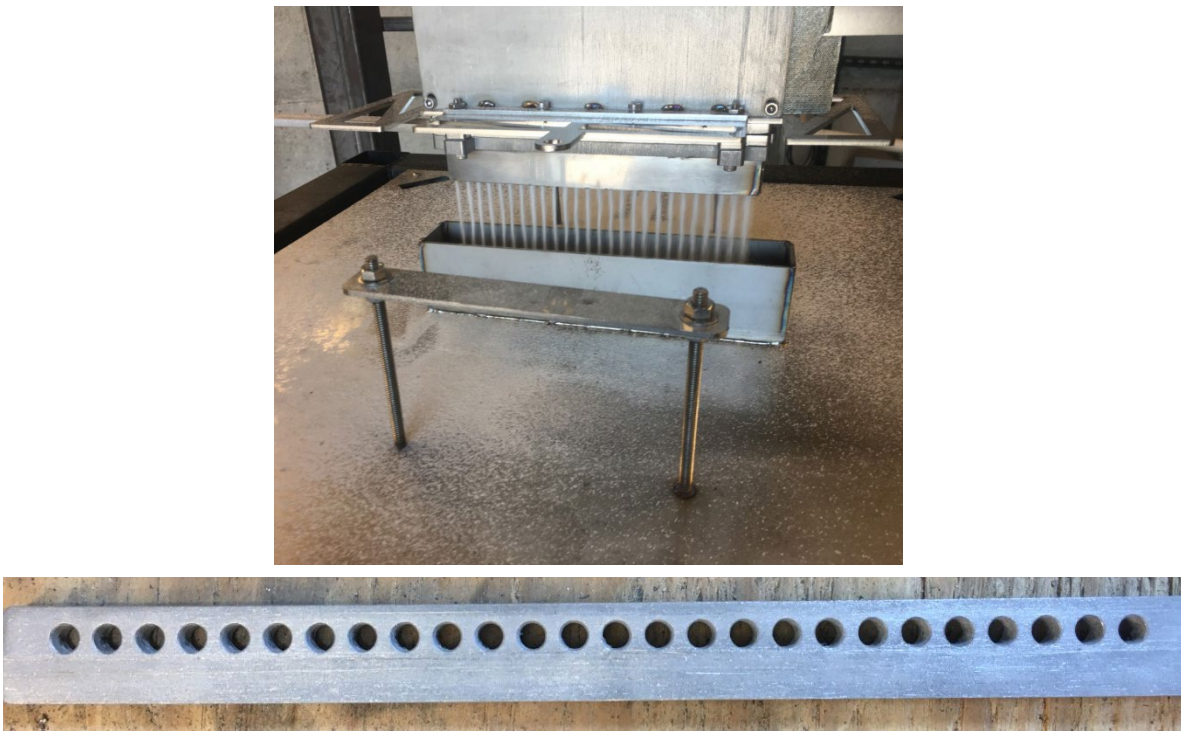

Figure 52 - Close up of the uninsulated restriction valve with sand flowing. Also, the 26 x 5.1 mm hole pattern in the restriction valve handle used for flow control.

Temperature measurements are taken using Omega type K, 0.5 mm Inconel sheath thermocouples installed at the inlet and outlet of the test section and along both stainless plates that form the two sides of the channel that are in contact with the flowing particles. The thermocouples are all connected to a cRIO-9024 chassis via a NI-9213 card, and measurements are recorded via LabVIEW. The hot side refers to the hot plate in contact with the heater and particle flow; the backside refers to the unheated plate in contact with the particle flow opposite to the hot plate as seen in Figure 50.

At the inlet of the test section, there are three thermocouples coming in from the

backside: one at the center and two about 2.5 cm from each edge (of the 203 mm gap). These three thermocouples are sandwiched between the hopper and test section junction and reside at the top of the two 1.55 m test section plates, as shown in Figure 53.

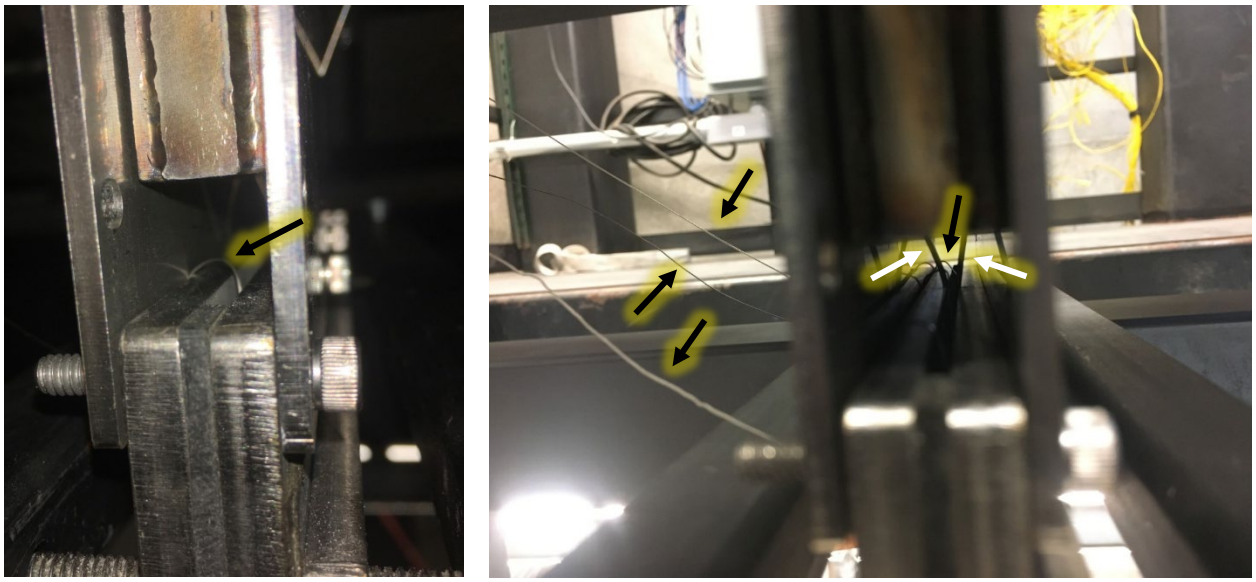

Figure 53 - Inlet thermocouple (indicated by black arrows) and capillary locations (indicated by white arrows) at the top of the test section within and coming into the junction of the hopper and test section. In the right picture, the top and rightmost black arrows are referencing the same edge thermocouple.

At the outlet, there are five thermocouples: two coming in from the hot and cold side at the center, two coming in from the hot and cold side 2.5 cm from one edge, and one coming in from the cold side 2.5 cm from the opposite edge. Note that this last thermocouple on the opposite edge must have become lodged in or near the restriction early on in testing and does not produce valid readings for the outlet flow temperature. The outlet thermocouples are sandwiched between the bottom of the test section and the first/top layer of the test section restriction valve, as shown in Figure 54.

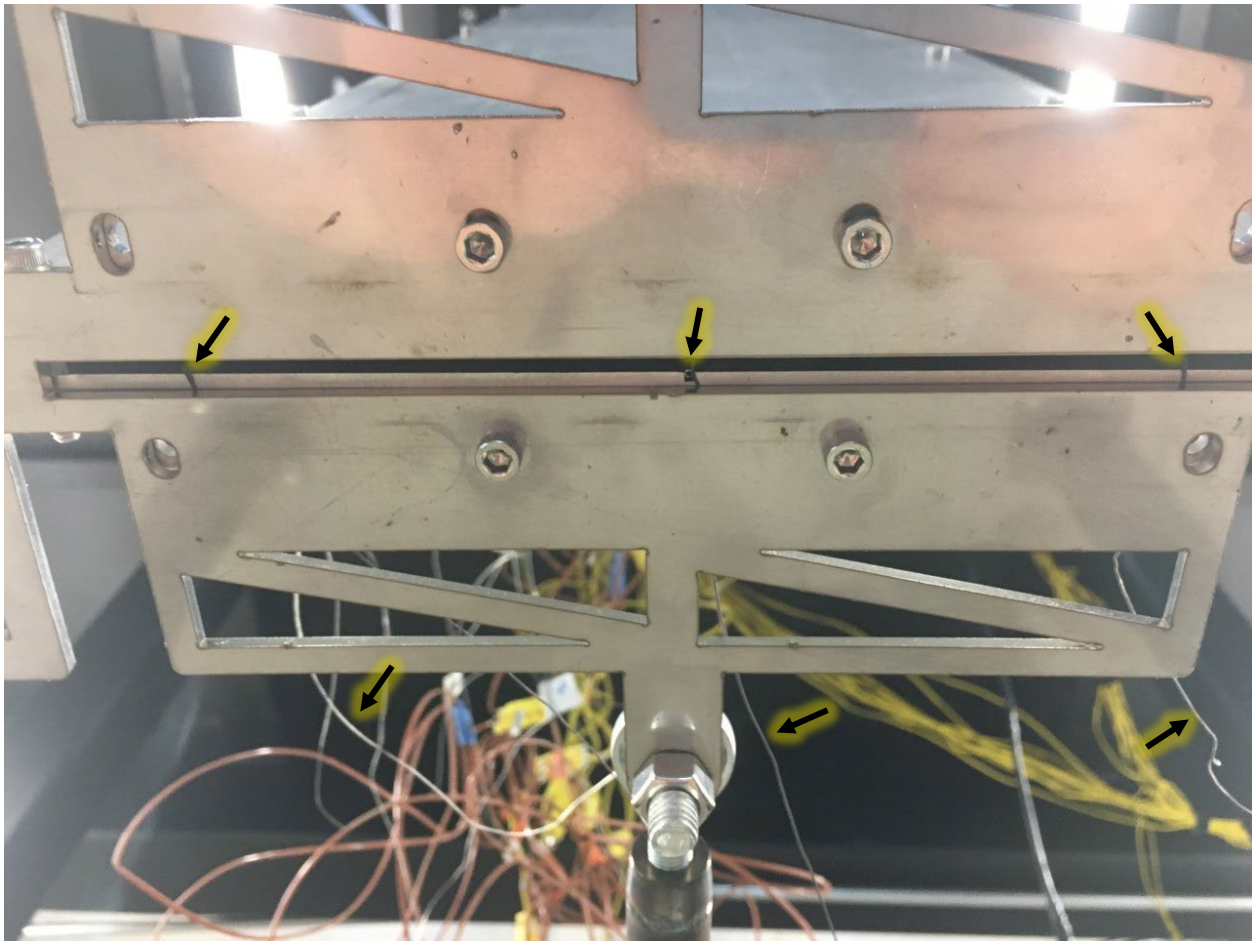

Figure 54 - Outlet thermocouples at the bottom of the test section indicated by the black arrows both inside and outside of the restriction. The bottommost edge of the capillary is next to the center arrow too. Note that only the top/first layer of the restriction valve is assembled onto the test section.

There are five thermocouples installed along the hot plate, and five thermocouples installed along the backside plate. Five 0.5 mm slots were milled into the surface of each plate that is in contact with the flow. These slots run from the edge to the center at 317.5 mm increments with the lowest thermocouple being 63.5 mm from the bottom (i.e., the hot outlet) of the test section. These thermocouples are spaced evenly along the length of flow. As seen in Figure 55, thermocouples were press-fit into these slots and made good thermal contact with the plates as a result of the slight deformation of the sheath from the press-fit. The

thermocouples did not move once fit into place. The thermocouple closest to the inlet on the hot plate broke at the beginning of testing and did not produce reasonable temperatures for the remainder of testing. The locations of all the thermocouples along the test section are shown in Figure 56.

Figure 55 - Press-fit thermocouple (indicated by black arrow) and capillary (indicated by white arrow) on one of the flow plates. Note that the hole near the tip of the thermocouple was originally intended to house a capillary for a fiber running transverse to the flow, but this plan was not pursued due to concerns of locational uncertainties of the measurements and uncertainty associated with conduction along the capillary in the 3 mm gap affecting temperature measurements as well as the fiber's spatial resolution capabilities limiting the number of measurements. As a result, these holes were stuffed to prevent flow leakage.

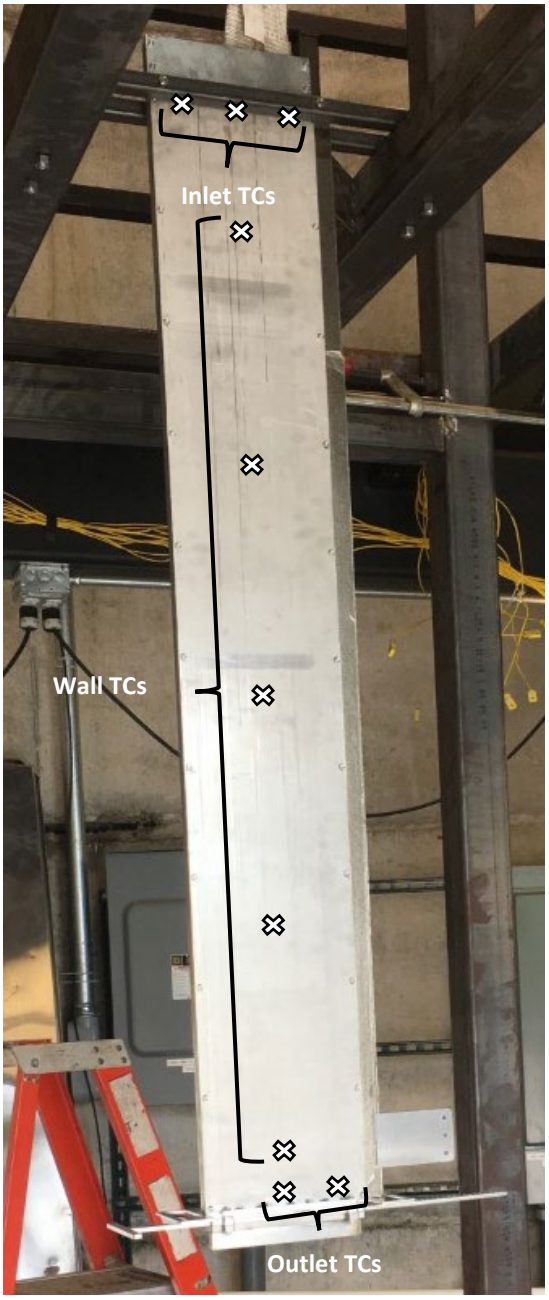

Figure 56 - Thermocouple locations along the test section indicated by the X's. The three inlet TCs all come in from the backside. The wall TCs are on both the hot wall and the backside; note that the topmost hot wall TC is broken. Four total outlet TCs come in from the hot wall and backside wall at the center and one edge; the fifth outlet TC on the opposite edge does not produce reasonable outlet temperatures.

Slots were also milled along the centerline and length of the hot and backside plate on the surface in contact with particle flow in order to fit a 316 stainless steel capillary with 1.6

mm outer diameter and 1 mm inner diameter for eventual use with a fiber-based temperature measurement. A length of capillary has been press fit into each of the hot and backside plates that enter at the junction of the hopper and test section shown in Figure 53 and Figure 57 and butts up to the test section restriction valve shown in Figure 54 and Figure 55. Additional slots needed to be milled in the junction of the hopper and test section to limit curvature of the capillary for fiber installation. Kaowool insulation is stuffed in the gaps where the capillary enters at the junction to prevent particle flow leakage. Fiber optic temperature sensors were not installed in these capillaries during testing as a result of time constraints as well as the fact that useful data could be obtained from the thermocouples alone.

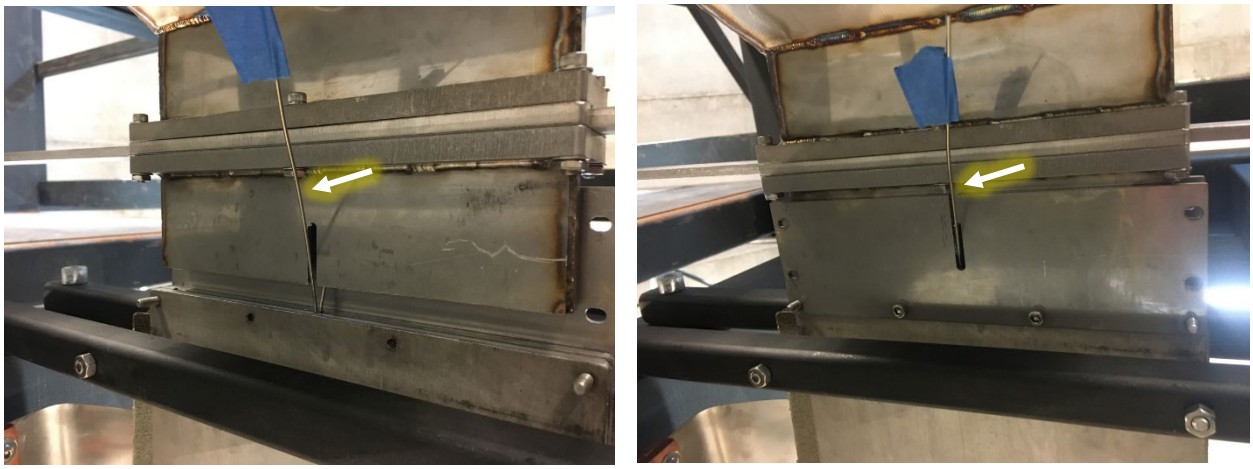

Figure 57 - Assembly of the junction for the hopper and test section with the white arrows indicating the capillary tubing. The left picture is a partially open junction; the right is the closed junction. Note that Kaowool is stuffed in the gaps next to the capillary to prevent particle flow leakage.

The test section is insulated with 5.1 cm thick Microtherm block installed around the majority of the assembly, as seen in Figure 58. Pyrogel and Kaowool insulations are used in areas where the Microtherm block could not fit at the top of the test section near the supports as well as along the test section restriction. Gaps between the Microtherm are also stuffed with Kaowool to prevent heat loss due to natural convection in the gaps of the insulation.

Figure 58 – Pictured left: the majority of the insulated test section on. Pictured right: the insulated top of the test section, the junction, and the bottom of the hopper.

The hopper and basin must hold at least 0.2 m^3 of particles each to achieve the proper flow times that are sufficient to reach steady state. The two vessels are slightly oversized and each hold approximately 0.25 m^3; this additional volume roughly accounts for the angle of repose of the sand which does not allow the sand to fill the top corners of the square volumes. The hopper and basin are designed with valley angles (i.e., the angle along the corner of the converging section) of approximately 45°, greater than the angle of repose for Silica #410. According to [32], the vessels should produce a "funnel flow" of the particles rather than a "mass flow" which results in better mixing of the particles to mitigate temperature gradients in the supply sand and segregation by particle size. Regardless, the valley angle would need to be much steeper to allow mass flow which may have resulted in the basin being too tall to clear the third deck due the chain hoist's maximum height limitations.

Another initial design error was treating the particles as a fluid with hydrostatic pressure in the containment vessels when the particle pressures are not hydrostatic due to compressibility, internal friction, cohesion, wall friction, and permeability. As described in [32], particles in a containment vessel exhibit less wall stress than they do vertical stress during filling and containment in both the bin and the converging section, and these wall and vertical stresses can change during discharge. The Silo Stress Tool by Dietmar Schulze [34] is a software that can be used to analyze wall and vertical stresses of particle vessels during filling, but only provides these stresses for filling and mass flow discharging, not funnel flow. The Static Structural tool in ANSYS Workbench was used to analyze the stresses in the containment vessels which are fabricated from laser cut and welded 3.2 mm thick, 316 stainless steel plate. The results are shown in Figure 59. The particles were treated as an incompressible, hydrostatic fluid with gravitational effects which means that the wall stress' factor of safety of 4.3 at 315°C is actually lower than the true factor of safety for particles.

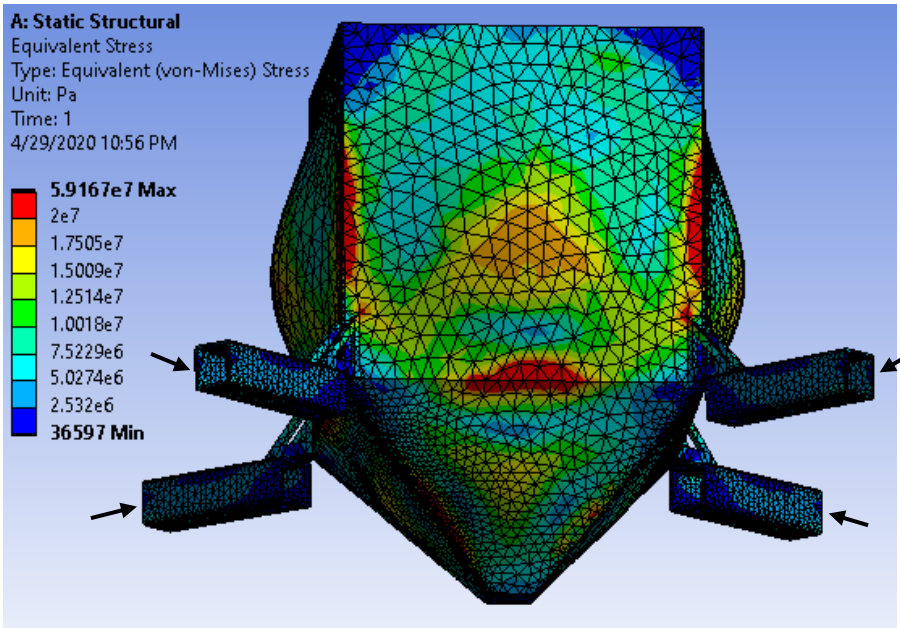

Figure 59 - ANSYS analysis of wall stresses treating the particles as a hydrostatic fluid with a constant density of 1625 kg/m3 (the same as measured for Silica #410) and using gravity. The assembly has fixed support boundary conditions at the four arrows.

The supports for the basin and hopper were also analyzed using ANSYS static structural analysis, and the results are shown in Figure 60. The supports are made up of 9.5 mm thick, 316 stainless steel laser cut pieces welded to the corners of the vessels. One of the four supports at the edge of the vessel was analyzed under one quarter of the total load of the combined basin/hopper and sand, an estimated 1330 N (or 136 kg). A vertical load was applied along the portion of the support in contact with the vessel, and a fixed boundary condition was used on the opposite end of the square tube that the support rests upon. This support design has a factor of safety of approximately 3.44 at 315°C using 316 Stainless Steel for the assembly.

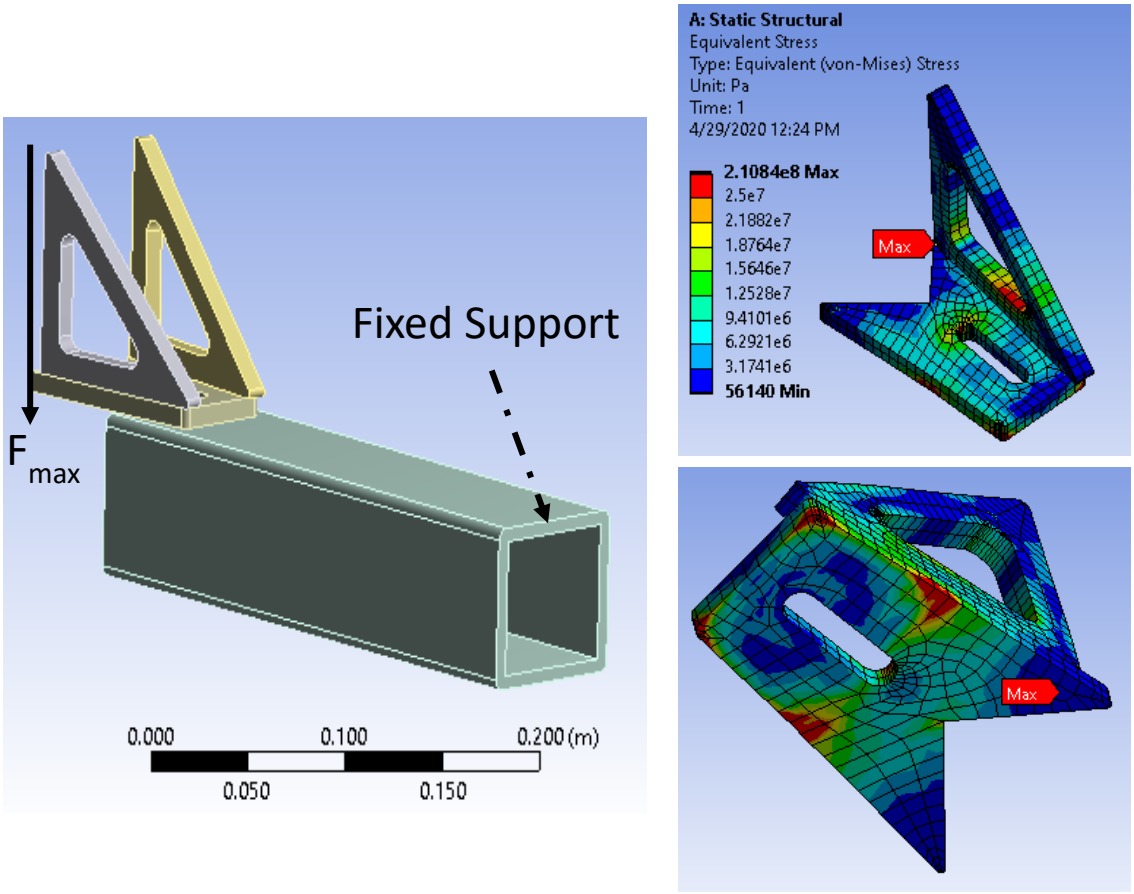

Figure 60 - ANSYS static structural analysis of one of the supports used on the corners of the basin and hopper. The applied load (F_{max}) is 1330 N (or 136 kg).

ZIRCAR Refractory Composites Inc.'s Zical-18 board insulates the hopper and basin, and Kaowool insulation fills in the gaps that the ZIRCAR cannot cover, as seen in Figure 61. Platform pieces are installed along the edges of the basin and hopper for the ZIRCAR board to rest upon; these platform pieces have cutouts to reduce heat transfer via conduction. Tapped holes in the sheet metal of the hopper and basin allowed ¼-20 stainless threaded rod to be partially screwed in and spot welded. These threaded rods act as supports for the ZIRCAR board to hold them in place using oversized washers and nuts on the sidewalls of the vessels. On the converging section, the threaded rod goes through the ZIRCAR insulation and then external plates, which are held on using nuts, apply even pressure to the insulation. These

external plates include an extended portion at the top to allow Kaowool to be stuffed along corners of the bin and the converging section of the vessels. Stainless steel wire runs through holes on these external plates to hold Kaowool against the corners of the converging section.

Figure 61 - Pictured left: uninsulated hopper with exposed threaded rod and platform pieces as well as I-tabs for lifting the hopper independent of the structure. Pictured right: fully insulated basin in the basin cage on weight scale with external plates installed.

Both the hopper and basin have lid handles and I-tabs. The lid handles allow the lids of the hopper and basin to be removed, as shown in Figure 62. The threaded rod extensions are used to create the lid handles and hold the ZIRCAR board insulation on the lid in place. There are two 9.5 mm thick, 316 stainless steel I-tabs welded in opposite corners of both the hopper and basin that allow the vessels to be lifted separately from an external support structure, as seen in Figure 61; these I-tabs are only rated to lift the weight of the vessels without sand.

Figure 62 - Insulated hopper in place with lid handles on top; the ZIRCAR board cover piece in place over the hole in the hopper lid; and the throne assembly for aligning basin when lowering on top of hopper.

The basin's converging section is symmetric while the hopper converges to a size that matches the test section flow cross-sectional area. The valve for the basin, shown in Figure 63, contains three layers and is designed similar to the test section restriction. The first and top layer is a large plate welded onto the 7.6 cm by 7.6 cm outlet of the basin with bolt holes. The sizing of the outlet allows the full basin to be emptied into the hopper within a couple of minutes. The second layer consists of side walls and a valve with a fully open and dead stop portion; the valve has tabs on either end to allow the valve to be actuated to either the fully open or dead stop portion without coming out of the assembly. There are 0.5 mm shims between the first and second layer to provide the clearance necessary to allow the valve to slide. The valve is also made of a relatively thick plate so that it can be pounded on using a rubber mallet to overcome any stickiness related to particles getting stuck in crevices of the

assembly. The third and bottom layer is the underside support of the valve which contains a cross-hatch to prevent the dead-stop portion from bowing under the weight of the sand.

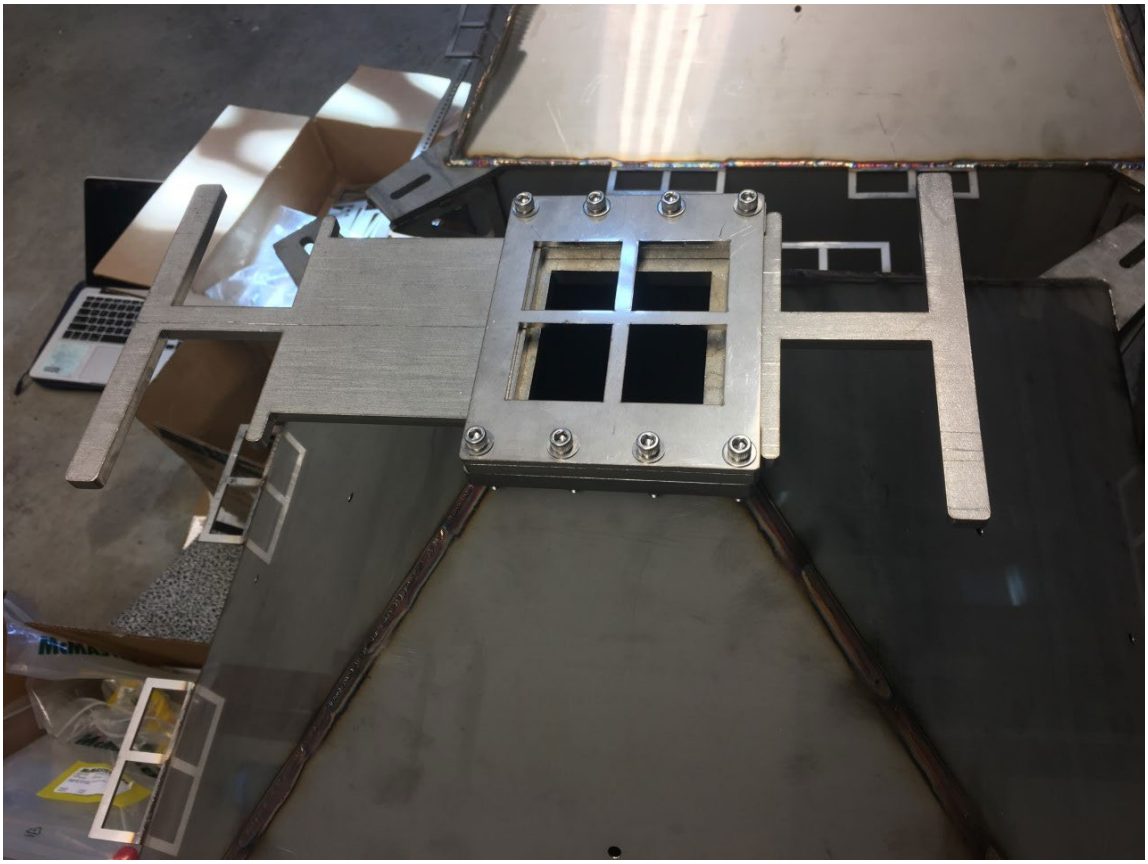

Figure 63 - Basin valve assembly in the fully open position.

The hopper shutoff valve located at the outlet of the hopper allows flow to be stopped prior to entering the test section; however, the hopper valve is normally in the fully open position. The valve contains three layers like the other valves and is shown in Figure 64. The valve includes a welded-on straight section that fits into the hopper and test section junction and sits 2 cm above the test section as seen in Figure 57. The junction contains two tall, thin plates bolted to the test section and two sidewall pieces bolted between those plates to close the edge gaps shown in Figure 65; the thin plates allow for the junction to slightly deform to

make a tight seal against the test section inlet and hopper valve assembly outlet. One interesting note is that if the hopper and test section are full of sand, the shutoff valve can leak slightly when actuated because of the momentary opening between the fully open portion of the actuating piece and the opening where the valve fits in.

Figure 64 - Hopper valve assembly in the fully closed position. Note that this picture was taken before the threaded rod to hold the ZIRCAR insulation in place was tacked into the sidewall holes of the converging section of the hopper.

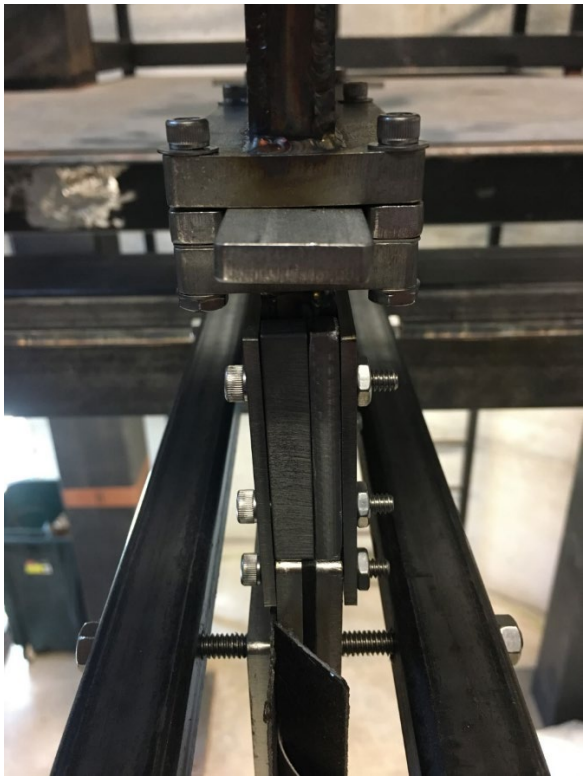

Figure 65 - Side profile of the hopper and test section junction showing one side of the junction sidewalls.

To be able to lift, move, and protect the basin, a basin cage was fabricated. The cage is welded together from 7.6 cm carbon steel square tube with 3.2 mm thick sidewalls shown in Figure 66. This compact design allows for clearance over the third deck when lifting and also allows the cage to fit onto the scale. The chain hoist clevis attaches to a steel eye bolt on a length of 7.6 cm square tube bolted on top of the basin cage; this length of square tube is removed when moving the basin underneath the test section for flow testing. The cage can be set on the scale or above the hopper such that the valve assembly for the basin slightly hovers above the ground or the hopper. The cage and its lifting mechanism are designed with a higher factor of safety to accommodate additional loads that might be associated with the cage

swaying, twisting, or getting caught under the silo structure while lifting as well as any sort of bumping or banging (usually with the cage rattling between the throne alignment pieces).

Figure 66 – Pictured left: the basin in the cage on top of weigh scale with clevis attached. Pictured right: the basin on top of the hopper between throne alignment pieces

Throne alignment pieces, as seen in Figure 62 and Figure 66, are added above the hopper to aide a single user in lowering and aligning the basin on top of the hopper because the chain hoist toggle switch is on the third level; these throne pieces consist of vertical square tube with angled edges at varying heights to align the basin as it is lowered. Climbing the ladder to the third level is a necessary part of lowering the basin on top of the hopper because the pull chain to move the I-beam that the chain hoist rests upon is manually operated.

The scale is a 900 kg capacity, 91 cm by 91 cm Rice Lake RoughDeck HP floor scale connected to an Avery Weigh-Tronix ZM303 indicator with an analog output card addon as seen in Figure 67. A square tube pallet was welded that has adjustable feet. The scale rests upon this pallet, and the clearance below the pallet allows the scale and the basin to be moved together with a pallet jack. The indicator is mounted to the external support structure of the silo and can withstand humid and reasonably hot and cold ambient conditions which is important because the silo does not have air conditioning.

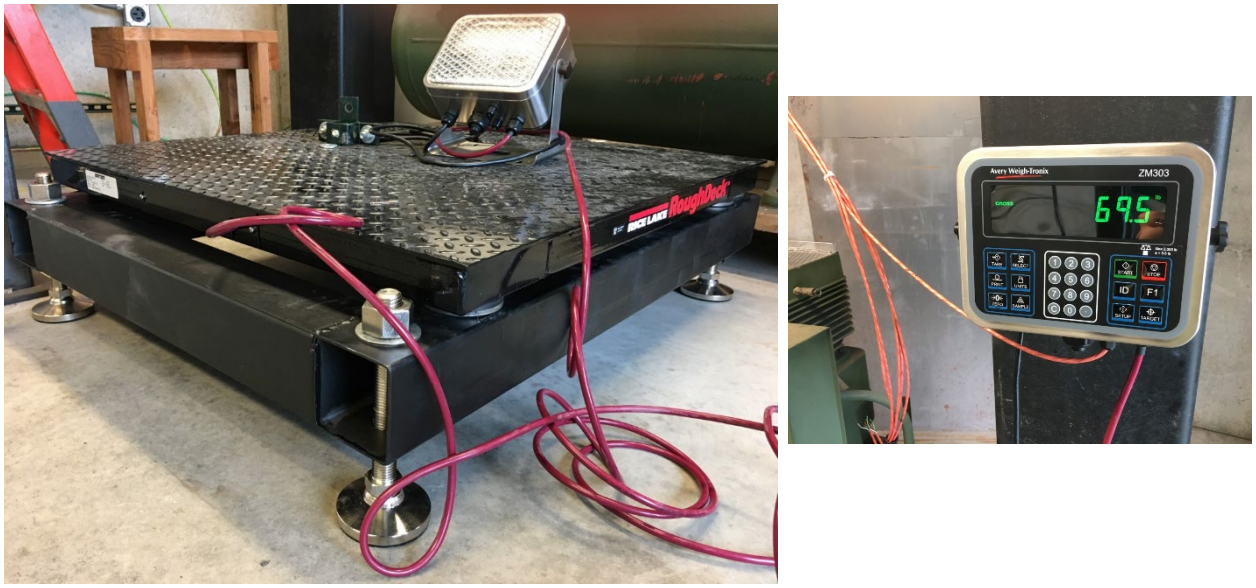

Figure 67 – Pictured left: RoughDeck weigh scale with ZM303 indicator on the custom pallet. Pictured right: mounted indicator

The ZM303 indicator has internal scale and analog output calibrations as well as zeroing, taring, and many other functions that can be set using the push buttons on the indicator. The resolution of the indicator display is +/- 0.2 kg. The analog output card with the 4-20 mA output setting is necessary to allow the ZM303 indicator to communicate with the cRIO-9024 chassis via a 250 Ω shunt resistor and a NI 9205 card. The resistor creates a 1-5 V signal with

1 V corresponding to 0 kg on the scale and 5 V corresponding to 900 kg on the scale which is calibrated via software embedded in the ZM303 indicator. An NRSE (non-reference signal end) wiring orientation, which can be found in the NI 9205 manual, improves signal performance by limiting noise. Data is recorded using LabVIEW.

Proper precautions that must be taken when handling hot sand and valves include (but are not limited to) safety glasses, long-sleeves, pants, close-toed shoes, heat-proof gloves, and a respirator. Though particle loss is generally not an issue, heat-proof clothing and a face shield should be worn when handling high temperature particles. A rubber mallet can be used to actuate the valves at a safe distance, but care should be taken not to hit the valves too hard and cause bending. A respirator is required due to airborne dust from the agitated particles and insulation and associated silicosis hazards. The insulation can irritate the skin. There is a possible electrical shock hazard due to the high-power current source used as well as other electrical components. There is a possible fall hazard associated with climbing up and down the ladders and working from heights. The work can be strenuous and lead to fatigue after multiple rounds of testing, especially because the silo is not air-conditioned. Make sure to take rest breaks in the main building of the Tantalus facility to consume fluids and food, to cool off in the hot summer to prevent dehydration and fainting, and to warmup during the cold winter to prevent hypothermia. Though the operator controls the chain hoist from the third deck, special care needs to be taken to ensure that the heavy components are properly secured before lifting and that people are not underneath and at a safe distance from the lifted component. Spillage of the hot sand from the suspended basin is another possible concern, but this has yet to occur. The full procedure for one cycle of the dynamic test rig is provided below.

1. Check to make sure that the test section outlet valve is in the fully closed position and the hopper outlet valve is in the fully open position. Ensure there is sand in the basin.
2. Plug in the current source and scale and ensure that these components are function properly. Zero the scale if necessary.
3. Ensure that the LabVIEW program is properly recording data. The LabVIEW program is typically set to record an average of 100 measurements every one second for the scale and each thermocouple input. Check to see if the current thermocouple and scale readings are reasonable.
    a. The computer used to collect and display LabVIEW measurements is located on the inside of the Tantalus facility, so traversing between the silo and the main building throughout the experiment will be necessary to keep an eye on the dynamic rig and the measurements being taken.
4. Use a pallet jack to move the basin underneath the chain hoist and attach the clevis and crossbar by hand tightening two lengths of threaded rod, aluminum spacer, washers, and nuts until the crossbar has very little free play as shown in Figure 66.
    a. If necessary, move the scale on top of the metal pallet using the pallet jack to a position that the basin cage can eventually be lowered upon using the chain hoist.
5. Climb the ladder to the third deck, and locate the chain hoist control toggle switch.
6. Engage the toggle switch to lift the basin cage assembly. Ensure that the basin cage does not catch on anything while lifting and that the chain does not twist excessively.

7. Once the basin cage is clear of the third deck shown in Figure 68, use the manual pull chain to move the chain hoist and basin cage over the center hole and hopper. Try to keep swinging and twisting of the basin cage to a minimum and to prevent the basin cage from hitting the structure.
    a. Pull the chain smoothly and slowly to prevent jamming or slipping.
    b. Sometimes the shaft and wheels to move the I-beam supporting the hoist can jam in one direction. If the pull chain does not move in one direction, operate the pull chain in the opposite direction. Keep operating back and forth until the pull chain operates smoothly.

Figure 68 – Pictured left: lifting basin above the third deck. Pictured right: lowering basin through center hole over hopper.

8. Lower the basin cage on top of the hopper. Use the throne alignment pieces to guide the basin cage; the basin cage may bounce quite a bit between the throne pieces. If necessary, manually pull and twist the chains to help align the cage over the hopper and prevent the cage from being lowered onto the corners of the lid.
9. After the basin cage is safely seated on the supports above the hopper, climb down to the first deck, ensure the test section valve outlet is completely closed and hopper outlet valve is fully open, remove the 23 cm by 23 cm ZIRCAR board above the hopper inlet in the lid (seen in Figure 62), and check that the basin outlet is aligned with the hopper inlet.
    a. If this is the first flow test being performed after several days of downtime, it is strongly suggested to sieve the particles that are leaving the basin and entering the test section. Bugs (i.e., flies and spiders) and other debris, as seen in Figure 69, have gotten into the particles and can block flow passages, which can result in negating entire tests. A #12 sieve (1.6 mm openings) is used for the setup described in this thesis. The basin may need to be slightly suspended above the hopper in order to fit the sieve on top of the hopper. Only partially open the basin valve when sieving; otherwise, the sieve will overflow. Sieving can take approximately a half hour.

Figure 69 - Leftover flies and debris from one of the first times sieving on 8/10/2020.

b. If sequential testing is being performed then do NOT sieve between tests unless absolutely necessary. This can be hazardous due to the hot sand as well as cause significant heat loss due to the increased transfer time compared to transferring without a sieve.

10. Open the basin outlet valve fully to fill the test section and hopper as seen in Figure 70. Once the basin is empty, completely close the basin outlet valve and return the 23 cm by 23 cm ZIRCAR board above the hopper inlet.

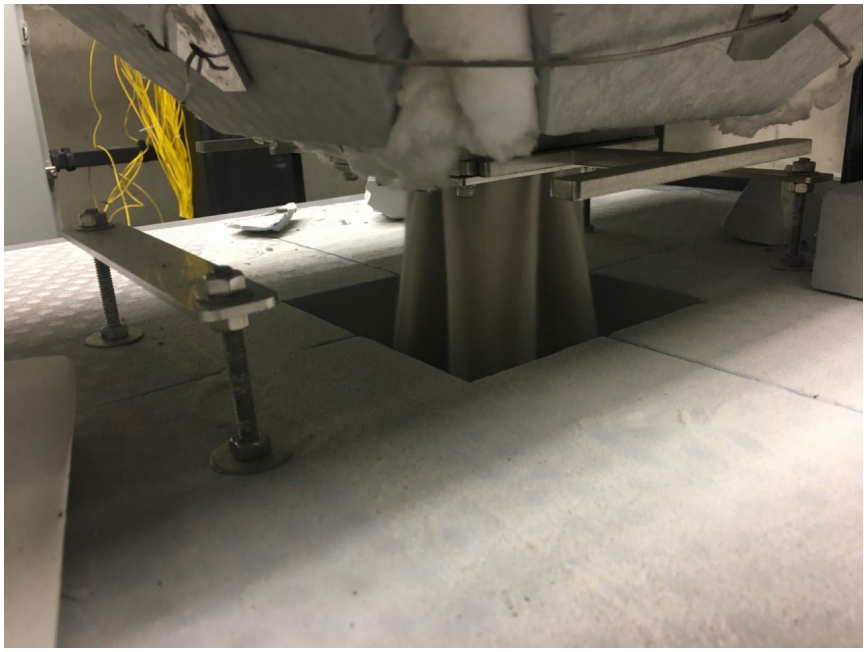

Figure 70 - Transferring sand from basin to the hopper and test section.

11. Climb up to the third deck, use the chain hoist to raise the basin above the third deck, use the chain pull to move the basin outside the center hole, and lower the basin on top of the scale that is sitting on top of the metal pallet.
12. Climb to the ground floor, manually push and turn the basin cage so that it lines up over the scale evenly as seen in Figure 66, and, lastly, remove the clevis and crossbar from the cage.
13. Use the pallet jack to move the basin on the scale on the metal pallet underneath the test section. Raise the pallet jack so that test section outlet fits into the basin inlet as seen in Figure 71.
    a. The clearance between the bottom of the test section and the basin lid handles is very tight when moving the basin underneath the test section.

b. Make sure not to raise the basin too high such that the basin handle presses against the tie rod. This can affect weight measurements.

Figure 71 - Basin on the scale on the metal pallet being moved and raised with a pallet jack underneath the test section.

14. Go to the computer in the main building to begin recording measurements via LabVIEW. Ensure readouts for the thermocouples and scale are still reasonable.
15. Return to the silo and adjust the current source to the proper power input.

a. With the XDC 40-150, the voltage will max out at 40 V for full heater power (and the amperage maximum is 150 amps). For reference, the stainless steel serpentine heater currently installed has a resistance of just over 0.5 Ω.

16. Open the test section outlet restriction valve to initiate flow. Ensure particles are flowing evenly out of all holes in the restriction as seen in Figure 52. Use a hand timer to estimate the mass flow rate based on the display output of the ZM303 scale indicator. Adjust the valve as necessary until the proper flow rate is achieved.
17. As the test proceeds, continue to monitor the temperature and weight measurements on the computer in the main building as well as the dynamic rig in the silo.
    a. If there is a significant change in the mass flow rate and the temperatures, there is likely a clog in the flow - this may look like the situation shown in Figure 72.
    b. If the clog is at the test section outlet (indicated by uneven flow through the restriction holes at the outlet), this can be remedied by actuating the valve. Note that it will likely not be possible to achieve an exact flow rate due to the stickiness of the valve and the difficulty in estimating the flow rates using a hand timer and the display on the indicator.

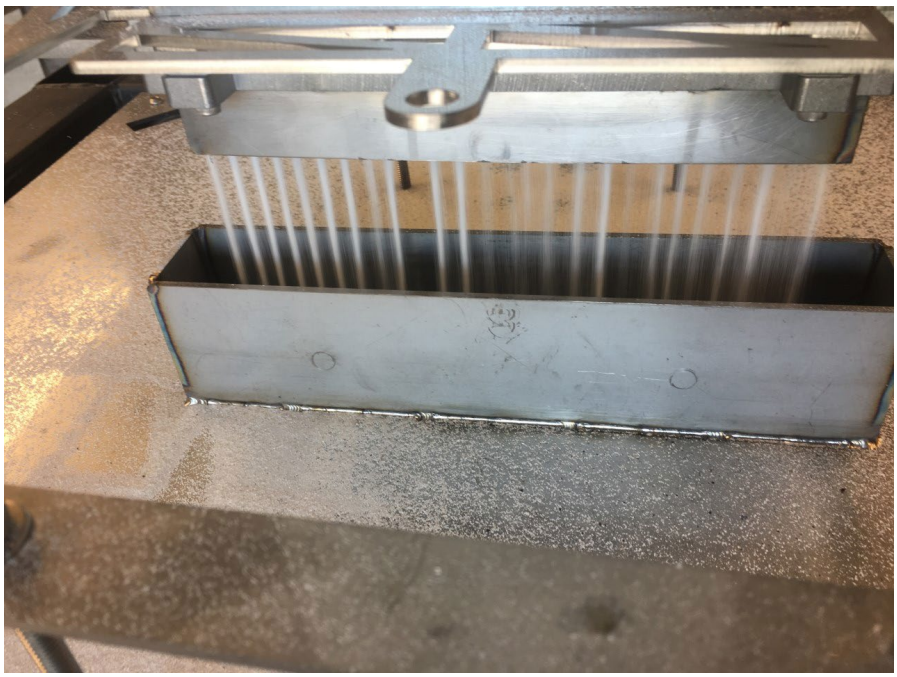

Figure 72 - Example of uneven flow out of the test section.

18. Once the hopper and test section have completely emptied, stop the LabVIEW program, turn off the current source, and completely close the test section outlet valve.
    a. It is recommended to know the exact weight of the full basin in order to anticipate when flow will end so that it is possible to complete this and the following steps as quickly as possible.
    b. Make sure to save the acquired LabVIEW data
19. Use the pallet jack to remove the basin, scale, and metal pallet from underneath the test section.
    a. If performing another test immediately following the current one, return to the beginning of this procedure. Proceed quickly and cautiously to limit transfer time and heat loss.

b. If concluding testing for any substantial period of time, cap the basin inlet on the lid with the 7.6 cm x 30.5 cm ZIRCAR cutout to prevent bugs and debris from getting into the particles.

Dynamic Testing Analysis for Heat Transfer Coefficients

34 data points at various mass flow rates and bulk temperatures were acquired to determine heat transfer coefficients, Nusselt numbers, and heat losses for the flowing sand. The heat losses from the dynamic rig test section and the heat transfer coefficient associated with the flowing sand can be determined once thermal steady state is reached using the inlet, outlet, and wall thermocouples and the mass flow rate of sand determined from the scale. The total rate of heat transfer to the sand ($\dot{q}$) is computed from:

$$\dot{q} = c_p \, \dot{m} \, (T_{out} - T_{in}) \tag{27}$$

where c_p is the specific heat capacity of the sand (found using the NIST-JANAF tables for Quartz [30]); $\dot{m}$ is the mass flow rate determined by recording weight measurements over time; T_{out} is the test section outlet temperature; and T_{in} is the test section inlet temperature. The energy transfer to the sand can be compared to the power input to the heater:

$$\dot{q}_{cs} = I \, V \tag{28}$$

where $\dot{q}_{cs}$ is the power supplied by the current source; I is the current taken from the display of the current source; and V is the voltage taken using a multimeter across the two leads of the serpentine heater. The fraction of the heat loss from the dynamic rig ($Loss$) can then be calculated according to:

$$Loss = \frac{\dot{q}_{cs} - \dot{q}}{\dot{q}_{cs}} \tag{29}$$

The local heat transfer coefficient of the flowing sand (h) is estimated using the bulk temperature of the flowing sand (T_{bulk}) and the hot wall temperature ($T_{hot,wall}$) along with the

heat input determined in Equation (27); note that this assumes that the heat flux at the wall of the test section is uniform, a good assumption given the construction of the heater.

$$h = \frac{\dot{q}}{A_{c,wall}\,(T_{hot,wall} - T_{bulk})} \qquad (30)$$

The cross-section of the wall ($A_{c,wall}$) is 203 mm x 1.52 m. The bulk temperature of the sand varies the inlet to outlet temperatures of the test section. For a given run at steady state, the local heat transfer coefficient is calculated using each of the four thermocouples (i.e., N=4) on the hot wall ($T_{hot,wall,i}$) using the associated bulk particle temperature at that location ($T_{bulk,i}$); the average of these four local heat transfer coefficients is taken to be the measured heat transfer coefficient for that run. Note that each of these locations are in the fully developed region of the test section, and, therefore, these measurements are essentially four separate measurements of the fully developed heat transfer coefficient rather than being a true average heat transfer coefficient that includes the developing region.

$$h_i = \frac{\dot{q}}{A_{c,wall}\,(T_{hot,wall,i} - T_{bulk,i})} \qquad (31)$$

$$h = \sum_{i=1}^{N} \frac{h_i}{N} \qquad (32)$$

The fully developed Nusselt number can then be calculated using:

$$Nu = \frac{h\,D_h}{k} \qquad (33)$$

where the hydraulic diameter (D_h) is defined as:

$$D_h = \frac{4A_c}{P} \quad (34)$$

and the cross-section (A_c) and perimeter (P) are calculated from the geometry of the channel, 203 mm x 3mm. The conductivity (k) of Silica #410 is found via a curve fit of the data measured using the static rig:

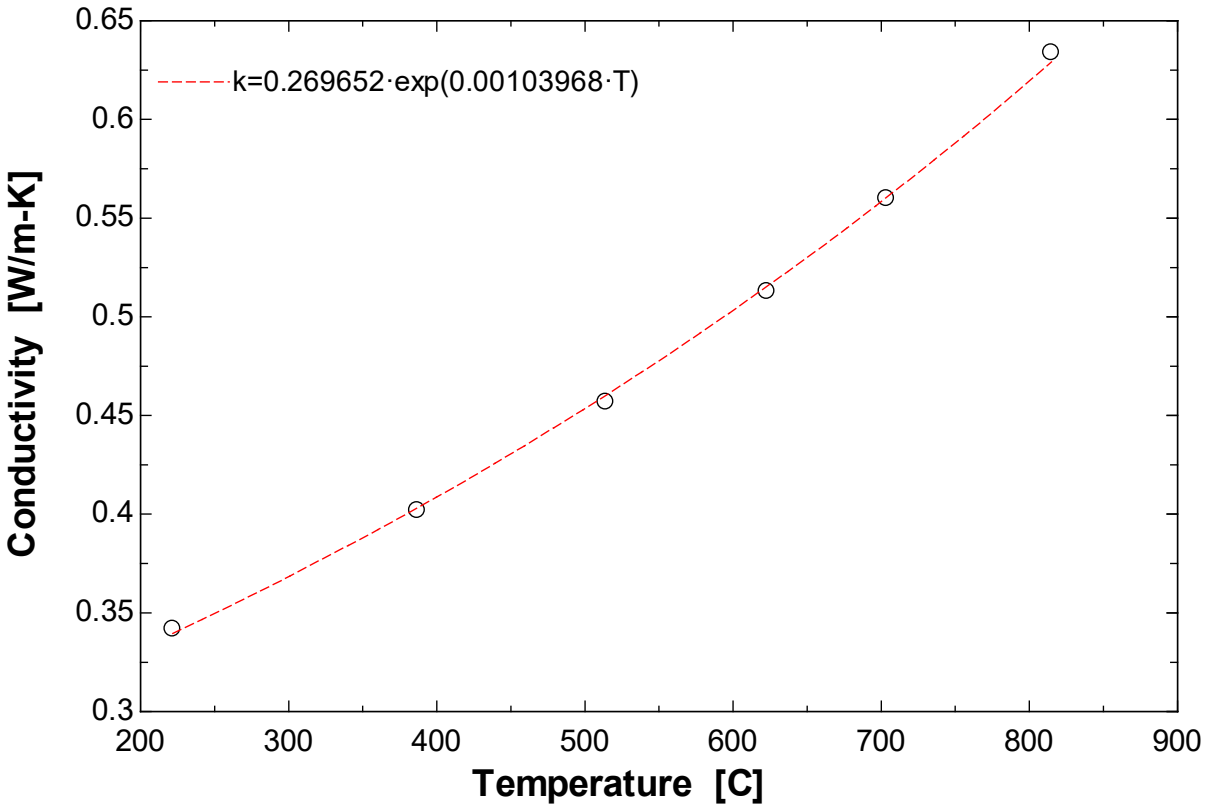

Figure 73 - Curve fit of thermal conductivity as a function of temperature for Silica #410 measured using the static rig.

The temperature used to approximate the conductivity is the average temperature of the sand in the test section defined by:

$$T_{avg} = \frac{T_{in} + T_{out}}{2} \quad (35)$$

The local bulk temperature is not measured directly due to the small size of the sand gap at 3 mm and the presence of a large temperature gradient across this small gap. Thus, the local bulk temperature of the flow must be calculated. The estimation of the local bulk temperature can be done using two methods, both of which assume that the bulk temperature increases linearly with distance along the test section (which is consistent with a uniform heat flux applied at the wall in the absence of heat loss).

The first method, which is referred to as the "inlet-outlet method," calculates the bulk temperature of the sand using the measured inlet and outlet temperatures:

$$T_{bulk,i} = (T_{out} - T_{in})\frac{x_i}{L} + T_{in} \qquad (36)$$

where x_i is the local position along the test section corresponding to the four, functioning hot wall thermocouples (i.e., at locations 51 cm, 83 cm, 114 cm, and 146 cm) and L is the total length of the heated test section (i.e., 1.52 m). The main issue with using the "inlet-outlet" method is the relatively large uncertainty associated with the outlet temperature on every run and the inlet temperature on runs in which the sand was previously heated. The gap is small, and the temperature gradient across the gap at the outlet can be large. Therefore, the sand temperature measurements are strongly affected by the location of the thermocouple. This is evident by the relatively wide spread in the outlet temperature measurements due to the low thermal conductivity of the bulk sand. For runs in which the sand had been pre-heated, there can be temperature non-uniformities in the hopper that result in variations in the inlet temperature as well. Runs in which the sand in the hopper is at a uniform temperature (i.e.,

runs without any preheat) lead to a well-defined inlet temperature that can be measured very accurately.

The second method, which is referred to as the "inlet-backside wall method," is motivated by the uncertainty in the outlet temperature together with the relatively accurate measurements that are available on the backside wall (i.e., the unheated wall) shown in Figure 50. The cold wall temperature measurements are very linear and have nearly the same temperature gradient as the heated wall measurements. The "inlet-backside wall method" determines the bulk temperature as a function of position using the inlet temperature of the particles and the temperature gradient (in the flow direction) measured by the thermocouples on the backside wall. The backside wall is composed of 316 Stainless Steel and is insulated beyond the wall, so the backside wall temperature in the fully developed region will have the same temperature gradient as the bulk particle temperature. The "inlet-backside wall" method calculation of the bulk temperature can be summarized as:

$$T_{bulk,i} = \frac{dT}{dx}_{bw} \frac{x_i}{L} + T_{in} \qquad (37)$$

where $\frac{dT}{dx}_{bw}$ is the slope of a linear fit of the five thermocouples located along the centerline of the backside wall (at locations 19 cm, 51 cm, 83 cm, 114 cm, and 146 cm).

In order to determine the uncertainty in the heat transfer coefficient calculated using these two methods, it is necessary to discuss the method for calculating the inlet and outlet bulk temperature of the sand. The inlet bulk temperature is calculated as an average of the three thermocouples at the inlet; one of these thermocouples is located at the center and the other two are 2.5 cm away from each edge of the 203 mm gap (as seen in Figure 56):

$$T_{in} = \frac{T_{in,l,b} + T_{in,c,b} + T_{in,r,b}}{3} \quad (38)$$

The subscripts *l*, *c*, and *r* indicate left, center, and right respectively, an arbitrary orientation of the test section, with left and right being the two edge thermocouples. All of the inlet thermocouples are inserted from the backside (unheated) wall, indicated by the second subscript *b*. The inlet temperature needs to be averaged across the entire inlet (rather than just the centerline) to account for the average thermal capacitance of the sand coming into the system. There were several test cases where the sand at the center of the inlet was not as hot as the sand entering at the edges; these were associated with consecutive sand heat-up tests due to temperature gradients in the supply sand in the hopper. The uncertainty associated with the three thermocouples increases with consecutive heat-up tests as shown in Figure 74.

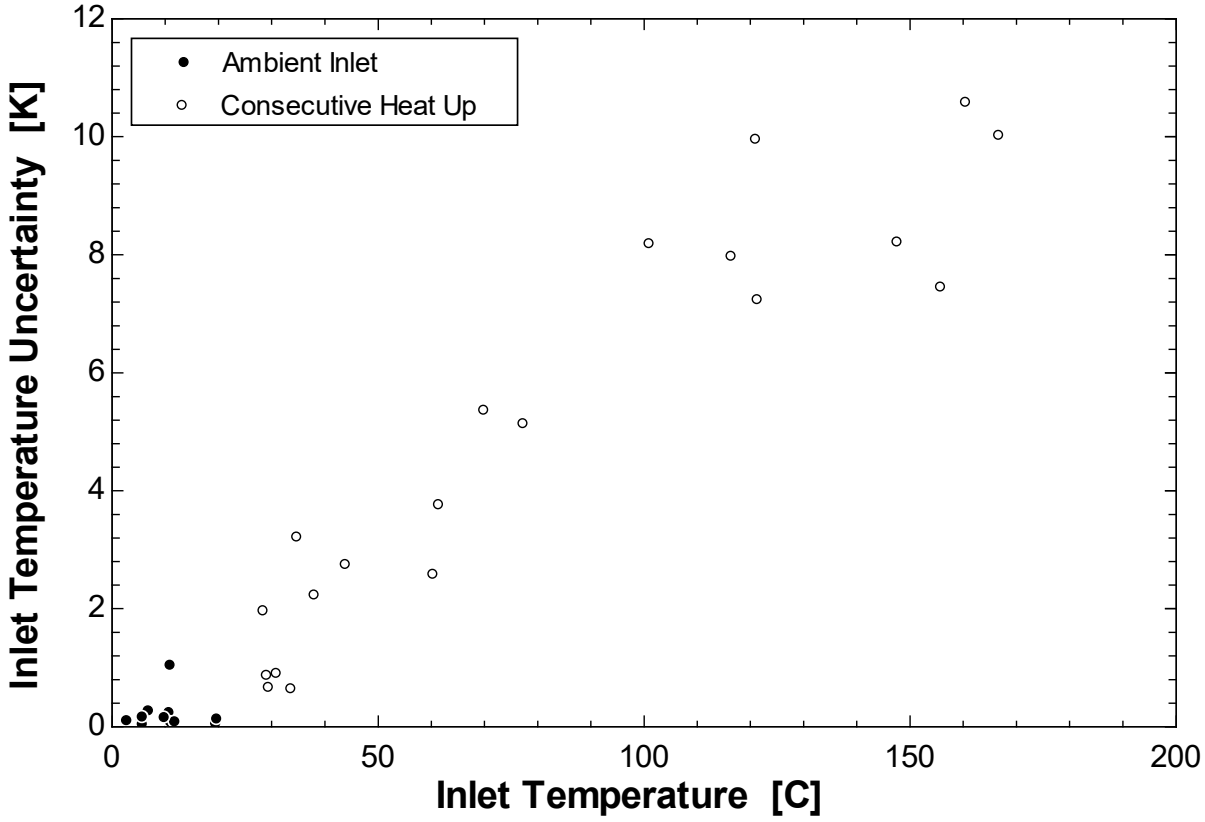

Figure 74 – Uncertainty of the three inlet thermocouples versus the average inlet temperature for all runs.

The outlet bulk temperature can be calculated one of two ways. The first method is referred to as the "outlet edge-center average" technique which uses a modified average of the four usable thermocouples in the outlet channel (as seen in Figure 56):

$$T_{out} = \frac{T_{out,c,h} + T_{out,c,b} + 2\,(T_{out,l,h} + T_{out,l,b})}{6} \qquad (39)$$

where the subscript h indicates the thermocouple is coming in from the hot wall. Note that Equation (39) does not include $T_{out,r,b}$ because this thermocouple was compromised at the beginning of testing. The thermocouple $T_{out,r,h}$ was never installed in the dynamic rig. As a result, the thermocouples on the left edge need to be counted twice to provide proper averaging of the thermal capacitance at the outlet. The thermocouples coming in from the backside wall

and hot wall are differentiated because of possible conduction heat transfer through the 0.5 mm diameter thermocouple sheaths. The backside wall and hot wall thermocouples are both approximately centered in the flow gap, and even checking the thermocouples after several flow tests, they did not significantly bend toward their respective walls. The inlet-outlet method, Equation (36), using the outlet edge-center average, Equation (39), to calculate the bulk outlet temperature provides the full scope of uncertainty at the outlet for estimating parasitic heat loss of the dynamic rig. However, the outlet edge-center average includes edge temperatures which results in lower heat transfer coefficients compared to using only the centerline temperatures; centerline temperatures are more representative of an infinitely wide test section because edge affects do not significantly tamper with the centerline. The uncertainty of the outlet edge-center average decreased with increasing mass flow rate shown in Figure 75.

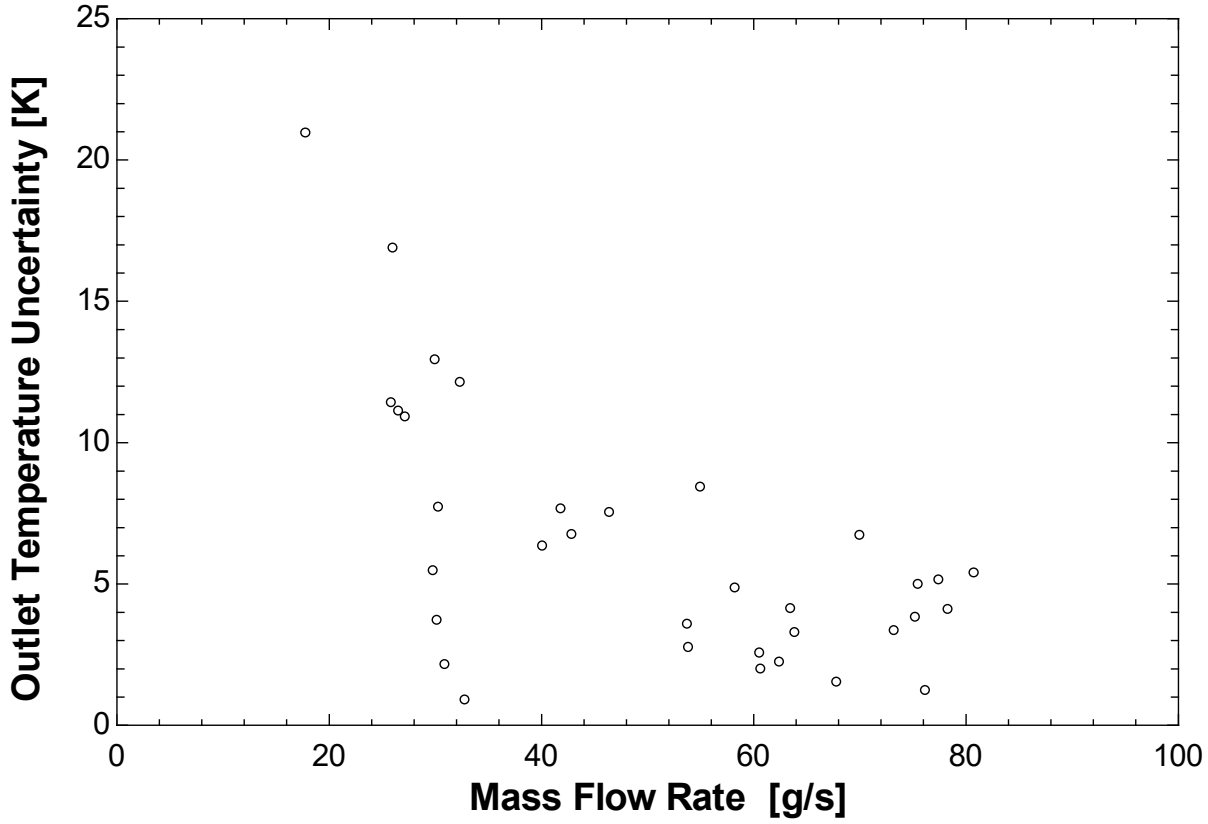

Figure 75 - Standard deviation using the outlet center-edge average versus mass flow rate for all runs.

The second method to calculate the outlet temperature is to use only the center thermocouples which is referred to as the "outlet centerline average:"

$$T_{out,c} = \frac{T_{out,c,h} + T_{out,c,b}}{2} \quad (40)$$

The benefit of the outlet centerline average is that it treats the test section more like an infinitely wide cross-section by ignoring edge effects. The inlet-backside wall method given by Equation (38) uses only centerline data to calculate the bulk localized bulk temperature, and, therefore, the inlet-outlet method using the outlet centerline average method should produce similar results as the inlet-backside wall method. Both of these methods essentially take information only at the centerline of a relatively high aspect ratio channel in order to get a result that is

affected as little as possible by edge effects. There are no particular trends noted for the uncertainty of the outlet centerline average which ranged from 0-6 K. Note that this variation is smaller than the outlet edge-center average in Figure 75.

There were a few runs that had higher edge temperatures than center temperatures at the outlet. This occurred for runs at flow rates above 60 g/s and during consecutive heating trials where the inlet temperature was not uniform. In these cases, the outlet edge-center and centerline averages were mostly within 1°C of each other, so the outlet temperature is approximately uniform from center to edge.

Shown in Figure 76, a comparison of the temperatures for the hot wall, backside wall, and the three ways to estimate bulk temperature: the inlet-outlet method with the outlet edge-center average (Equations (36) and (39)), the inlet-outlet method with the outlet centerline average (Equations (36) and (40)), and the inlet-backside wall method (Equation (37)). The latter two bulk temperature estimations have similar profiles because they both only use centerline temperatures.

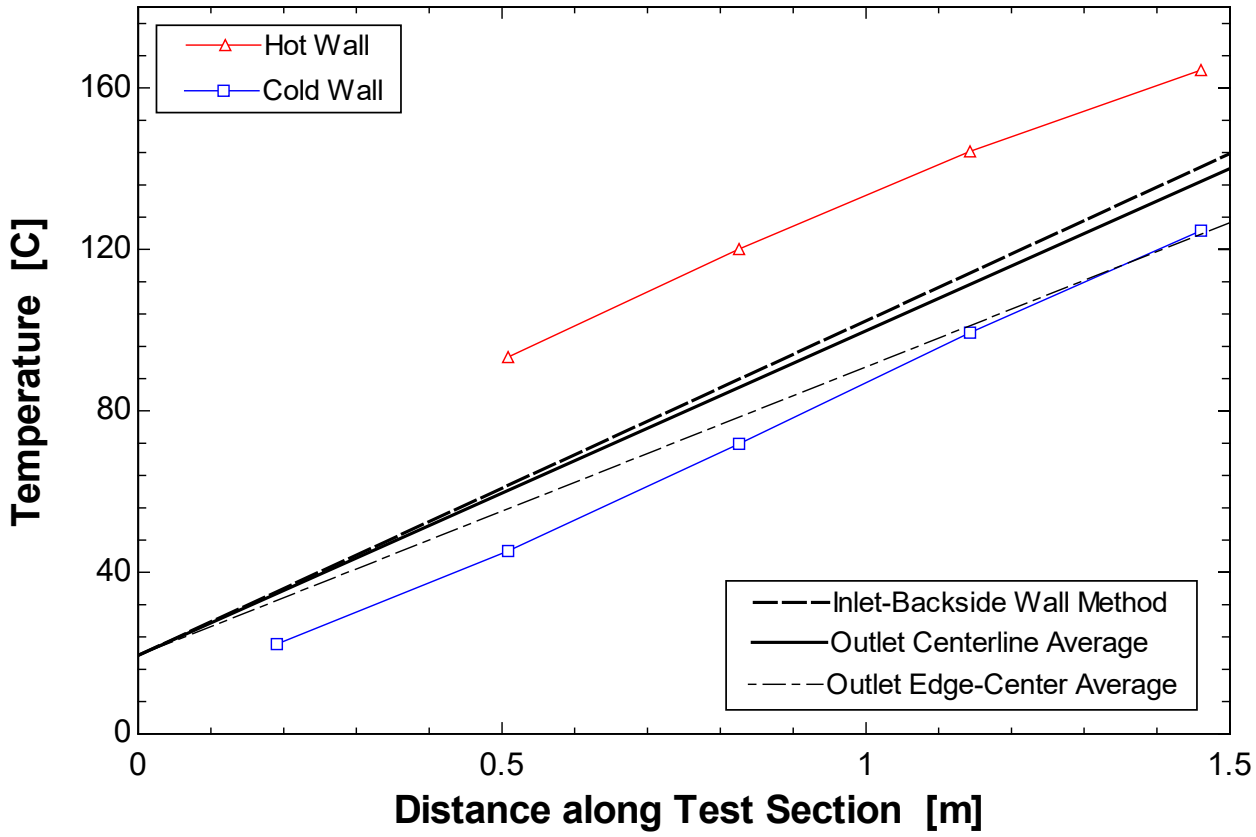

Figure 76 – Temperature profiles of the walls and estimated bulk. Note that the outlet centerline average and the outlet edge-center average both use the inlet-outlet method. Temperature data is taken at 27.2 g/s (27.5 mm/s) with ambient supply sand on 11/9/2020.

The mass flow rate of the sand did not vary significantly over the course of a test (assuming that no blockage occurred). The chi squared values of a linear fit to the mass accumulated in the basin as a function of time is above 0.9998 for most runs and above 0.999 for all runs. An example of this is shown in Figure 77; the slope of the fit is the mass flow rate. Also, the test section walls did not noticeably degrade over the course of testing as a result of the sand flow.

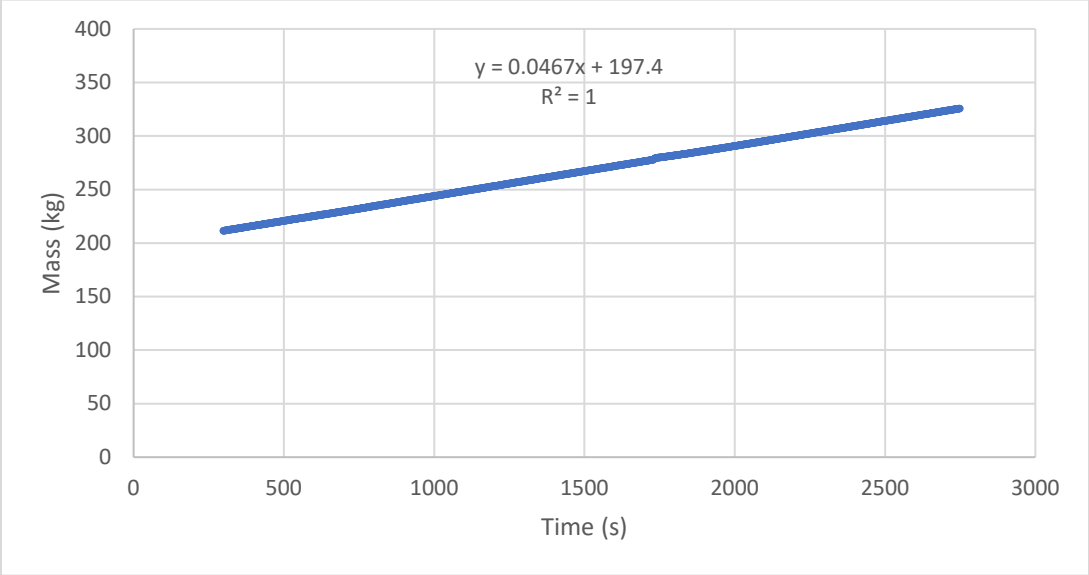

Figure 77 - Mass of the combined basin in the cage with accumulating sand over time for a test with half the total sand used. Taken from a 6th consecutive run on 11/19/2020. The mass flow rate is 46.4 g/s, and the velocity is 46.9 mm/s.

The velocity can be calculated from the mass flow rate according to:

$$v = \frac{\dot{m}}{\rho\, A_c} \qquad (41)$$

which assumes the density (ρ) is constant and equal to the density of the static sand (1625 $\frac{\text{kg}}{\text{m}^3}$) which is consistent with the flow behaving as a packed-bed. The cross-section (A_c) is a constant 3 mm x 203 mm.

By adjusting the outlet valve, the heat flux, and the inlet temperature (via sequential heat up cycles), it is possible to take data over a range of temperatures and mass flow rates. The tests that were run are shown in these two parameters in Figure 78. In total, 34 tests were carried out. Of these 34 tests, 18 data points were associated with a uniform (ambient) inlet temperature supply sand. The other 16 data points were taken after heating the sand in a previous test (these are labeled sequential heat ups). Data with a uniform inlet temperature and

low mass flow rate yields the lowest uncertainty in the calculated heat transfer coefficient because the inlet bulk temperature uncertainty is low and the temperature rise of the sand is large. Data taken after a previous test or at a high flow rate yields the highest uncertainty.

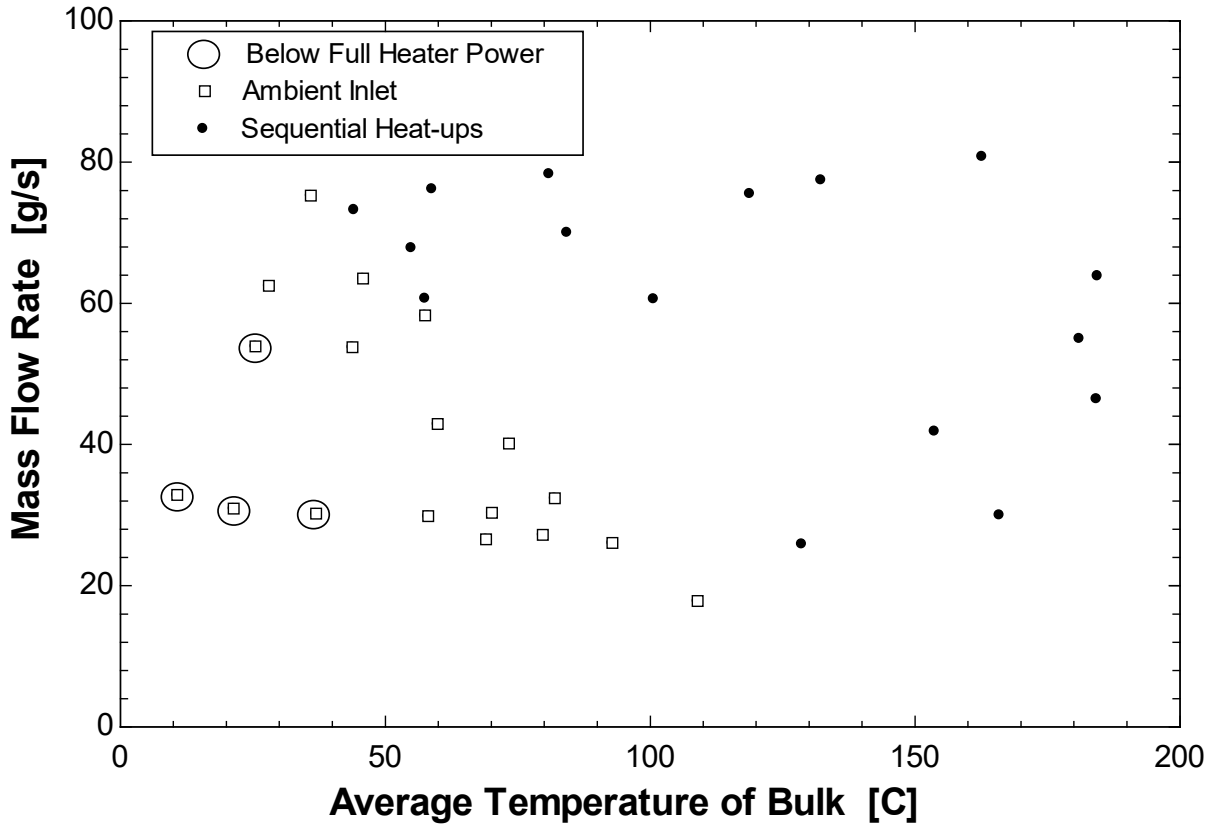

Figure 78 - Experimental data taken shown in the parameter space of mass flow rate and average temperature. All data was taken at full heater power aside from the four points circled. The average temperature is found using the average of the inlet temperature and the maximum of the outlet edge-center average and the outlet centerline average.

Lower flow rates allow higher average temperatures of the bulk sand to be achieved after multiple, sequential heat-ups. For example, the average temperature of the sand could reach 132°C after 6 sequential runs between 60-77.5 g/s while the average temperature could get to 129°C after only 2 sequential runs between 26-30 g/s -- both trials were run at max heater output. To achieve higher average sand temperature at higher flow rates, initial runs need to take place at lower flow rates in order to heat the sand to a high enough temperature before the

final high flow, high temperature run. For sequential heat-ups, there is a diminishing increase in the average bulk temperature of the sand obtained with each consecutive run due to heat loss through the test section, heat loss associated with the hot sand sitting in the basin or hopper during a run, and heat lost during the transfer of sand between runs from the basin to the hopper. Runs at lower flow rates utilize less overall sand in order to run for the same time duration. Therefore, the last two of these negative effects increase, and the result is larger temperature gradients in the supply sand due to the diminished self-insulating properties of the sand.

The dynamic rig took no more than one hour and on average about 40 minutes to achieve steady state. This allows for 3-4 flow rates or heat fluxes to be tested when starting with a full supply hopper of ambient inlet sand, the situation that provides the lowest uncertainty. These tests were ordered from hottest to coldest; that is, the lowest flow rate or highest power test was run first, and the highest flow rate or lowest power test was run last. This ordering ensured that the entire dynamic rig would reach the highest temperature using the minimum amount of supply sand. This decreases the time to reach steady state for the following, lower temperature tests because the rig was pre-heated by the previous run. For runs in which the sand would be cycled through the test section to achieve higher inlet temperature conditions, slightly more than half of the sand was removed from the hopper and stored in another vessel to allow for more runs in a given day.

All of the temperature data for a given run within a series of consecutive heat ups is shown in Figure 79 as a function of time.

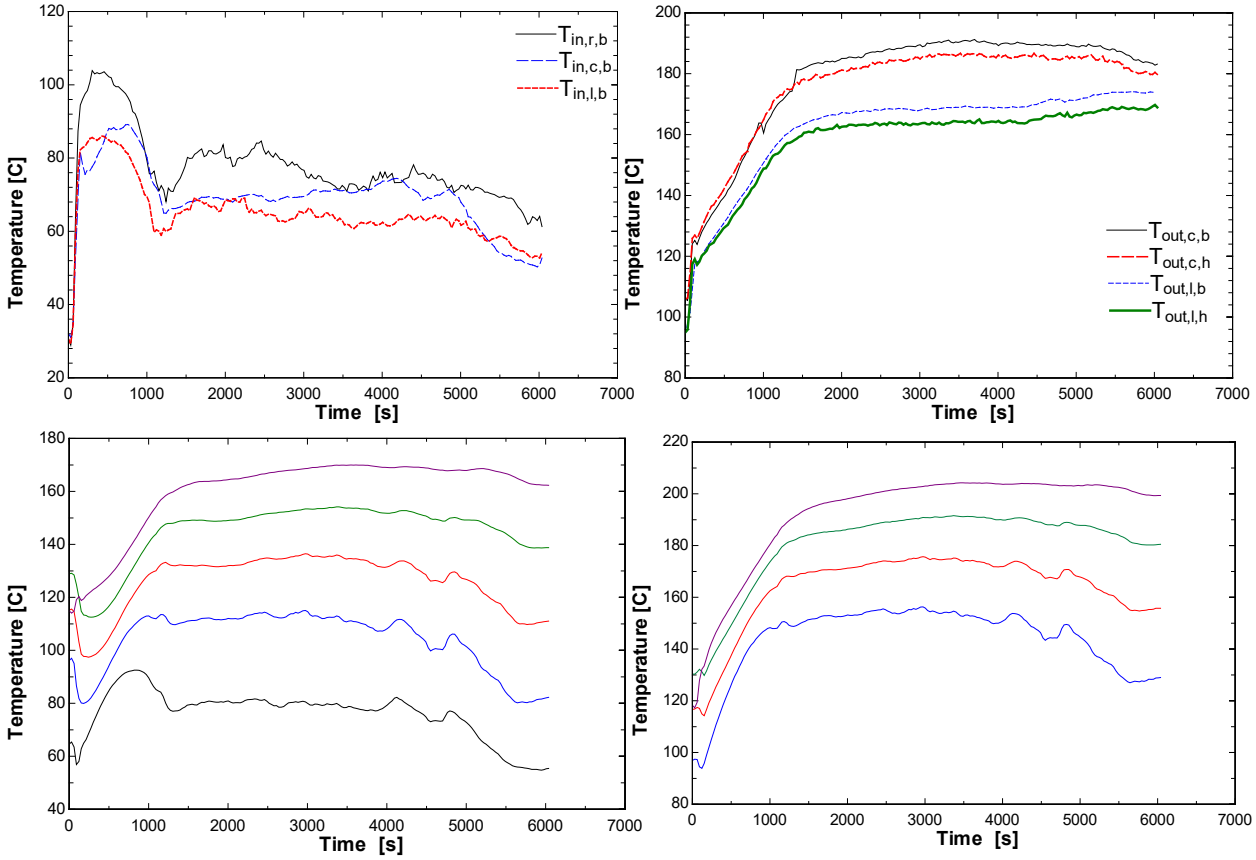

Figure 79 - Temperature data from the second, consecutive heat-up run at 25.4 g/s (25.6 mm/s) at full heater power on 11/19/2020. Starting from the top left and going clockwise: inlet temperatures, outlet temperatures, hot wall temperatures, and backside wall tempertaures. The four temperatures on the hot wall correspond to the same locations along the test section as the top four hotter temperatures on the backside wall.

Note in Figure 79 how the inlet temperature on the right edge is hotter than the center and left edge due to the essentially random temperature gradients that tend to develop in the supply sand. The fluctuation in the inlet temperature seems to have an impact on the temperature measurements on the walls and the outlet temperature and affects the ability for the dynamic rig to approach a consistent steady state.

A run using ambient sand is shown Figure 80. These data are taken after an increase in the velocity accomplished by adjusting the valve on the test section restriction after a previous, higher temperature run with a lower mass flow rate had reached steady state. The

ambient, constant temperature inlet sand in Figure 80 provides much more consistent steady state results, and the associated heat transfer coefficients have much less uncertainty than the data from Figure 79.

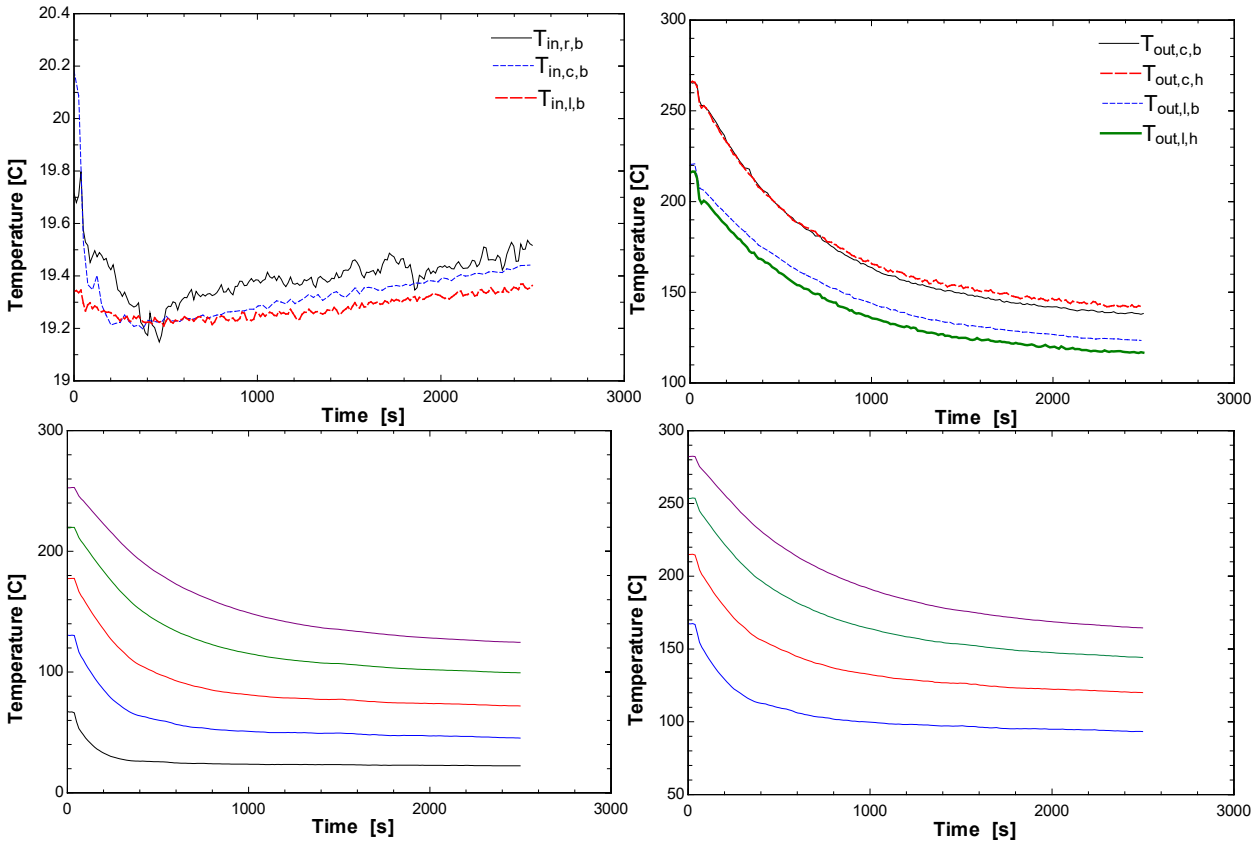

Figure 80 - Temperature data taken at 27.2 g/s (27.5 mm/s) with ambient supply sand following a previous velocity of 12.3 g/s (12.4 mm/s) at full heater power on 11/9/2020. Starting from the top left and going clockwise: inlet temperatures, outlet temperatures, hot wall temperatures, and backside wall tempertaures. The four temperatures on the hot wall correspond to the same locations along the test section as the top four hotter temperatures on the backside wall.

Using the inlet-outlet method in conjunction with the outlet edge-center average, Equations (36) and (39), respectively, yields the following heat transfer coefficient and heat loss data for runs in the 26-34 g/s range:

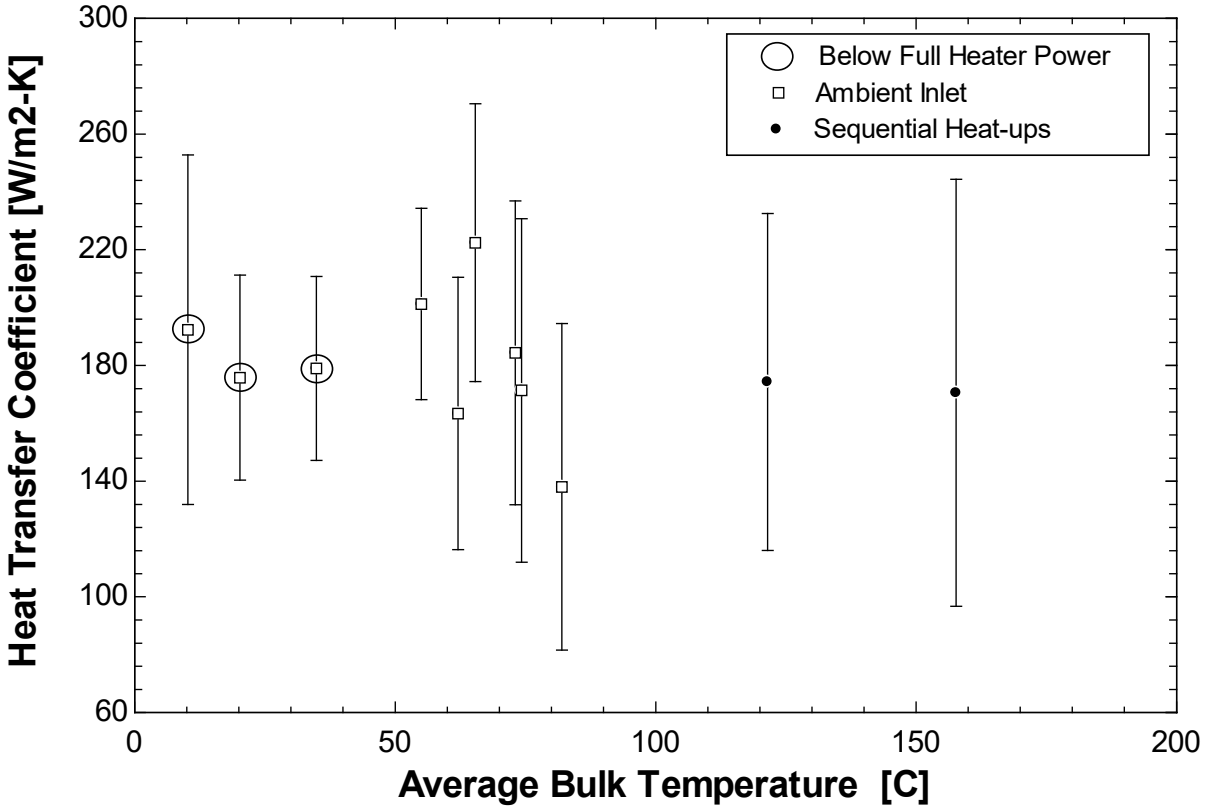

Figure 81 - Inlet-outlet method using the outlet edge-center average for runs in the 26-34 g/s (26-33 mm/s) range to compute the heat transfer coefficient as a function of average temperature of particle flow in the test section

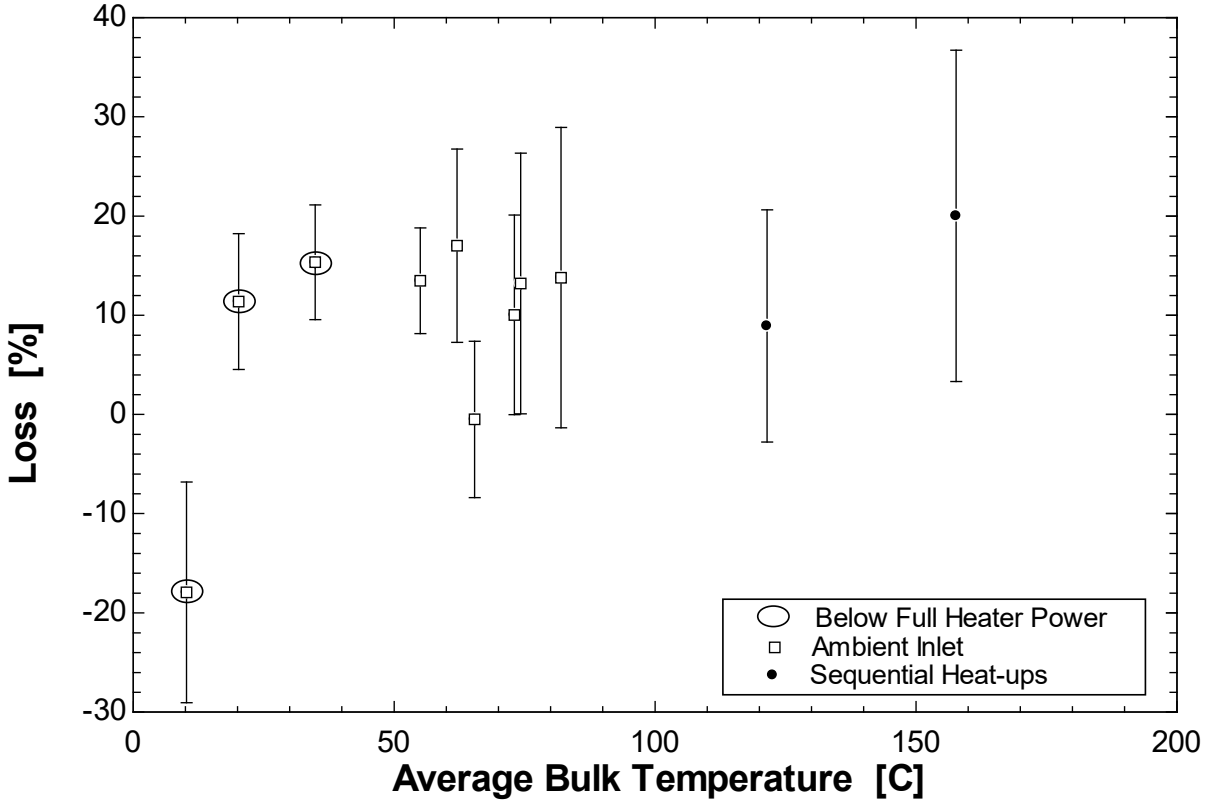

Figure 82 - Inlet-outlet method using the outlet edge-center average for runs in the 26-34 g/s (26-33 mm/s) range to compute the heat loss as a function of average temperature of particle flow in the test section.

Note that the data point in Figure 82 showing a negative heat loss is attributed to running a test in which the test facility is cooling which occurs following an increase in mass flow rate or a reduction in heater power.

Using the inlet-outlet method with the maximum of the outlet edge-center average or the outlet centerline average, Equations (36) and (39) or Equations (36) and (40), respectively, results in larger heat transfer coefficients with lower uncertainty but lower heat losses:

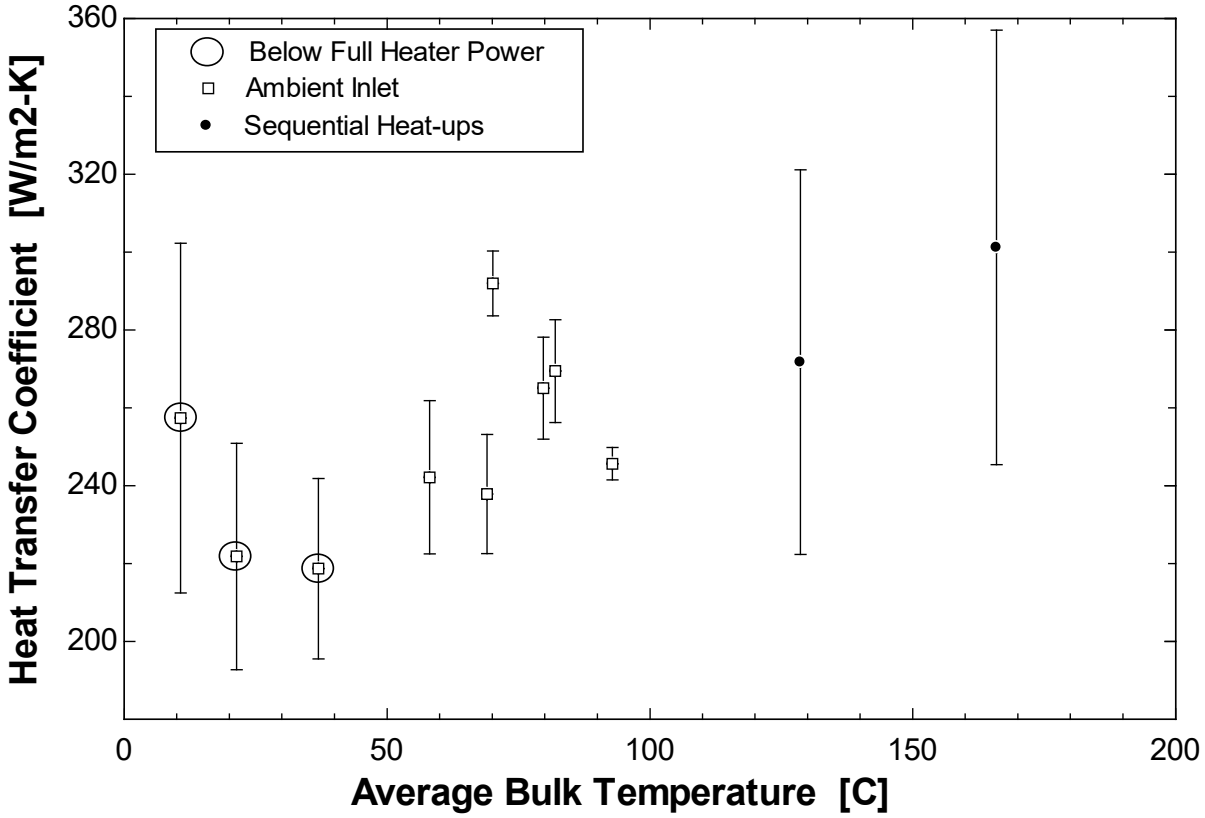

Figure 83 - Inlet-outlet method using the maximum of the outlet centerline average OR the outlet edge-center average for runs in the 26-34 g/s (26-33 mm/s) range to compute the heat transfer coefficient as a function of average temperature of particle flow in the test section.

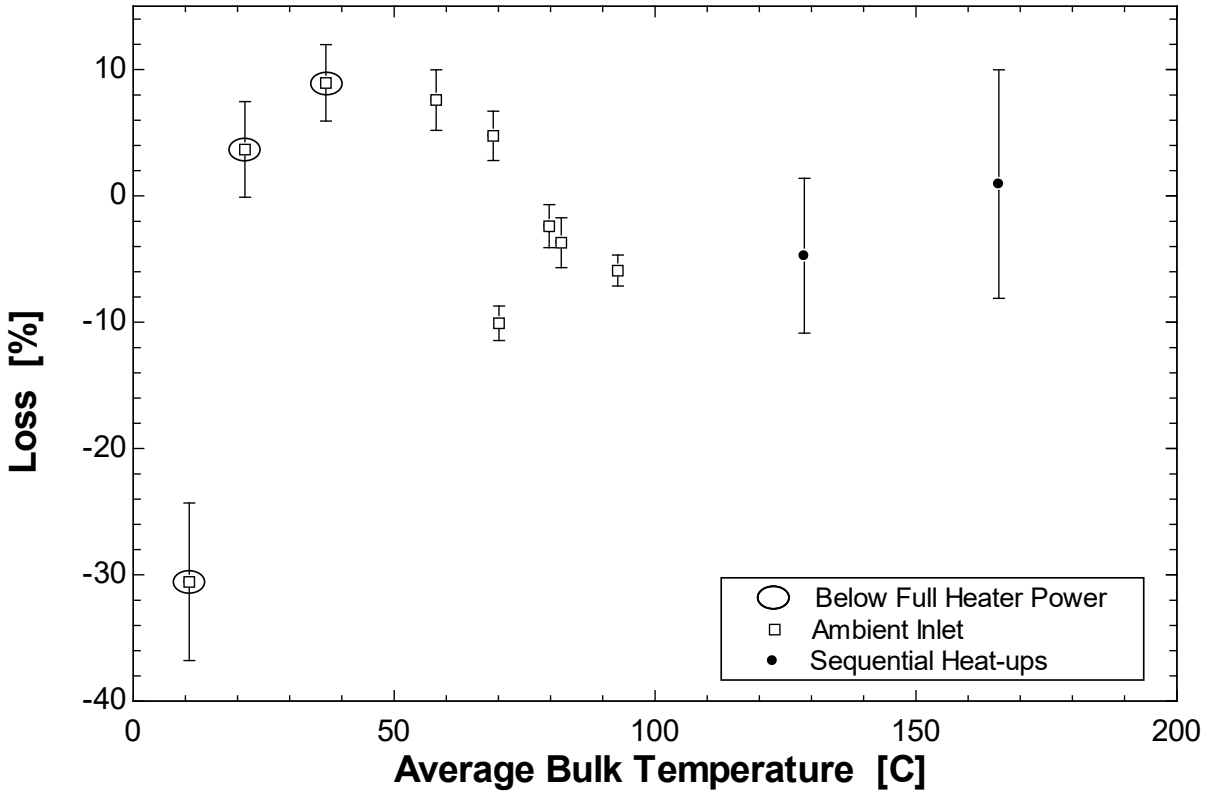

Figure 84 - Inlet-outlet method using the maximum of the outlet centerline average OR the outlet edge-center average for runs in the 26-34 g/s (26-33 mm/s) range to compute the heat loss as a function of average temperature of particle flow in the test section.

The inlet-backside wall method, Equation (37), offers an alternative way to calculate heat transfer coefficient and leads to the lowest uncertainty. The results are similar to those shown in Figure 84 due to the use of temperatures along the centerline:

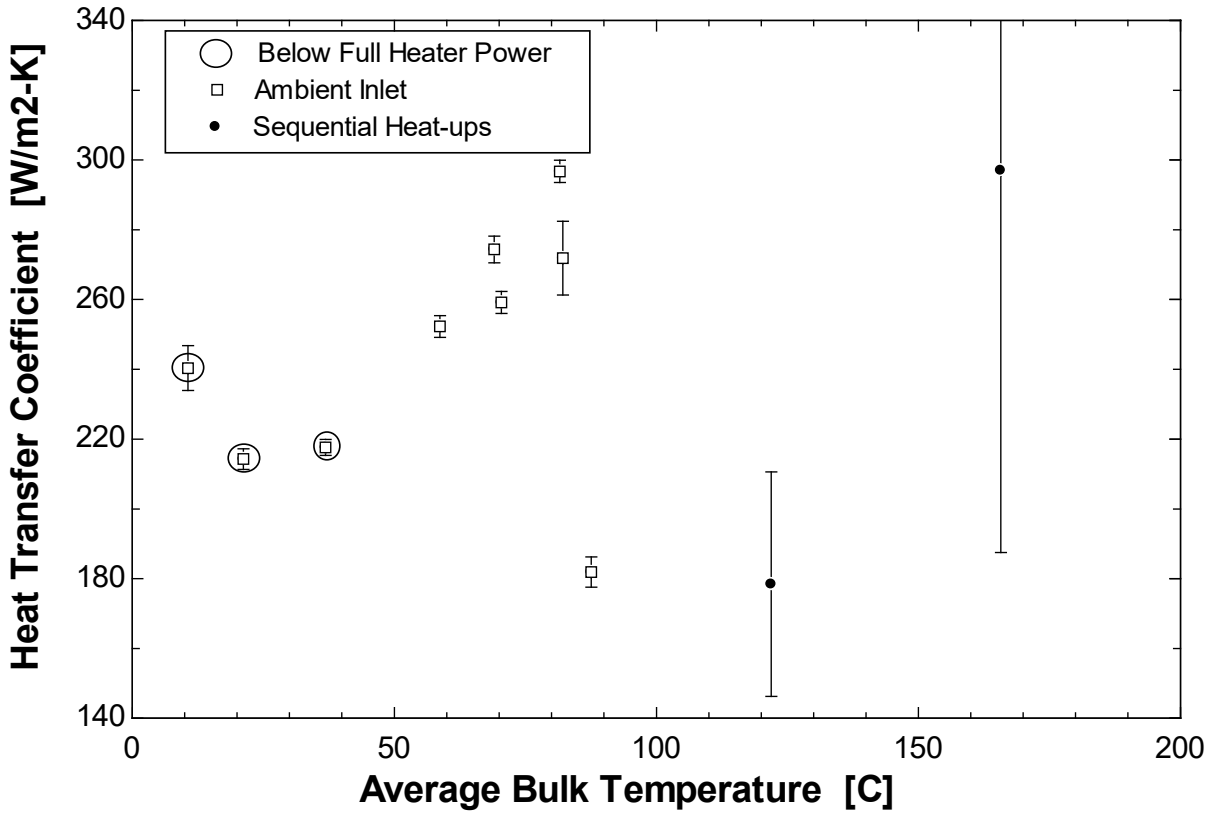

Figure 85 - Inlet-backside wall method for runs in the 26-34 g/s (26-33 mm/s) range to compute the heat transfer coefficient as a function of average temperature of particle flow in the test section.

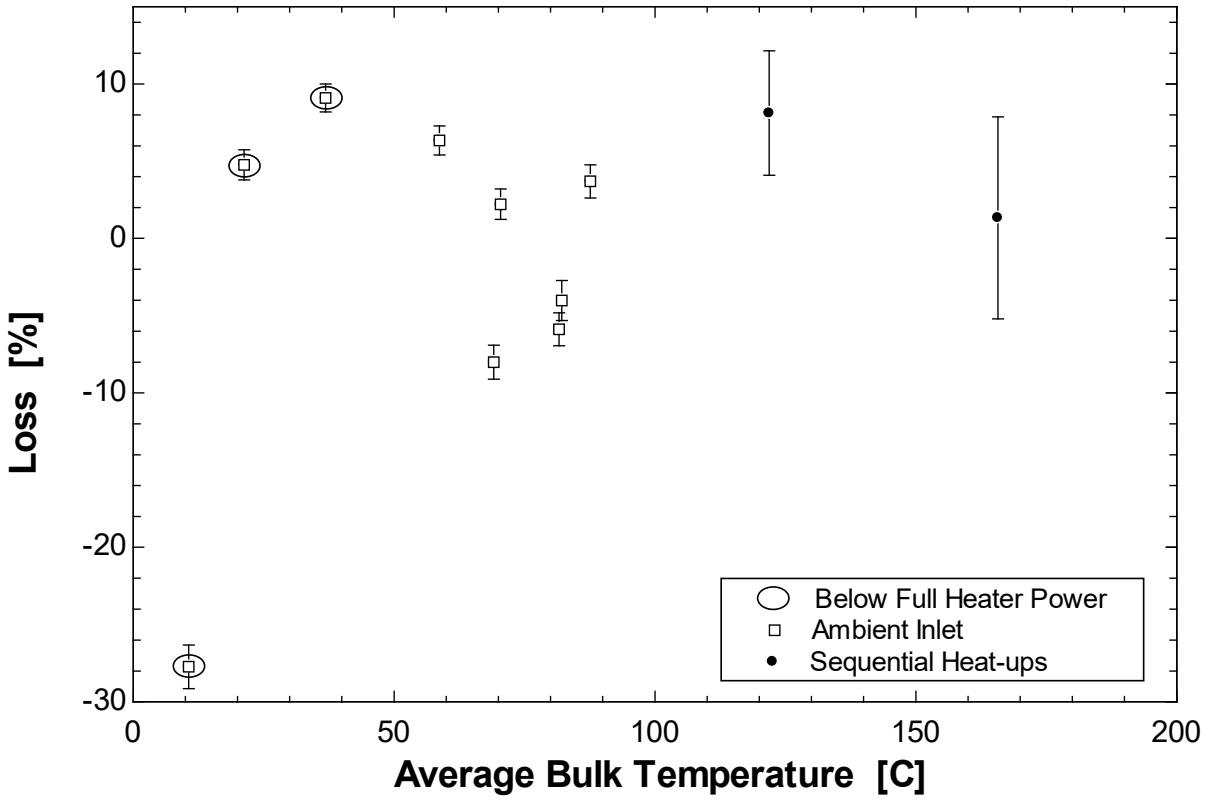

Figure 86 – Inlet-backside wall method for runs in the 26-34 g/s (26-33 mm/s) range to compute the heat loss as a function of average temperature of particle flow in the test section.

Based on a derivation done by Megan Kirschmeier [35] which uses the theoretical technique described in [36], the Nusselt number should be equal to exactly 6 for a fully developed laminar slug flow through an infinitely wide, rectangular test section assuming plug flow, pure conduction, and no edge effect resistance. As seen in Figure 87, the data, using the inlet-outlet method with the maximum of the outlet centerline average or the outlet edge-center average, nearly matches the theory for the Nusselt number and does not vary with velocity. These results are also similar using the inlet-backside wall method, so both methods involving the centerline temperatures of the wall and outlet produce reasonable results for heat transfer coefficients which are shown in Figure 88. The heat transfer coefficients produced in this work are comparable to other research for packed-bed, particle flow, although different types of

particles were used [16], [17], [18]. There is a slight increase in heat transfer coefficient with increasing bulk temperature. The heat loss needs to be calculated using the average temperature across the inlet and the average temperature across the outlet (i.e., outlet edge-center average). As seen in Figure 89, the heat loss increases with bulk temperature as a result of the thermal conductivity of the insulation increasing with temperature which decreases insulation performance.

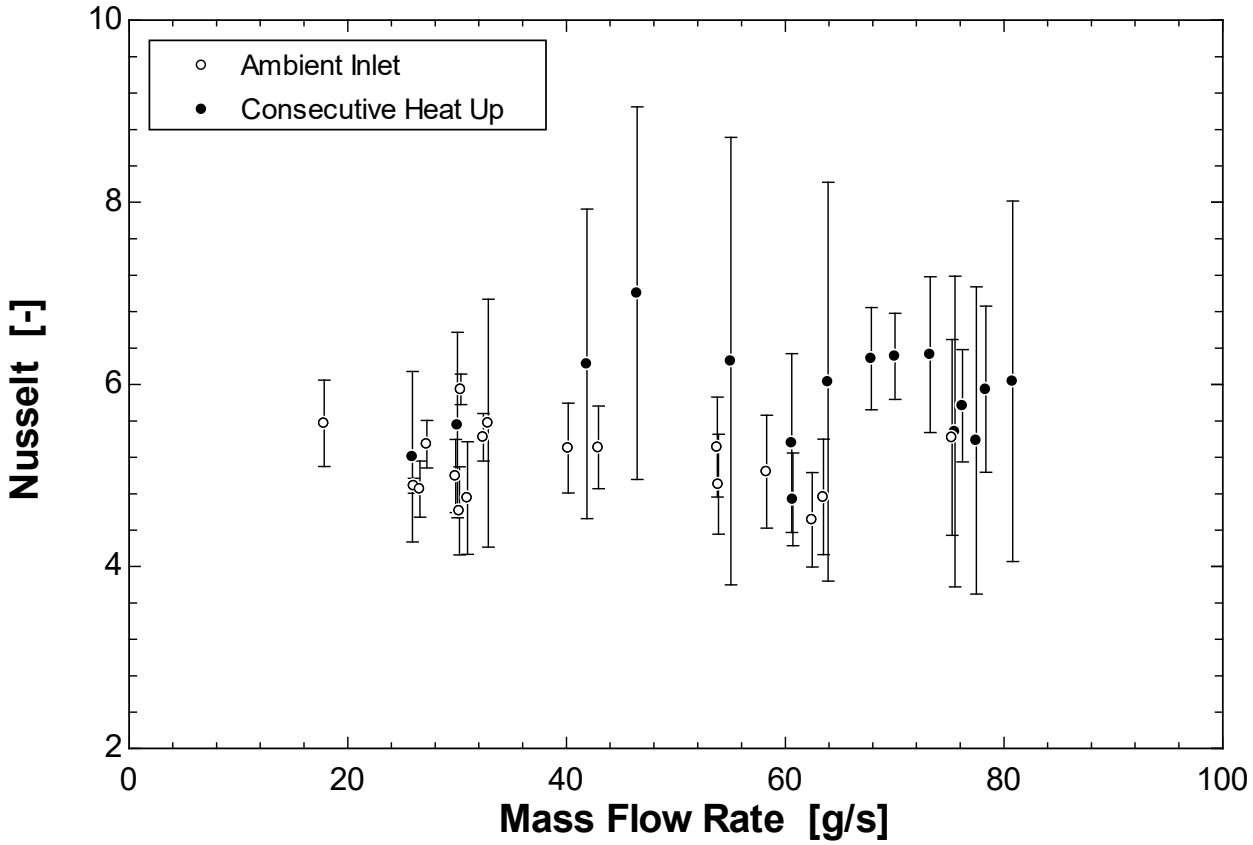

Figure 87 - Nusselt number versus flow rate for all data using the inlet-outlet method with the outlet centerline average. Theoretical value for laminar slug flow in an infinitely wide, rectangular cross section is equal to exactly 6.

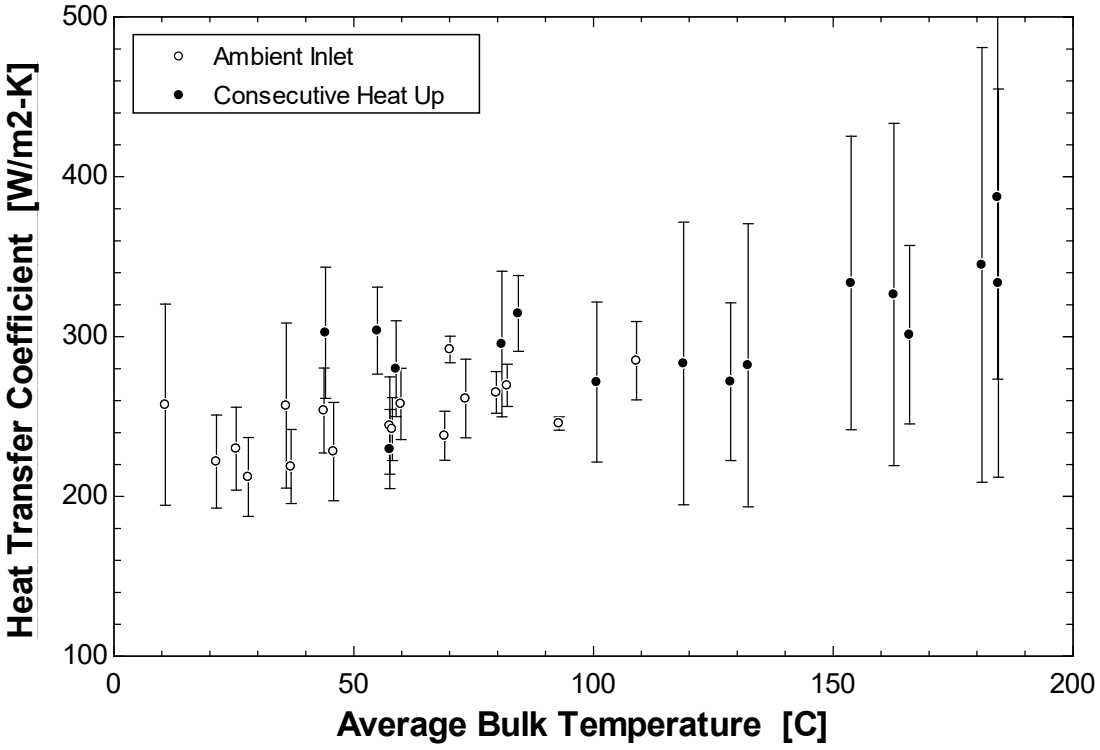

Figure 88 - Heat transfer coefficients for all runs using the inlet-outlet method with the outlet centerline average.

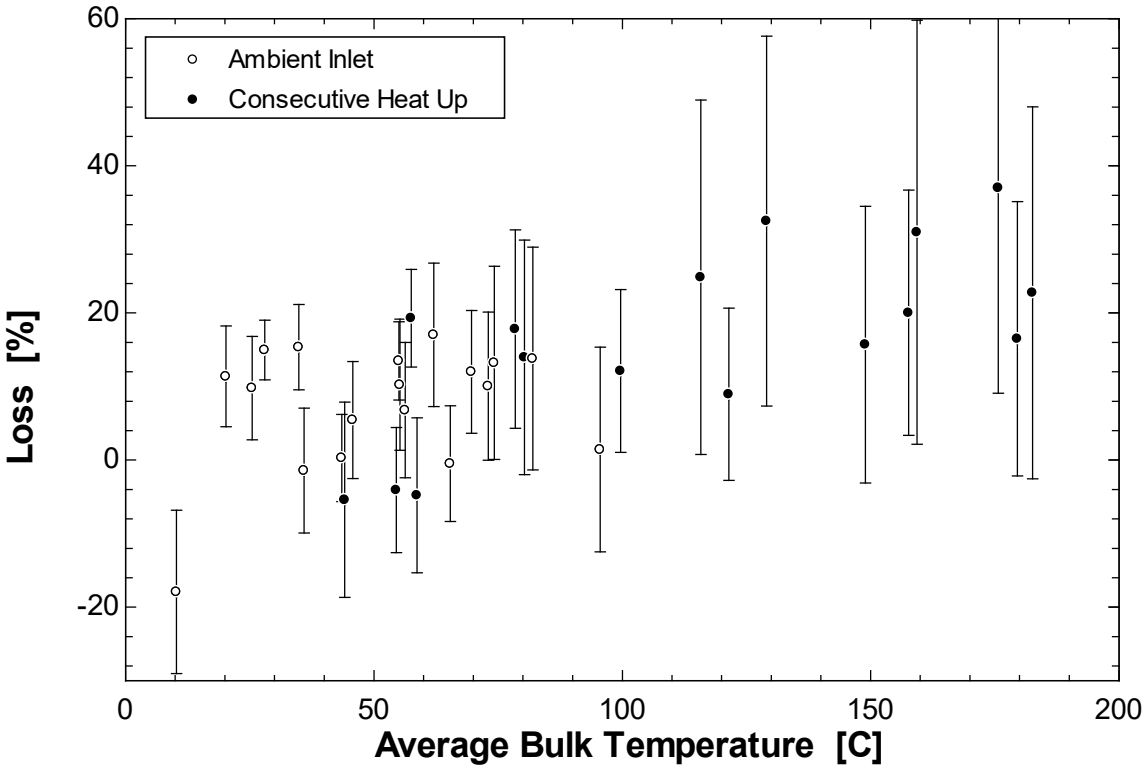

Figure 89 - Heat loss for all runs using the inlet-outlet method with the outlet edge-center average

Conclusion

The first experimental facility, deemed the "Static Rig," was constructed in order to determine high-temperature bulk thermal conductivity, heat capacitance, and interface resistance of six pure Silica particles and two Alumino-Silicate particles of various size distributions in a 75-800 micron range. A 3D ANSYS model was used to analyze the steady state and transient trends of those particles at various temperatures. The bulk thermal conductivities for the Silica sands are in the range of 0.33-0.64 $\frac{\mathrm{W}}{\mathrm{m-K}}$ over 220-815°C (which is in good agreement with other experimentation performed for the same Silica sands) and for the Alumino-Silicate sands are in the range of 0.27-0.45 $\frac{\mathrm{W}}{\mathrm{m-K}}$ over 235-670°C; the bulk thermal conductivity of all the particles increases non-linearly with temperature. As average particle size of the distribution decreased, the bulk thermal conductivity decreased. The specific heat capacitance for the particles is deemed to be the same as the bulk material and can be estimated using standardized values for the specific heat capacitance of the bulk material. The specific heat capacitance of the particles increases non-linearly with temperature, but there is a noted phase change in the crystalline structure of Quartz at 573°C which causes a step decrease in specific heat capacitance for the Silica and Alumino-Silicate sands. The interface resistance between the particles and the wall was unable to be determined.

Future work for static testing of particles should include:

- Understanding the mechanisms to describe the phenomenon of smaller particles having lower bulk thermal conductivity
- Experimentally determining the effects of conduction through the particles, convection

of the interstitial gas, and radiation between the particles as well as the temperature dependent properties of particle material (e.g., thermal expansion, thermal conductivity, etc.) on the overall bulk thermal conductivity of the particles

- Further development of the available models to more accurately estimate the bulk thermal conductivity of the particles

The second experimental facility, deemed the "Dynamic Rig," was designed to measure heat transfer coefficients of a packed-bed, particle flow, much like a laminar slug flow, through a high aspect ratio, rectangular channel with a 3 mm gap. A specific size distribution of Silica sand in the range of 100-600 microns was chosen, in part because of its flowability. The heat transfer coefficients for this configuration are determined during thermal steady state and fully developed flow and are in the range of 200-400 $\frac{\mathrm{W}}{\mathrm{m}^2-\mathrm{K}}$ over 10-190°C which are in good agreement with other literature for other types of particles; the heat transfer coefficient increased with temperature. The experimentally determined Nusselt number showed good correlation with theoretically determined Nusselt number of 6 for this configuration.

One major issue in the uncertainty of the heat transfer coefficient measurements is the uncertainty of the inlet temperature during sequential heating cycles of the particles. This uncertainty could be mitigated with the addition of an unheated, adiabatic flow section added between to the supply hopper and the test section. The adiabatic section would consist of only an insulated flow channel and allows the sand to come to a uniform temperature before entering the test section.

Future work for the dynamic testing of particles should include:

- Achieving higher temperature particle flow with various particle sizes and materials, velocities, and geometries to increase the overall available research on packed-bed, particle flow
- Development of a model to accurately depict the heat transfer in a packed bed particle flow
- Determining if the bulk density of a packed bed particle flow changes as a result of flow rate, thermal expansion, pressure, etc.
- Identifying a viscosity value for packed bed particle flow to aide in determining non-dimensional numbers for particle flow to compare mass and thermal transport (e.g., Reynolds number, Prandtl number, etc.)
- Comparison of packed bed particle flow to fluidized particle flow

Bibliography

[1] Office of Energy Efficiency and Renewable Energy, "Concentrating Solar-Thermal Power," Department of Energy, [Online]. Available: https://www.energy.gov/eere/solar/concentrating-solar-thermal-power. [Accessed December 2020].

[2] Z. Ma, G. Glatzmaier and M. Mehos, "Fluidized bed technology for concentrating solar power with thermal energy storage," *Journal of Solar Energy Engineering,* vol. 136, no. 3, p. Article number 031014, 2014.

[3] J. Lilliestam, T. Barradi, N. Caldes, M. Gomez, S. Hanger, J. Kern, N. Komendantova, M. Mehos, W. Hong, Z. Wang and A. Patt, "Policies to keep and expand the option of concentrating solar power for dispatchable renewable energy," *Energy Policy,* vol. 116, pp. 193-197, 2018.

[4] Helioscsp, "Helioscsp Thermal Energy News," 11 May 2017. [Online]. Available: http://helioscsp.com/concentrated-solar-power-could-provide-the-flexibility-and-reliability-the-u-s-electric-grid-needs/. [Accessed December 2020].

[5] M. F. Herraiz, "Solar Steam for Industrial Processes," Solatom, 2018. [Online]. Available: www.solatom.com/index.html. [Accessed December 2020].

[6] K. Lovegrove and W. Stein, Concentrating Solar Power Technology (Second Edition), Woodhead Publishing, 2020.

[7] X. Xu, K. Vignarooban, B. Xu, K. Hsu and A. Kannan, "Prospects and problems of concentrating solar power technologies for power generation in the desert regions," *Renewable and Sustainable Energy Reviews,* vol. 53, pp. 1106-1131, 2016.

[8] Atlas Obscura, "Solar One and Solar Two," Atlas Obscura, [Online]. Available: https://www.atlasobscura.com/places/solar-one-and-solar-two. [Accessed December 2020].

[9] Torresol Energy, "Gemasolar," Torresol energy, [Online]. Available: https://torresolenergy.com/gemasolar/. [Accessed December 2020].

[10] Office of Energy Efficiency & Renewable Energy, "The SunShot Initiative," Deparment of Energy, [Online]. Available: https://www.energy.gov/eere/solar/sunshot-initiative. [Accessed December 2020].

[11] C. Zhao and Z. Wu, "Thermal property characterization of a low melting-temeprature ternary nitrate salt mixture for thermal energy storage systems," *Solar Energy Materials & Solar Cells,* vol. 95, no. 12, pp. 3341-3346, 2011.

[12] Y.-t. WU, Y. LI, Y.-w. LU, H.-f. Wang and C.-f. MA, "Novel low melting point binary nitrates for thermal energy storage applications," *Solar Energy Materials and Solar Cells,* vol. 164, pp. 114-121, 2017.

[13] A. Palacios, A. Calderon, C. Barrrenche, J. Bertomeu, M. Segarra and A. I. Fernandez, "Study on solar absorptance and thermal stability of solid particles materials used as TES at high temperature on different aging stages for CSP applications," *Solar Energy Materials and Solar Cells,* vol. 201, 2019.

[14] A. Caleron, A. Palacios, C. Barraenche, M. Segarra, C. Prieto, A. Rodriguez-Sanchez and A. I. Fernandez, "High temperature systems using solid particles as TES and HTF material: A review," *Applied Energy,* vol. 213, pp. 100-111, 2018.

[15] C. Ho, J. Christian, A. Moya, S. Jeter, S. Abdel-Khalik, D. Sadowski, N. Siegel, H. Al-Ansary, L. Amsbeck, B. Gobereit and R. Buck, "Technology advancements for next generation falling particle receivers," *Energy Procedia,* vol. 49, pp. 398-407, 2014.

[16] M. F. Kirschmeier, "A Heat Transfer Analysis of Vertical Dense Granular Flows," Ph.D. Thesis, University of North Carolina State, 2018.

[17] E. F. Johnson, "Conceptual Design and Heat Transfer Investigation of Dense Granular Flow Solar Receiver," M.S. Thesis, Middle East Technical University, 2017.

[18] K. J. Albrecht and C. K. Ho, "Design and operating considerations for a shell-and-plate, moving packed-bed, particle-to-sCO2 heat exchanger," *Solar Energy,* vol. 178, pp. 331-340, 2019.

[19] A. S. C177-19, "Standard Test Method for Steady-State Heat Flux Measurements and Thermal Transmission Properties by Means of the Guarded-Hot-Plate Apparatus," ASTM International, West Conshohocken, PA, 2019.

[20] LUNA, "Sensing and Non-Destructive Testing - Temperature," LUNA, 2020. [Online]. Available: https://lunainc.com/capability/temperature. [Accessed December 2020].

[21] M. Weathered, "Characterization of Sodium Thermal Hydraulics with Optical Fiber Temperature Sensors," Ph.D. Thesis, University of Wisconsin-Madison, 2017.

[22] G. Nellis and S. Klein, Heat Transfer, Cambridge University Press, 2009.

[23] Aspen Aerogels, "Pyrogel XTF," [Online]. Available: https://www.aerogel.com/_resources/common/userfiles/file/Data%20Sheets/Pyrogel_XTF_DS.pdf. [Accessed December 2020].

[24] F. Molaei and H. Siavoshi, "Molecular dynamics studies of thermal conductivity and mechanical properties of single crystalline α-quartz," *Solid State Communications,* vol. 320, 2010.

[25] MakeItFrom.com, "Alumina (Aluminum Oxide, Al2O3)," MakeItFrom.com, 30 May 2020. [Online]. Available: https://www.makeitfrom.com/material-properties/Alumina-Aluminum-Oxide-Al2O3. [Accessed December 2020].

[26] R. Chen, Interviewee, *Personal Communications.* [Interview]. 4 May 2020.

[27] R. Bauer and E. U. Schlunder, "Part I: Effective radial thermal conductivity of packings in gas flow. Part II: Thermal conductivity of the packing fraction without gas flow," *International Chemical Engineering,* vol. 18, no. 2, pp. 189-204, 1978.

[28] W. v. Antwerpen, C. d. Toit and P. Rousseau, "A review of correlations to model the packing structure and effective thermal conductivity in packed beds of mono-sized spherical particles," *Nuclear Engineering and Design,* vol. 240, pp. 1803-1818, 2010.

[29] W. v. Antwerpen, P. Rousseau and C. D. Toit, "Multi-sphere Unit Cell model to calculate effective thermal conductivity in packed pebble beds of mono-sized spheres," *Nucl. Eng. Des.,* vol. 247, pp. 183-201, 2012.

[30] "NIST-JANAF Thermochemical Tables," National Institute of Standards and Technology, 1998. [Online]. Available: https://janaf.nist.gov/. [Accessed December 2020].

[31] A. C. Akhavan, "The Silica Group," The Quartz Page, 12 January 2014. [Online]. Available: http://www.quartzpage.de/gen_mod.html. [Accessed 11 December 2020].

[32] G. Mehos, Hopper Design Principles for Chemical Engineers, Westford, MA: Greg Mehos & Associates LLC, 2020.

[33] D. Witkowski, Interviewee, *Personal Communication.* [Interview]. 8 November 2019.

[34] D. Schulze, "Silo Stress Tool," 2019. [Online]. Available: https://www.dietmar-schulze.de/fre.html. [Accessed December 2020].

[35] M. Kirschmeier, Interviewee, *Personal Communication.* [Interview]. 23 Novermber 2020.

[36] Y. Muzychka, E. Walsh and P. A. Walsh, "Simple Models for Laminar Thermally Developing Slug Flow in Non-Circular Ducts and Channels," *Journal of Heat Transfer,* vol. 132, no. 11, 2010.

Appendix A: Fairmount Santrol's Wedron Silica Data Sheet

TECHNICAL DATA SHEET

WEDRON SILICA

HIGH-PURITY ROUND GRAIN SILICA SAND

Wedron Silica is a high-purity, round grain silica sand. It ranges from coarse to very fine sand and is mined from the St. Peter Sandstone, which is a 459-455 million years old sand deposit that runs from Minnesota to Oklahoma.

APPLICATIONS

- Epoxy flooring
- Grout and plaster
- Landscaping
- Pool Construction
- Roofing
- Road Paving

TYPICAL ANALYSIS

PERCENT RETAINED ON EACH MESH

Microns	Mesh Size	480	460	430	420	410	530	520	510	730
850	20	0.0	0.0	0.0	0.0	0.0	0.0	0.0	0.0	0.0
600	30	13.1	0.7	0.1	0.1	0.0	0.0	0.0	0.0	0.0
425	40	73.9	60.7	30.9	18.8	11.2	1.2	0.7	0.0	0.0
300	50	12.0	34.5	45.2	37.5	31.2	25.6	22.2	8.7	2.2
212	70	0.9	3.8	19.4	28.3	33.4	39.9	36.3	27.8	14.7
150	100	0.0	0.3	3.8	12.2	18.2	24.6	27.7	41.7	47.5
106	140	0.0	0.0	0.6	2.9	5.4	7.6	11.2	17.9	28.8
75	200	0.0	0.0	0.0	0.2	0.6	1.1	1.9	3.8	6.4
53	270	0.0	0.0	0.0	0.0	0.0	0.0	0.0	0.1	0.4
<53	Pan	0.0	0.0	0.0	0.0	0.0	0.0	0.0	0.0	0.0
AFS/GFN		30	34	40	46	51	57	60	70	80

TYPICAL PHYSICAL & CHEMICAL PROPERTIES

Grain Shape	Round
LOI	0.07%
ADV	1.0
pH	7.0
SiO_2	99.65%
Al_2O_3	0.065%
Fe_2O_3	0.018%
TiO_2	0.011%
CaO	0.012%

WARNING: Contains Free Silica. Do Not Breathe Dust. Prolonged exposure to dust may cause delayed lung injury (silicosis). Monographs on the Evaluation of the Carcinogenic Risk of Chemicals to Humans (vol 68, 1997) concludes that there is sufficient evidence in humans for the carcinogenicity of inhaled crystalline silica in the forms of quartz and cristobalite (Group 1) in certain industrial circumstances, but that carcinogenicity may be dependent on inherent characteristics of the crystalline silica or on external factors affecting biological activity or distribution activity or distribution of its polymorphs. See Material Safety Data Sheet for detailed information. CAS 14808-60-7 FOR INDUSTRIAL USE ONLY.

All information contained herein is subject to change without notice. The information contained in this data sheet is for general application and is believed to be accurate at the time of printing. Data listed has been generated by Fairmount Santrol and/or independent laboratories. Every real-world sampling is different so your results may vary. Fairmount Santrol makes no warranty, expressed or implied, concerning these products and assumes no responsibility or liability whatsoever for any of the information contained herein or for the use of such information.

Fairmount Santrol, 3450 East 2056th Rd, Wedron, IL 60557
800.255.7263 | Fax: 269.465.6075 | Sales@FMSA.com
FairmountSantrol.com

FairmountSantrol

FMSA0067_0113_0118

Figure 90 - Data sheet for Fairmount Santrol's Wedron Silica sands

Appendix B: Christy Minerals Alumino-Silicate Data Sheet

ISO 9001:2008 CERTIFIED

CHRISTY® MINERALS

STKO® Alumino-Silicate Grains and Flours

STKO® Alumino-Silicate contains less cristobalite so that it does not exhibit a high expansion at autoclave temperatures. This makes it ideal for today's precision investment caster.

STKO® is screened to close tolerances to assure consistent, precise sizing. Plus, constant de-dusting throughout the screening process makes STKO® virtually dust-free. Christy works with customers to determine proper size – from coarse to fine grains.

When your application demands superior ceramic refractory mold media, STKO® grains and flours deliver the precision performance you need.

Chemical Analysis	STKO®
SiO_2	51.65%
Al_2O_3	43.05%
Fe_2O_3	1.25%
TiO_2	2.27%
MgO	0.41%
CaO	0.25%
Na_2O	0.02%
K_2O	0.90%
P_2O_5	0.20%

Physical Properties	STKO®
Bulk Density	2.55 (gm/cc)
Apparent Porosity	2.5%
PCE	33-34
Mineralogy:	
Mullite	65%
Glass	25%
Cristobalite	10%

Note: All data subject to reasonable deviation. ASTM Test Methods, where applicable, used for determination of data.

Thermal Expansion

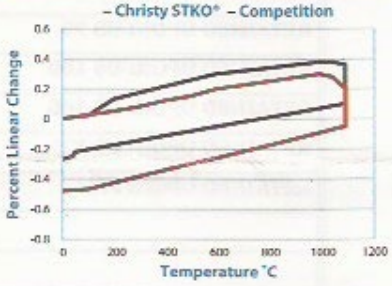

Typical Particle Size Distribution (% Retained)

U.S.S. Sieve Size	16	20	30	40	50	70	100	140	200	270	325	Pan*
STKO® 14 x 28	0-1	20-45	25-45	15-30	5-15							0-1
STKO® 22 S	0-1	15-40	45-70	15-30	0-3							0-1
STKO® 35 S	0-1	5-15	25-50	25-50	5-15	0-1						0-1
STKO® 50 S		0-1	0-3	25-55	25-45	10-30	0-10	0-3				0-1
STKO® 60 S			0-1	0-10	25-70	25-50	0-10	0-6				0-1
STKO® 105 S					0-5	30-60	35-55	5-20			0-5	0-3
Ceramic Ball Milled Flours	Microtrac D-50 Channel											
STKO® 150 S	30-40 µ											
STKO® 200 S	20-30 µ											

*PAN indicates percentage of material which passed the last screen per sizing

Plant: P.O. Box 159 • High Hill, MO 63350 • Phone: 636.585.2214 • Fax: 636.585.2220 • www.christyco.com

Sales Office/Distributor:

Revised: January 2013

Figure 91 - Data sheet for Christy Minerals MCFC STKO Alumino-Silicate sands

Appendix C: Experimentally Determined Thermal Conductivities

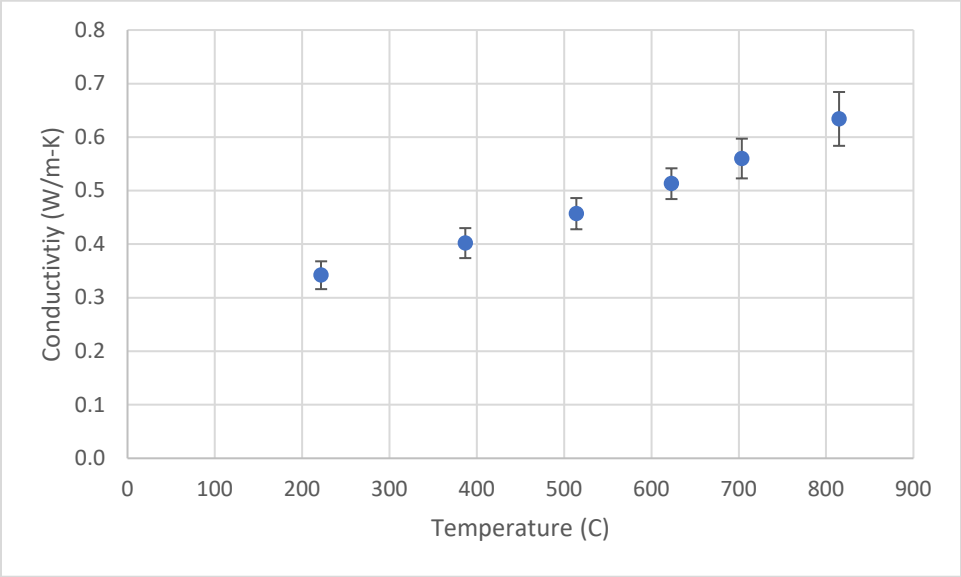

Figure 92 - Thermal conductivity as a function of temperature for Wedron Silica #410. These results agree with [26].

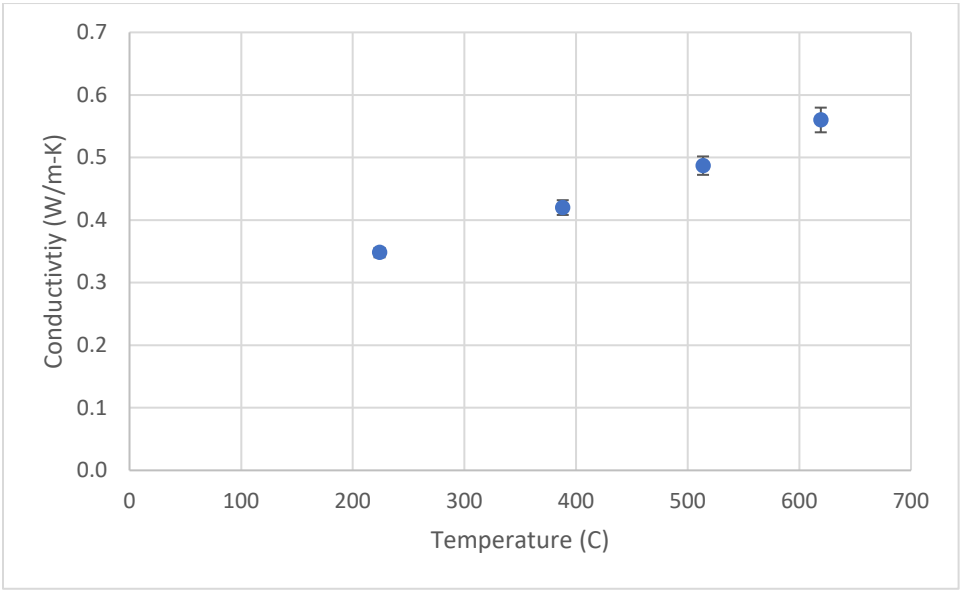

Figure 93 - Thermal conductivity as a function of temperature for Wedron Silica #430. These results agree with [26].

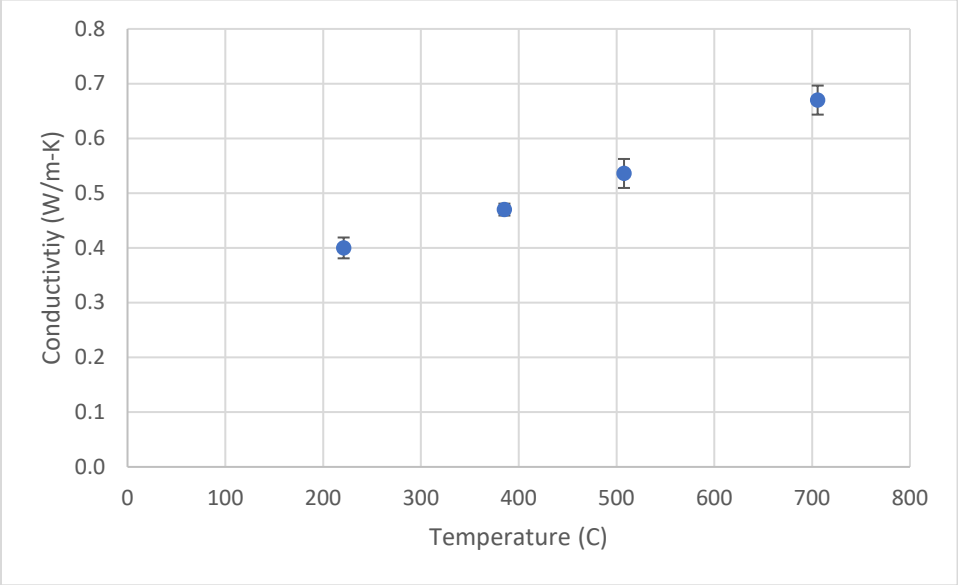

Figure 94 - Thermal conductivity as a function of temperature for Wedron Silica #460

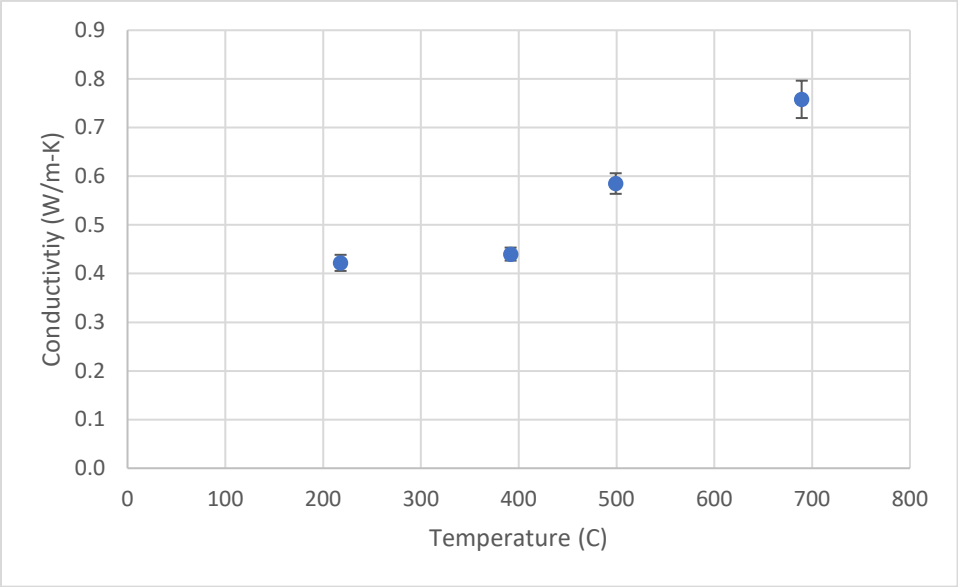

Figure 95 - Thermal conductivity as a function of temperature for Wedron Silica #480. These results agree with [26].

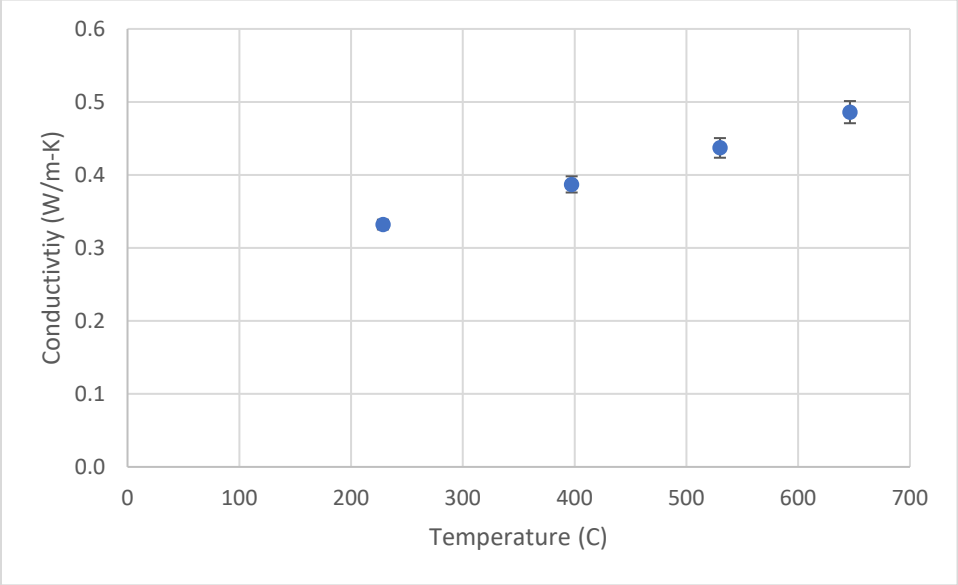

Figure 96 - Thermal conductivity as a function of temperature for Wedron Silica #510

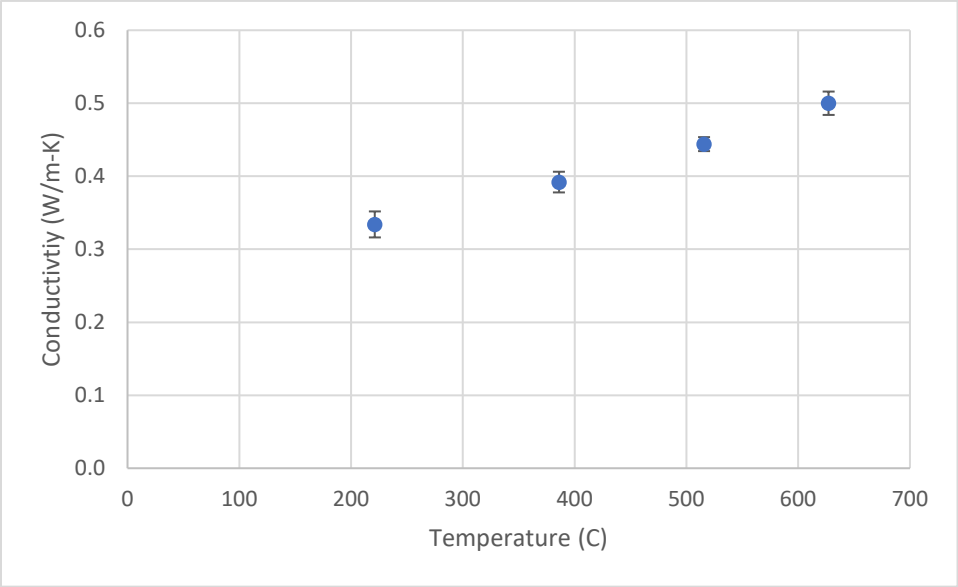

Figure 97 - Thermal conductivity as a function of temperature for Wedron Silica #530

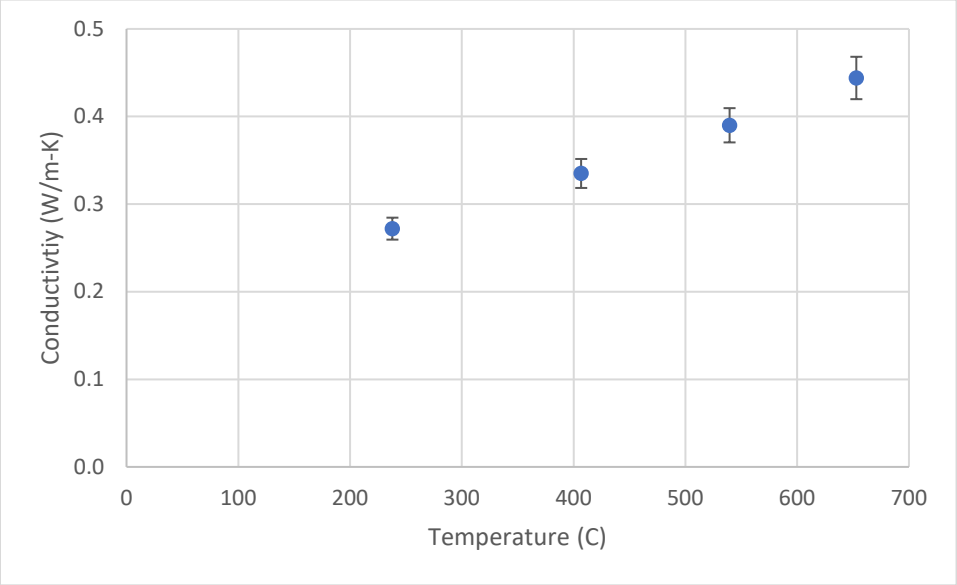

Figure 98 - Thermal conductivity as a function of temperature for Christy Minerals MCFC 50S

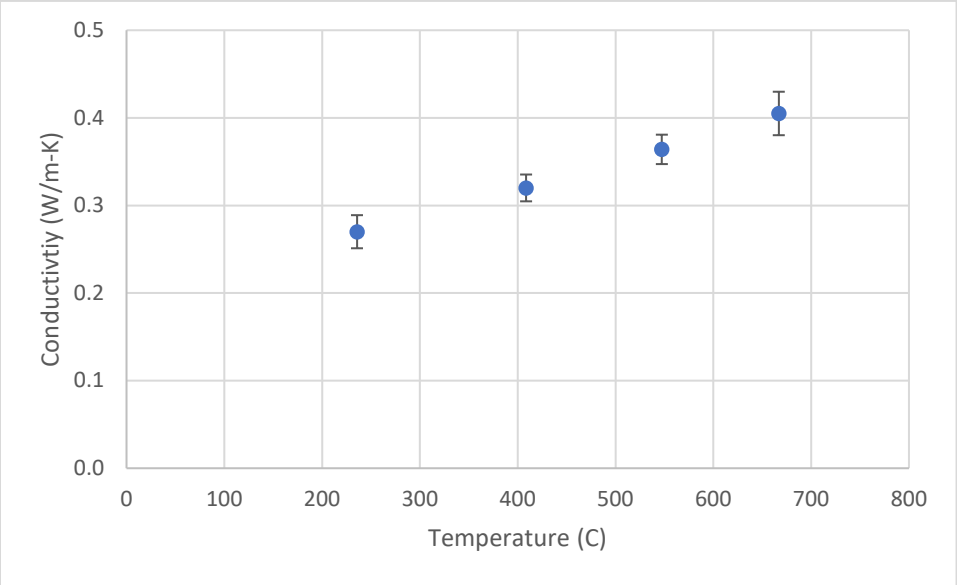

Figure 99 - Thermal conductivity as a function of temperature for Christy Minerals MCFC 60S